

WGN

48:3
june 2020



In memoriam: Prof. Dr. Oleg Belkovich
IMC 2020 replaced by Virtual IMC Day
NASA all-sky fireball data available
New meteor showers discovered using Encontreitor
Cosmic rays and meteors
December IMO video meteors and 2018 summary

Administrative

- In memoriam: Prof. Dr. Oleg Igorevich Belkovich (1934 – 2020) *Galina Ryabova and Cis Verbeeck* 57
- Registration for the online IMC 2020 is open! *IMO Council and IMC 2020 LOC and SOC* 59

Meteor science

- Seven years of bright meteor data from the NASA All Sky Fireball Network *Aaron Kingery, Danielle E. Moser, William J. Cooke, and Althea V. Moorhead* 60
- Encontreiro: First Radiants *Leonardo S. Amaral, Carlos A.P.B. Bella, Lauriston S. Trindade, Gabriel G. Silva, Rubens Damigle, Marcelo L.P.V. Zurita, Marcelo W.S. Domingues, Renato C. Poltronieri, Cristóvão J.L. Faria, Carlos F. Jung* 69
- From Cosmic Rays and Meteors *H. W. Wilschut* 89

Preliminary results

- Results of the IMO Video Meteor Network — December 2018, and summary of 2018 *Sirko Molau, Stefano Crivello, Rui Goncalves, Carlos Saraiva, Enrico Stomeo, Jörg Strunk, and Javor Kac* 92

Front cover photo

This beautiful meteor shot through while shooting panorama with Canon EOS 700D at ISO 3200 in Torres, Rio Grande do Sul, Brazil at Morro das Furnas on 2020 May 18, at 8:59 pm local time. Photo courtesy: Gabriel Zaparolli.

Writing for WGN This Journal welcomes papers submitted for publication. All papers are reviewed for scientific content, and edited for English and style. Instructions for authors can be found in WGN **45:1**, 1–5, and at <http://www.imo.net/docs/writingforwgn.pdf>.

Copyright It is the aim of WGN to increase the spread of scientific information, not to restrict it. When material is submitted to WGN for publication, this is taken as indicating that the author(s) grant(s) permission for WGN and the IMO to publish this material any number of times, in any format(s), without payment. This permission is taken as covering rights to reproduce both the content of the material and its form and appearance, including images and typesetting. Formats include paper, CD-ROM and the world-wide web. Other than these conditions, all rights remain with the author(s).

When material is submitted for publication, this is also taken as indicating that the author(s) claim(s) the right to grant the permissions described above.

Legal address International Meteor Organization, Jozef Mattheessensstraat 60, 2540 Hove, Belgium.

In memoriam: Prof. Dr. Oleg Igorevich Belkovich (1934 – 2020)

Galina Ryabova¹ and Cis Verbeeck

Received 2020 July 17

On July 11, 2020 at 5 am Professor Oleg Belkovich passed away after a long illness.

Oleg Belkovich was born in Kazan, in a family of an astronomer. His father, Igor Vladimirovich Belkovich, world-renowned researcher of the Moon, worked in the Engelhardt Astronomical Observatory (EAO), situated in a forest, 20 km from Kazan, from 1928 till his death in 1949. Oleg graduated from Kazan State University (KSU) in 1957, as radio physicist. His first work was as engineer in the radio astronomical laboratory in KSU. In 1964 he got his first scientific degree (candidate of science – an equivalent of Ph.D.). From 1965 to 1970 Oleg worked as an assistant and assistant professor in the radio astronomy department at KSU. In the years 1966–1967 he completed a scientific internship in England, at the University of Sheffield, working with the famous meteor researcher Professor T.R. Kaiser.

In 1970, Oleg transferred to work in the EAO as a deputy director for scientific work, at the same time he served as the head of the meteor department. In 1977–1991 he served as director of the EAO. Being director of the observatory, he had to deal not only with scientific, but also with organizational and economic work. The astronomical observatory is an autonomous institution in which the director is obliged to ensure not only the coordination of scientific research, but also the normal living conditions on its territory for more than 150 scientists and members of their families. Nevertheless he found time to gain his second scientific degree (D. of Sci.) in 1988.

¹Email: goryabova@gmail.com



Figure 1 – March 30, 1991, Simferopol, the Crimea. A meeting at Crimean meteor station. Belkovich O.I., Ryabova G.O., Levina A.S. and Martynenko V.V.



Figure 2 – Oleg Belkovich lecturing at the Radio Meteor School 2005 in Oostmalle.

In 1991 Oleg resigned to devote most of his time to science, and had the position of principal researcher. He also was professor in Kazan University for almost two decades (1996–2014). Oleg was member of the International Astronomical Union from 1966 onwards, and in 1982 he was elected as President of IAU Commission 22 for the following triennium. Since 2005, Oleg was Honorary Member of the International Meteor Organization.

As a professional astronomer, Oleg Belkovich focused on the study of radar observations of meteors. He began with the development and improvement of equipment for radar observations of meteors, and took a direct part in the observations. The work started originally as military research on communications via meteors, but later evolved into the study of radar meteors themselves. Later Oleg became more involved with theoretical work regarding the interpretation of radar observations. Oleg proposed a new, probability-based approach to processing and interpreting the radar observations of meteors. For the first time in the world, he obtained the distribution of the amplitudes and durations of meteor echoes in an analytical form, considering the random positions of the reflecting points on the meteor trails. The method allows calculation of the incident flux density for a meteor shower, which is one of the basic problems of meteor astronomy. Asteroid 179595 Belkovich (2002 MK₄) is named in his honor for his work in radar observations of meteors.

It would not be an exaggeration to say that Oleg Belkovich was an eminent meteor astronomer. Some of his numerous students are now doctors and professors and continue his work in astronomy. Still, he always had time for collaboration with amateur meteor astronomers, highly appreciating the scientific value of their efforts. In co-authorship with amateur meteor astronomers from Crimea, he published research papers in WGN, and he participated in several International Meteor Conferences, organized by IMO.

Till the end of his life Oleg lived and worked in EAO, and he was buried there as well. He found his peace, and we lost a devoted and passionate teacher, colleague, friend and a very kind, affable man.

When I (Cis Verbeeck) first met Oleg at the IMC 1991 in Potsdam, he made a big impression on me. As a young amateur astronomer, I was too shy to approach him. When me and my friends from the Belgian RAMSES radio team did approach him at the IMC 1993 in Puimichel, Oleg was very patient with our questions and encouraged us in our radio meteor work. The correspondence continued after the IMC and Oleg invited us to his observatory in Kazan. So in the summer of 1994, Oleg tutored us in radio meteor astronomy during the Meteor Summer School in EAO. We were very honored and amazed that Oleg spent two weeks of his time to teach us, young amateurs, about meteor astronomy, and much more than that. He received us in his own house as a very kind and warm host, we spent time socializing, enjoying the lovely EAO neighborhood and some Russian culture, and he introduced us to several distinguished researchers. Our visit to Kazan inspired us to pursue radio meteor astronomy studies for many years to come.

At the occasion of the IMC 2005 in Oostmalle, the Belgian LOC got the idea to organize a Radio Meteor School (RMS) for devoted amateur meteor astronomers. When we asked Oleg to be the main teacher, he immediately agreed, and he went to great lengths to explain his theoretical work on radio meteors. During five days, participants listened to lectures, alternated with “study time” and Q&A sessions. As a result, and after many e-mail interactions with Oleg afterwards, the 130-page volume of the RMS 2005 Proceedings was born. This is by far the most fruitful collaboration I have personally had in meteor science to date, and I am very grateful to Oleg for his nonrelenting enthusiasm and willingness to help.

IMO bibcode WGN-483-ryabova-belkovich NASA-ADS bibcode 2020JIMO...48...57R

Registration for the online IMC 2020 is open!

IMO Council and IMC 2020 LOC and SOC

In view of the risks and evolving policies regarding COVID-19, IMO and the Local Organizing Committee cannot guarantee the successful organization of the IMC 2020. Hence, we have decided to cancel the IMC 2020 in Hungary.

People who had already registered will get a total refund of the money they have paid for their participation in the IMC 2020.

If COVID circumstances allow, the IMC 2021 will take place in Hungary, at the place where the IMC 2020 was originally planned to take place.

We regret that the IMC 2020 will not take place in a physical way. In order to accommodate the need to present new results to the meteor community, we organize a **one-day online IMC on Saturday, September 19**.

In order to register for attendance of the online IMC, please send an e-mail to imc2020@imo.net, mentioning your name and affiliation. In case you want to present a talk, please add the authors, title, abstract and duration (15 minutes max). The deadline for both registration and submitting an abstract is September 5, but **please submit asap** because the time leading up to the IMC is very short now.

Program and connection details will follow in due time.

We hope to meet you at the online IMC on September 19!

IMO bibcode WGN-483-council-cancellation NASA-ADS bibcode 2020JIMO...48...59C

Meteor science

Seven years of bright meteor data from the NASA All Sky Fireball Network

Aaron Kingery¹, Danielle E. Moser², William J. Cooke³, and Althea V. Moorhead^{3,4}

We announce the public release of an archive of bright meteor data (complete to an absolute meteor magnitude of about -4) from the NASA All Sky Fireball Network. The data include basic trajectory information, brightness measurements, and derived orbits for 33 660 meteors collected between 2013 January 1 and 2019 December 31. This paper provides a brief description of the hardware and software used to make these meteor observations and discusses the general characteristics of and known sources of error in the data.

Received 2020 June 1

1 Introduction

The NASA All Sky Fireball Network is a low-cost network of simple automated video cameras used to detect and characterize bright meteors over the United States. It is operated by the Meteoroid Environment Office (MEO) at Marshall Space Flight Center in Huntsville, Alabama. The network was first established in 2008 and initially consisted of just two cameras located in Huntsville and Chickamauga, Georgia (Cooke and Moser, 2012). Over time, we have added additional stations, as listed in Table 1. The network currently consists of 16 cameras grouped into five clusters in different areas of the continental United States (see Figure 1).



Figure 1 – Locations of NASA All Sky Fireball Network camera stations (red dots) in 2020. The red circles surrounding the stations are 600 km in diameter and represent the approximate range of each camera.

The network was established with the following aims: [1.] measuring the speed distribution of centimeter-sized meteoroids, [2.] determining which sporadic sources produce large meteors, [3.] measuring orbits for bright meteors, [4.] determining the size at which shower meteors outnumber sporadic meteors, [5.] monitoring the activity of major meteor showers, and [6.] assisting in the location of meteorite falls (Cooke & Moser, 2012).

¹ERC, Inc., Marshall Space Flight Center, Huntsville, Alabama 35812

²Jacobs Space Exploration Group, Marshall Space Flight Center, Huntsville, Alabama 35812

³NASA Meteoroid Environment Office, Marshall Space Flight Center, Huntsville, Alabama 35812

⁴Email: althea.moorhead@nasa.gov

Table 1 – NASA All Sky Fireball Network station number, location, and date established, from 2008 to present. *Stations 8 and 15 were decommissioned in Oct 2019 and Dec 2014, respectively.

Num.	Location	Date est.
1	Huntsville, AL	Jun 2008
2	Chickamauga, GA	Oct 2008
3	Tullahoma, TN	Jan 2011
4	Cartersville, GA	Mar 2011
5	Las Cruces, NM	Sep 2011
6	Mayhill, NM	Sep 2011
7	Rosman, NC	Apr 2012
8	Dahlonaga, GA*	Jul 2012
9	Kitt Peak, AZ	Aug 2014
10	Mt. Lemmon, AZ	Aug 2014
11	Mt. Hopkins, AZ	Aug 2014
14	Pittsburgh, PA	Aug 2013
15	Oil City, PA*	Aug 2013
16	Oberlin, OH	Aug 2013
17	Hiram, OH	Aug 2013
18	Daytona Beach, FL	Oct 2017
19	Orlando, FL	Oct 2017
20	Cape Canaveral, FL	Oct 2017

The achievement of some of these goals (notably goals 1 and 4) has been hampered by the large uncertainty present in the luminous efficiency (see, e.g., Subasinghe et al., 2017), but we have fulfilled others. Contributions from all sporadic sources are visible in our data and we have used our all-sky data to study individual showers (Moorhead et al., 2015; Campbell-Brown et al., 2016; Blaauw, 2017; Sato et al., 2017; Tsuchiya et al., 2017) and conduct shower surveys (Burt et al., 2014; Moorhead, 2016; Sugar et al., 2017). The network has detected at least two meteorite falls: our cameras saw the Dishchii’bikoh fall (Jenniskens et al., 2020) in 2016 and the Hamburg fall (Brown et al., 2019) in 2018, and our data were used to help characterize the Hamburg fall.

In recent years, the network has also assisted our office in fulfilling a new required function. While the MEO is primarily tasked with monitoring and modeling the meteoroid environment in support of spacecraft risk assessments, a second function of our office is to analyze bright bolides of public interest (Moser, 2017). Where

possible, all-sky camera data is used to obtain rapid and reasonably accurate trajectories for these events. Our network has thus become an important tool for answering these queries.

2 Data collection

Our camera network is modeled after the Southern Ontario Meteor Network (SOMN; Weryk et al., 2008; Brown et al., 2010a); it implements a similar camera design and utilizes the All-sky and Guided Realtime Detection (ASGARD) meteor detection software and analysis pipeline (Weryk et al., 2008). The following subsections provide details about the network hardware and software.

2.1 System components

The NASA All Sky Fireball Network consists of a collection of camera stations and a central server. Each station in turn consists of a camera, desktop computer, and a Global Positioning System (GPS) receiver. We will use the term “camera” to refer to the camera and attached hardware, “camera station” to refer to all components housed at a particular site, “cluster” to refer to groups of stations with overlapping fields of view, and “network” to refer to all camera stations plus the central server to which they report.

The cameras are Watc 902H2 Ultimate charge-coupled device (CCD) video cameras; these black-and-white security cameras are favored by amateur astronomers due to their sensitivity and affordability. Each camera is equipped with a fish-eye lens with a variable focal length between 1.6 and 3.4 mm (which we set to 2 mm), an f-ratio of 1.4, and a field of view that extends almost to the horizon (see Figure 2). Cameras are housed in a simple weatherproof structure consisting of a PVC pipe and clear acrylic dome. Micro-fans and either resistors or a heating strip provide thermal control and reduce moisture build-up in the housing. A daylight sensor automatically turns the camera on each evening and shuts it down each morning. A diagram of the interior of an all-sky camera is presented in Figure 3, and Figure 4 shows how the electronic components of the camera are connected.

The station computers are relatively cheap, off-the-shelf basic PCs running Linux. Only one special hardware component is added: a commercial frame-grabber card that digitizes the camera video at 30 fps with 640×480 resolution. The GPS receiver is connected directly to the computer; it is not a part of the camera. The GPS receiver is used to determine the time of each video frame of the event, and, in some cases, to establish the location of the camera.

Our all-sky camera stations are placed no more than 145 km apart so that most of each camera’s field of view overlaps with that of another camera and meteors can thus be detected by multiple cameras. They are placed no less than 65 km apart to permit effective triangulation of jointly detected meteor’s position.

Stations are established and operated under partnerships between NASA and each site, usually codified



Figure 2 – Composite image of an Orionid meteor detected by the NASA All Sky Fireball Network on 2014 October 17. This image illustrates the basic characteristics of our meteor imagery: black-and-white images, a large field of view that encompasses most of the horizon, and the ability to detect a few stars (the constellation Orion is easily seen in the lower left quadrant). Images are oriented with north at the top and west to the right.

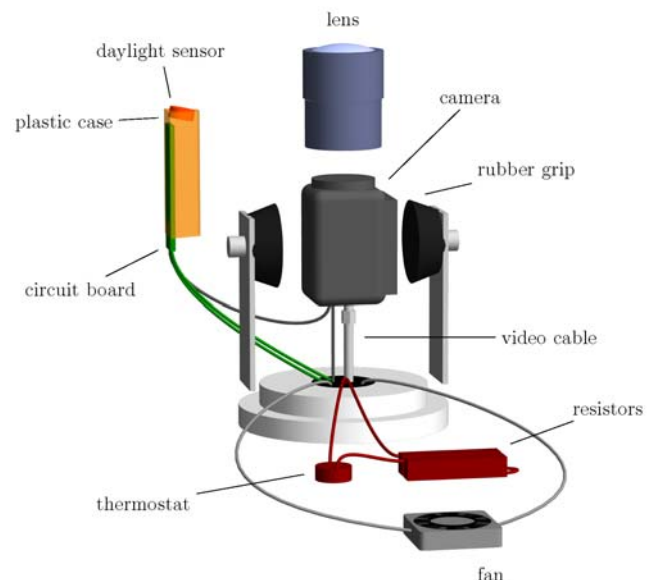


Figure 3 – Diagram of the basic components of the interior of a NASA all-sky meteor camera. This diagram is not precisely to scale, and objects have been spatially separated and in some cases colored to help distinguish between components. We have also omitted the screw terminal through which wires are connected.

in the form of a Space Act Agreement. The partner hosts the equipment, providing power and a stable internet connection, while NASA provides the camera, a computer equipped with ASGARD, the GPS receiver, and associated peripherals.

2.2 Detection and correlation

Our station computers utilize the ASGARD software to detect meteors (Weryk et al., 2008; Brown et al., 2010a) by comparing pixel brightness in video frames. If at least one pixel increases in brightness to above a set threshold for several frames, this triggers the station to consider it a possible event. The event “ends” when the brightness decreases again to below a second threshold.

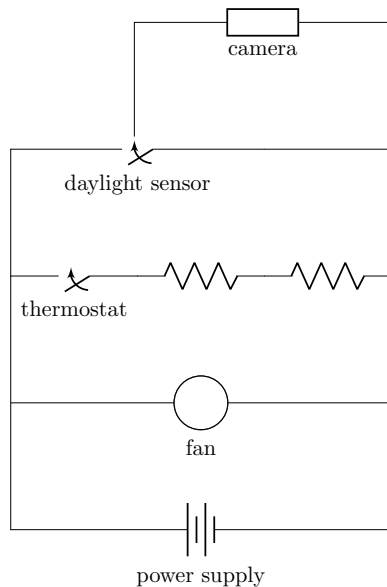


Figure 4 – Circuit diagram for a NASA all-sky meteor camera.

For each event, the camera system saves a compressed video file, uncompressed individual video frames as still images, a composite image (i.e., a stacked image of all video frames), and a summary text file noting the pixel location of the event in each frame using a center-of-light algorithm. All of this is completed in real time by the station computer.

We create monthly astrometric calibration files (“plates”) for each camera; this is a manual task that uses the process of Ceplecha (1987). These calibration files map the pixel coordinates to local azimuth and zenith distance angles. The computers also generate monthly photometric offsets that are used to map the total pixel counts to apparent magnitude. The plates and the photometric offsets are obtained by comparing the observed positions and brightness of stars with Sky2000 R-band magnitudes (Myers et al., 2001).

Event correlation is performed by the central server. Each camera system reports events to the server every 30 minutes during the night. In the morning, the server correlates events by time within each camera cluster. Events observed by different cameras in the same cluster are considered to be the same event if the observation time (specifically, the time at which peak brightness occurs) for each differs by less than five seconds.

A variety of non-meteor events can produce temporary but detectable increases in brightness. Airplanes, satellites, headlights, lightning, and fireflies have all been recorded as “events” by camera stations. A dark object, such as a bird, moving in front of a moon-lit cloud background can also trigger *ASGARD*’s detection algorithm. Some of these false positives (such as insects and birds) are seen by only camera and are therefore excluded from the data, but requiring detection of an event by multiple stations is not sufficient to exclude all false positives. To further reduce the number of false positives, *ASGARD* applies a variety of filters to exclude events that are, for instance, overly long, move too little, move irregularly, or are too close to the Moon.

At times, *ASGARD* is overzealous in excluding events and can reject actual meteors. In an effort to retain as much meteor data as possible, we have developed a GUI that a member of our office uses to visually inspect each night’s “rejects.” Based on the path of the meteor across each camera’s field of view and the associated light curves, the user can override *ASGARD*’s classification and put the event back in the queue for further analysis (see section 2.3).

2.3 Trajectory and orbit analyses

Correlated events – those that are detected by at least two cameras and have passed either *ASGARD*’s filters or visual inspection – are automatically analyzed on the server. The atmospheric trajectory is determined using the program *MILIG* (Borovicka, 1990); a full description of the “straight least-squares method” can be found in that paper. The geocentric meteor position as a function of time in rectangular and WGS84 coordinates, the apparent meteor radiant in geocentric rectangular and equatorial coordinates, the convergence angles, the topocentric azimuth and zenith distance, and the average atmospheric meteor speed are calculated and output by *MILIG*.

The heliocentric orbit is calculated using the program *MORB* (part of the program *FIRBAL*; Ceplecha, 1987). The average observed velocity is corrected for Earth’s rotation and gravity. The meteor radiant is also corrected and transformed to J2000 geocentric radiant coordinates. The heliocentric velocity and ecliptic latitude and longitude are calculated using the geocentric velocity and radiant position. The J2000 orbital elements follow from these quantities.

The data pipeline and analysis are automated and meteor results are stored in a database; the most recent three weeks of data are available through a public website^a.

2.4 Shower association

To determine shower association, the date of the event, the radiant, and the velocity are compared to a reference shower table taken from Brown et al. (2010b). Events are marked with the corresponding three-letter meteor shower code if the event date falls within the shower’s period of activity, the meteor’s geocentric radiant falls within 7.5° of the reference shower radiant (taking radiant drift into account), and the geocentric velocity is within 20% of the reference velocity.

3 Data description

The first of our meteor cameras were deployed in 2008, but many fewer camera stations were operational in these early years and the data outputs were not yet in their current form. Thus, we limit our data release to those meteors seen between 2013 January 1 and 2019 December 31 (inclusive).

These data are provided in a file named `nasfn_2013-2019_data.txt`, which we have placed on

^a<https://fireballs.ndc.nasa.gov>



Figure 5 – Distribution of the locations of events detected by our camera network.

our public server^b. The data file is accompanied by a file named `nasfn_2013-2019_readme.txt` that explains each data field and specifies units (typically degrees for angles, km for heights, km s^{-1} for speeds, and au for orbital distances). We also describe these data fields in this section.

These events are not evenly distributed over our network. Local weather and establishment date affect the number of meteors seen by each camera. Figure 5 shows the location distribution of events.

3.1 Trajectory and brightness

All data presented in our master file are derived quantities; the raw data are the video files and still images. This subsection, however, describes the data fields that are more closely related to our observations of meteors in the atmosphere, while the next subsection describes the meteoroid’s motion before it encounters the Earth.

First, we provide information on the time of the event. The first field specifies the date and time at which the meteor peaks in brightness (in ‘YYYYMMDD-hh:mm:ss’ format). The second field provides the corresponding numeric Julian date, and the third field provides the corresponding solar longitude (`slon`).

Next, we provide a few parameters that reflect how well the meteor was observed. The fourth field (`n`) specifies the number of camera stations that observed the meteor, which never can be less than 2. The fifth field (`Qstar`) gives the maximum convergence angle, which we term ‘`Q*`’. The sixth data field is a saturation flag (`sat`) that indicates whether the meteor’s brightness exceeded the maximum in any pixel in any camera.

The next 13 fields describe the start and end positions of the meteor and the duration of the event. Each position is specified in terms of latitude, longitude, and height above the ground; the characters “1” and “2” indicate whether the coordinate belongs to the start or end of the event (i.e., `lat1` is the latitude at which the event begins). Latitudes and longitudes are given in degrees north and east, respectively, and heights are given in km. The uncertainty in each quantity is also given and is indicated by prepending “d” to the variable name (e.g., `dlat1` gives the uncertainty in `lat1`). Finally, we provide the duration of the event in seconds (`dur`). Figure 6 displays a sample set of meteor



Figure 6 – Ground tracks (white arrows) of Geminid meteors observed over a section of central Florida by the NASA All Sky Fireball Network between 05:30 and 07:30 UT on 2017 December 14. The large lake near the center of the image is Lake George and the coastal city partially visible at right is Daytona Beach.

ground tracks produced by the server during the 2017 Geminids.

We also provide two measures of the meteor’s brightness. The first is the peak absolute meteor magnitude of the event (`mag`), and the second is the integrated luminosity, or total luminous energy, of the event (`L_int`; see Campbell-Brown and Koschny, 2004). These quantities can be combined with an assumed luminous efficiency to compute an estimated mass (see, e.g., Verniani, 1973). Figure 7 presents the distribution of peak magnitudes in the archive. The median value is -3.28 and, based on the interval over which the data follow a power law, detection appears to be complete to a magnitude of about -4 . The relative lack of very bright meteors in Figure 7 also indicates that saturation starts to play a significant role for meteors with an absolute magnitude of approximately -7 or brighter. The slope of this power law is equivalent to a population index of 2.2, but, because our cameras are by no means scientific grade, this should be taken as a test of reasonableness and not a reliable measurement of the true population index; additionally, any measurement of the sporadic population index would require careful removal of shower meteors.

The quantities mentioned so far fully describe a meteor event. However, we also provide a number of derived properties that are likely to be of interest to any users. The first of these properties are the apparent azimuth and zenith angle of the meteor as it passes through the atmosphere. The zenith angle (`rho_p`) measures the angle between the zenith and the meteor’s path; when this angle is zero, the meteor’s path is perfectly vertical. The azimuth (`eta_p`) measures the angle from the northward direction; when this angle is zero,

^bhttps://fireballs.ndc.nasa.gov/public_data/nasfn_2013-2019.zip

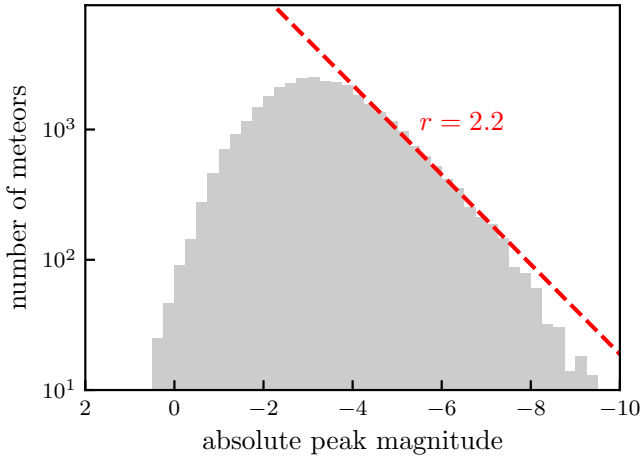


Figure 7 – Distribution of peak magnitudes from our meteor data archive. We highlight the portion of the distribution that appears to obey a power law (dashed line).

the meteor appears to come from due north, and when it is 90° , it appears to come from due east. We also provide the average in-atmosphere velocity of the meteor (v_p), and the uncertainty associated with each of these quantities ($drho_p$, etc.).

3.2 Radiant and orbit

ASGARD uses the program MORB to compute the radiant and orbit of the meteoroid before it encounters the Earth. In this section, we describe each of the associated parameters.

This includes the geocentric meteor radiant and speed (v_g). The radiant is expressed first in terms of right ascension (alp_g) and declination (dec_g), but we also provide the equivalent ecliptic longitude (lam_g) and latitude (bet_g). One can subtract the solar longitude from this ecliptic longitude to put the radiant in a Sun-centered ecliptic frame. We provide estimated uncertainties for each term (e.g., $dalp_g$). The distribution of Sun-centered ecliptic meteor radiants is presented in Figure 8; note the tendency of our optical, northern-hemisphere network to detect only nighttime meteors and to preferentially detect those at northern latitudes.

We also provide the nominal orbital elements that correspond to the meteor’s geocentric trajectory, including perihelion distance (q), eccentricity (e), inclination ($incl$), argument of perihelion ($omega$), and longitude of ascending node ($anode$). We use cometary orbital elements (i.e., we provide q rather than a) because our meteoroid orbits are often quite eccentric. We do not provide uncertainties for the orbital elements; the uncertainties in the low-precision trajectories produced by our all-sky system correspond to large, asymmetric regions of orbital element parameter space (this is discussed further in the next section).

The geocentric trajectory and orbital elements are used to classify the meteors in two ways. First, we use the solar longitude and geocentric radiant and speed to associate meteors with known showers (see section 2.4). If associated with a shower, this field (shw) provides the three letter shower code; if not, we indicate that the

meteor is a sporadic using the string “...”. Second, we use the orbital elements to compute Tisserand’s parameter with respect to Jupiter:

$$T_J = \frac{a_J}{a} + 2 \cos i \sqrt{\frac{a}{a_J} (1 - e^2)} \quad (1)$$

where semi-major axis is $a = q/(1 - e)$ and a_J is the semi-major axis of Jupiter.

We have found that MORB can sometimes enter an infinite calculation loop when the in-atmosphere velocity is less than 13 km s^{-1} . For this reason, users will find that our archive does not provide geocentric radiants and orbital elements for meteors below this speed limit; values of zero are substituted.

3.3 Caveats and pitfalls

This data is not manually curated and contains false positives. Some of these events, such as those caused by insects, are seen only in one camera and thus are not considered events by the server. Others produce events but are later filtered out. Figure 9 displays several images from our cameras that triggered ASGARD’s detection algorithm but were correctly filtered out from the final data archive. Some events are listed in the data twice, 20191230-10:31:52 for example. This can occur when the meteor is seen by two different clusters of cameras.

These filters are imperfect, however, and some non-meteor events are present in our archive. Figure 10 displays one such example. In this case, light reflected off the edge of a raindrop on the Chickamauga camera, triggering a detection. At nearly the same time, strong wind slightly displaced the Huntsville camera mount, causing a perceived shift in the position of the lightning rod in the field-of-view. This brief change created a linear feature at the rod’s pre-shift location, and previously dark pixels were illuminated by a bright sky, thus triggering a detection. Although we know this event to be a false positive, we have left it in the data as a representative of other, unknown false positives. The only events within the given time range that we have excluded are those whose uncertainties are so large that they break the formatting of our table.

The bit depth of the Wattec cameras is relatively small (8-bit), and as a result many events are flagged as saturated in our cameras (46%; although, as discussed in section 3.3, our saturation flagging is aggressive). A bright, saturated meteor produces a large number of pixels of equal (maximum) brightness in the camera images, making it difficult for ASGARD to track the meteor properly. Features such as hot pixels and background stars are not masked and can “pull” the apparent center of light off the meteor. Figure 11 presents an example of a poorly tracked meteor. Thus, lower confidence should be placed in the trajectory solutions of saturated meteors.

Hot pixels, background stars, and saturation also affect our magnitude estimates. Figure 7 shows a deficit of events at the bright end of our distribution compared to our power-law fit. This is likely due to the brightness of these events being underestimated due to saturation.

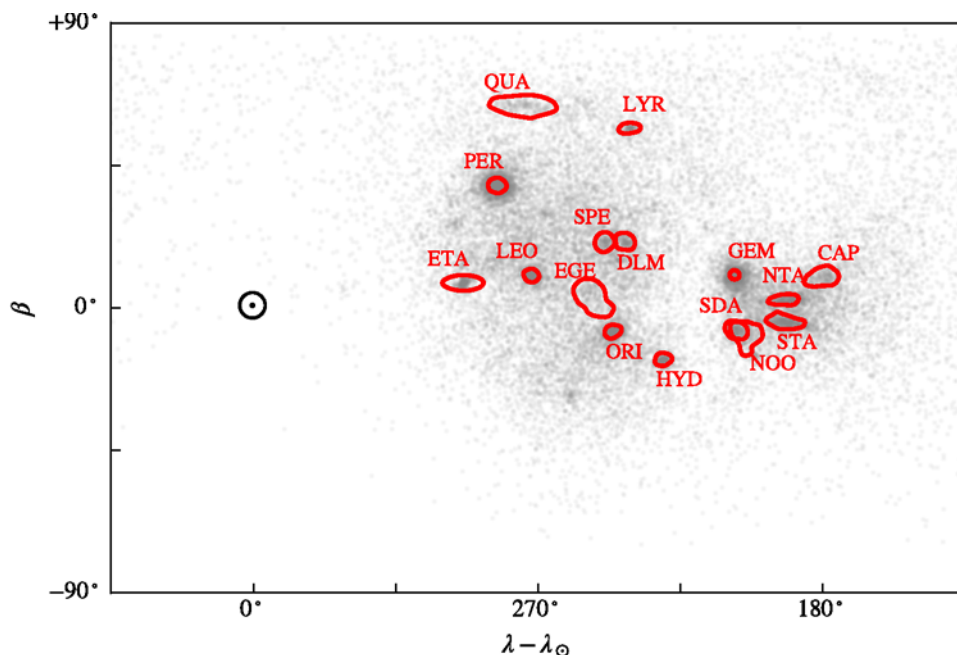


Figure 8 – The radiants of meteors seen by our network, in Sun-centered ecliptic coordinates. Major meteor showers are circled and labeled in red. The ‘ \odot ’ symbol marks the sunward direction.

Variations in the background light level, as well as contamination by hot pixels and background stars, will result in a varying saturation threshold, but saturation typically sets in for apparent magnitudes somewhere between -5 and -6 . Because most of our meteors will have a range greater than 100 km, this serves as a lower limit for saturation in absolute magnitude. Additionally, the Wattec cameras are not scientific grade cameras and have a unique spectral response. Thus, the magnitudes measured by these cameras likely differ from the true (visual) magnitudes of the detected meteors.

The programs MILIG and MORB generate uncertainty estimates in the meteor’s trajectory. However, these values describe only the uncertainty in the orbital fit, and do not include sources of uncertainty such as errors in determining the center of light or distortion in the images near the horizon. Thus, they are strict underestimates of the true uncertainty. They can be used as rough indicators of precision but should not be used to constrain, for example, the possible orbits for a particular meteoroid. To illustrate this, we have computed the possible orbits corresponding to a meteor with $1\text{-}\sigma$ uncertainties of 5° in the ecliptic geocentric radiant and 20% in the geocentric speed (see Figure 12). We find that these types of errors can result in a huge range of possible orbits and Tisserand parameters, and thus caution against using these data to study the dynamics of an individual meteoroid. We specifically warn against using these data to identify supposed interstellar meteoroids due to the lack of reliable uncertainties. However, these data can be used to study shower and sporadic meteor activity at large sizes, and occasionally to support meteorite hunts.

We also encourage users to take our meteor shower membership identifications with a grain of salt. The shower identification algorithm is crude and makes no assessment of the probability of membership. The num-

ber of meteors belonging to large showers, such as the Perseids, may be underestimated, and the number of meteors belonging to small showers overestimated. Users interested in studying showers should consider applying their own shower extractions on the data.

We also caution against using the raw numbers of meteors to compare shower activity year-to-year. While the data can be used to confirm unusual outbursts such as the May Camelopardalids (Campbell-Brown et al., 2016) and December Phoenicids (Sato et al., 2017) in 2014, the data cannot be used in the current form to compare, for example, the activity of the eta Aquariids over time. We do not yet have reliable measures of the number of clear hours per camera per night, and efforts to characterize the collecting area are underway but not complete. Without this information, it is not possible to measure meteor fluxes or to conduct reliable activity comparisons.

If a user wishes to study the meteors in our database in aggregate, there are a number of possible quality cuts that can be applied. For instance, we often require that the maximum angle of convergence (Q^*) exceeds 15° and that the estimated uncertainty in the in-atmosphere velocity be no greater than 20%. One could additionally require that events not be saturated, that the start height be greater than the end height ($H_{\text{beg}} > H_{\text{end}}$), or that each event be seen by at least three cameras. However, we note that the saturation flag is fairly aggressive and can be triggered by the meteor simply overlapping with a hot pixel in a single video frame. The exact set of quality cuts may depend on the application: to give a possible example, the requirement that the start height not exceed the end height could impede a search for meteors that “graze” the atmosphere. Thus, we have not applied any such cuts to this data release, instead leaving it to the user to choose quality cuts that are appropriate for their project.

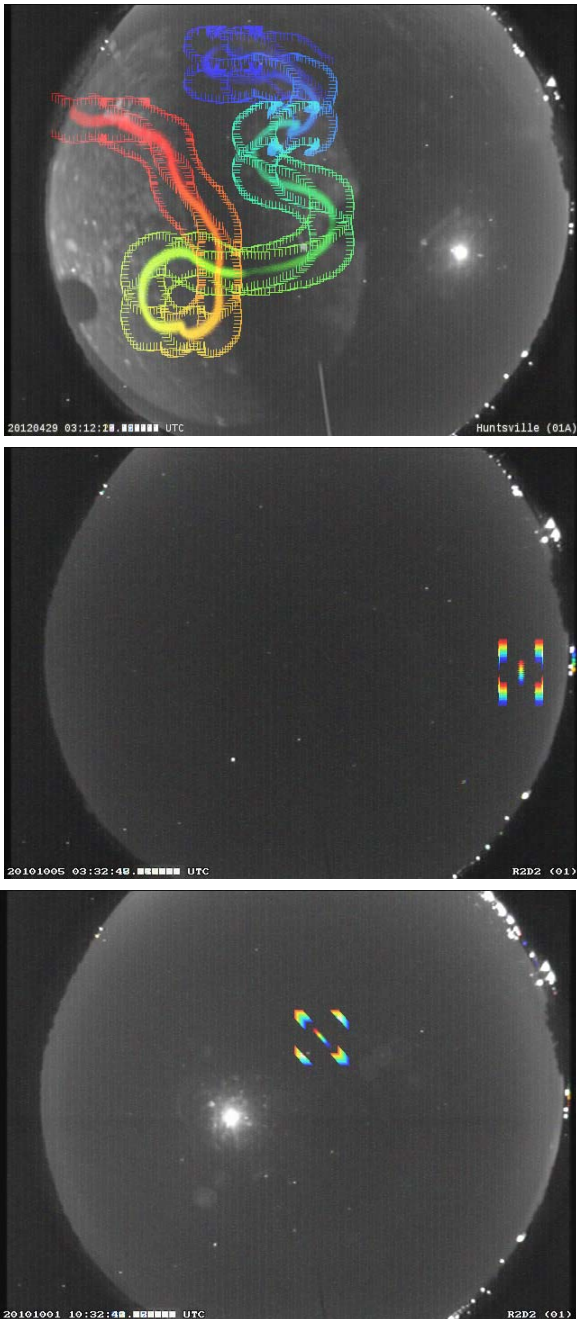


Figure 9 – Examples of non-meteor events (an insect, top; an airplane, center; and the International Space Station, bottom) that were filtered out of the data by **ASGARD**. These images have been generated by colorizing individual frames of a video and re-combining them; color therefore indicates movement.

4 Future Work

We plan to make improvements to both our hardware and analysis routines in the future. This section outlines several such improvements that we plan to implement over the next few years.

First, we plan to update our camera hardware. The Watco camera models that we use have been discontinued, making it necessary to find a replacement. Ideally, we will replace these cameras with alternatives that offer a higher bit depth, frame rate, and resolution. There are cameras such as the Blackfly S GigE that offer these features and are commercially available.



Figure 10 – Light reflecting off a raindrop on the camera dome located in Chickamauga triggered a false event detection on 2013 July 11. This false positive has a time-stamp of 20130711-04:03:00 and is present in our data archive.



Figure 11 – Stacked video frames of a poorly tracked meteor. In each frame, **ASGARD** marks the meteor's location by drawing the corners of a square around it. One can see that when the meteor is at its brightest, these markers exhibit some left-right and up-down jitter, as the tracking jumps ahead to illuminated clouds in front of the meteor and then falls behind it to lock on the illuminated trail.

We also plan to update our analysis pipeline to include a saturation correction. We have developed a method to improve our estimates of the brightness of saturated meteors by using a LED to measure the camera response to saturated light sources, and we plan to incorporate this correction into our automated analysis routines. In parallel, our colleagues at the University of Western Ontario plan to make some minor corrections to **ASGARD**. For instance, the combination of codes currently used by **ASGARD** to convert in-atmosphere trajectories to orbits corrects for the Earth's rotation twice. This error is smaller than our typical uncertainties, but should nevertheless be repaired.

We have also begun to develop routines to characterize our collection area and convert our detection rates into meteor flux measurements (Ehlert & Blaauw Erskine, 2020). These methods cannot yet be automated due to the lack of cloud cover data; their use is currently limited to known clear nights during major meteor showers.

The expansion of our network has slowed in recent years and is close to the total number of cameras we are

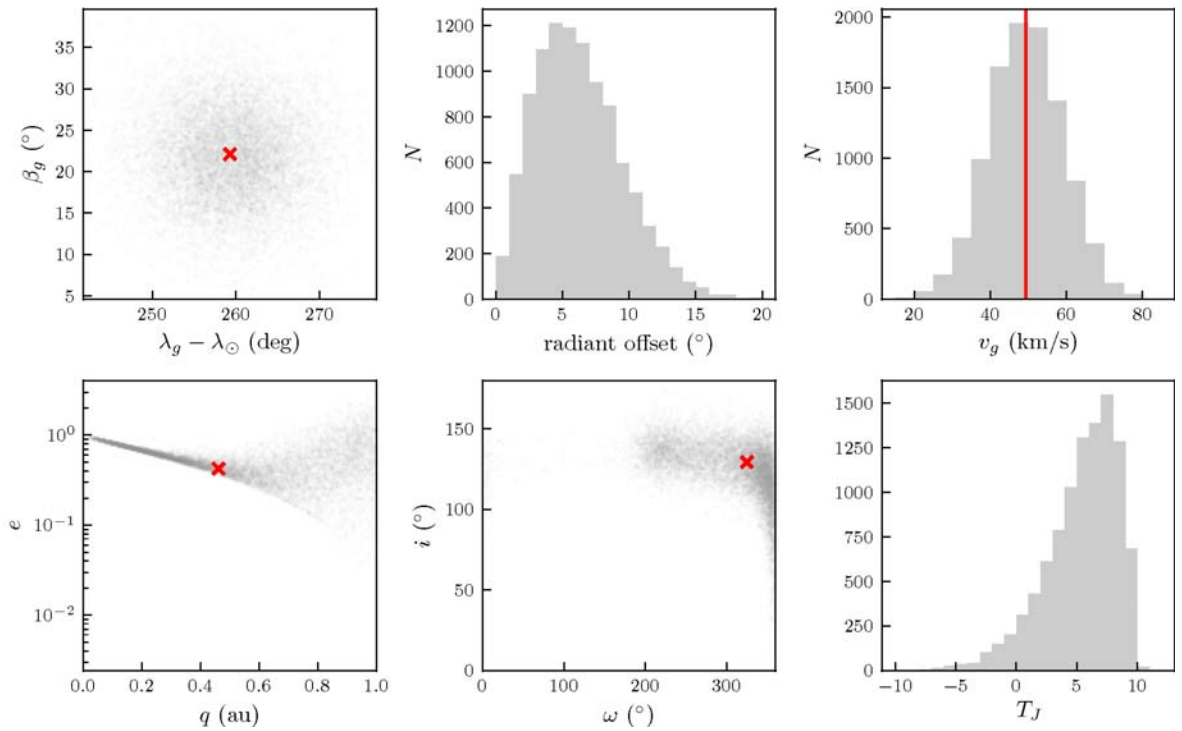


Figure 12 – Illustration of how a 5° dispersion in measured radiant and 20% dispersion in measured speed (see top panels) corresponds to a wide range of possible orbital solutions (lower panels). Red crosses and lines mark the nominal radiant, orbit, and speed, while gray dots represent other possible solutions that are consistent with the assumed uncertainty in radiant and speed.

capable of maintaining. Thus, we are unlikely to expand our network in the near future. However, interested potential hosts can email us^c if they would like to be contacted in the event of a network expansion in their area.

Finally, we would like to note that it is possible to use all-sky cameras for many other applications, including weather studies. We have, for instance, made incidental recordings of sprites and supplied these data to atmospheric scientists (Lang, 2017). However, our particular network cannot be altered to optimize lightning detections and our involvement in weather-related applications is likely to remain minimal.

5 Acknowledgments

We would like to thank our site partners, without whom our network would not exist. These partners are: Walker County School District and the Walker County Board of Education, Hands-On Science Center and the University of Tennessee Space Institute, Tellus Science Museum, New Mexico State University, New Mexico Skies Inc., Pisgah Astronomical Research Institute, University of North Georgia, Association of Universities for Research in Astronomy and Kitt Peak National Observatory, Arizona Board of Regents and the University of Arizona with Mount Lemmon Observatory and MMT Observatory, University of Pittsburgh and Allegheny Observatory, Oil Region Astronomical Society Inc., Oberlin College, Hiram College, Embry-Riddle Aeronautical University, University of Central Florida and the University of Central Florida Board of Trustees, and the NASA Kennedy Space Center.

^cMSFC-fireballs@mail.nasa.gov

We thank the meteor physics group at the University of Western Ontario – especially Peter Brown, Jason Gill, Zbigniew Krzeminski, and Rob Weryk – for providing the **ASGARD** meteor detection software, building some of our cameras, and providing assistance and advice in general. We also thank Jiri Borovička for providing the **MILIG** and **MORB** codes used for trajectory and orbit analyses. Finally, we thank Rob Suggs for helping to establish our network and providing advice and technical expertise, and Derek Peloquin and Chris Hozian for providing IT support.

This work was supported in part by NASA contracts 80MSFC18C0011 and NNM16AA01, by NASA cooperative agreement 80NSSC18M0046, and by the Natural Sciences and Engineering Research Council of Canada.

References

- Blaauw R. C. (2017). “The mass index and mass of the Geminid meteoroid stream as determined with radar, optical and lunar impact data”. *Planetary & Space Science*, **143**, 83–88.
- Borovička J. (1990). “The comparison of two methods of determining meteor trajectories from photographs”. *Bulletin of the Astronomical Institutes of Czechoslovakia*, **41**, 391–396.
- Brown P., Weryk R. J., Kohut S., Edwards W. N., and Krzeminski Z. (2010a). “Development of an All-Sky Video Meteor Network in Southern Ontario, Canada The **ASGARD** System”. *WGN, Journal of the International Meteor Organization*, **38:1**, 25–30.

- Brown P., Wong D. K., Weryk R. J., and Wiegert P. (2010b). “A meteoroid stream survey using the Canadian Meteor Orbit Radar. II: Identification of minor showers using a 3D wavelet transform”. *Icarus*, **207**, 66–81.
- Brown P. G., Vida D., Moser D. E., Granvik M., Koshak W. J., Chu D., Steckloff J., Licata A., Hariri S., Mason J., Mazur M., Cooke W., and Krzeminski Z. (2019). “The Hamburg meteorite fall: Fireball trajectory, orbit, and dynamics”. *Meteoritics and Planetary Science*, **54:9**, 2027–2045.
- Burt J. B., Moorhead A. V., and Cooke W. J. (2014). “A meteor cluster detection algorithm”. *WGN, Journal of the International Meteor Organization*, **42:1**, 14–19.
- Campbell-Brown M. D., Blaauw R., and Kingery A. (2016). “Optical fluxes and meteor properties of the camelopardalid meteor shower”. *Icarus*, **277**, 141–153.
- Campbell-Brown M. D. and Koschny D. (2004). “Model of the ablation of faint meteors”. *Astronomy & Astrophysics*, **418**, 751–758.
- Cepelcha Z. (1987). “Geometric, dynamic, orbital and photometric data on meteoroids from photographic fireball networks”. *Bulletin of the Astronomical Institutes of Czechoslovakia*, **38**, 222–234.
- Cooke W. J. and Moser D. E. (2012). “The status of the NASA All Sky Fireball Network”. In *Proceedings of the International Meteor Conference, 30th IMC, Sibiu, Romania, 2011*. pages 9–12.
- Ehlert S. and Blaauw Erskine R. (2020). “Measuring Fluxes of Meteor Showers with the NASA All-Sky Fireball Network”. *arXiv e-prints*, page arXiv:2004.07951.
- Jenniskens P., Moskovitz N., Garvie L. A. J., Yin Q.-Z., Howell J. A., Free D. L., Albers J., Samuels D., Fries M. D., Mane P., Dunlap D. R., Ziegler K., Sanborn M. E., Zhou Q., Li Q.-L., Li X.-H., Liu Y., Tang G.-Q., Welten K. C., Caffee M. W., Busemann H., Meier M. M. M., and Nesvorny D. (2020). “Orbit and origin of the LL7 chondrite Dishchii’bikoh (Arizona)”. *Meteoritics and Planetary Science*, **55:3**, 535–557.
- Lang T. J. (2017). “On the relationships between sprite production and convective evolution”. In *AGU Fall Meeting Abstracts*, volume 2017. pages AE21A–01.
- Moorhead A. V. (2016). “Performance of D-criteria in isolating meteor showers from the sporadic background in an optical data set”. *MNRAS*, **455:4**, 4329–4338.
- Moorhead A. V., Brown P. G., Spurný P., Cooke W. J., and Shrbený L. (2015). “The 2014 KCG Meteor Outburst: Clues to a Parent Body”. *The Astronomical Journal*, **150:4**, 122.
- Moser D. E. (2017). “Comparing eyewitness-derived trajectories of bright meteors to instrumentally-observed data”. *Planetary & Space Science*, **143**, 182–191.
- Myers J. R., Sande C. B., Miller A. C., Warren, W. H. J., and Tracewell D. A. (2001). “VizieR Online Data Catalog: SKY2000 Catalog, Version 4 (Myers+ 2002)”. *VizieR Online Data Catalog*, page V/109.
- Sato M., Watanabe J.-i., Tsuchiya C., Moorhead A. V., Moser D. E., Brown P. G., and Cooke W. J. (2017). “Detection of the Phoenicids meteor shower in 2014”. *Planetary & Space Science*, **143**, 132–137.
- Subasinghe D., Campbell-Brown M., and Stokan E. (2017). “Luminous efficiency estimates of meteors - I. Uncertainty analysis”. *Planetary & Space Science*, **143**, 71–77.
- Sugar G., Moorhead A., Brown P., and Cooke W. (2017). “Meteor shower detection with density-based clustering”. *Meteoritics and Planetary Science*, **52:6**, 1048–1059.
- Tsuchiya C., Sato M., Watanabe J.-i., Moorhead A. V., Moser D. E., Brown P. G., and Cooke W. J. (2017). “Correction effect to the dispersion of radiant point in case of low velocity meteor showers”. *Planetary & Space Science*, **143**, 142–146.
- Verniani F. (1973). “An Analysis of the Physical Parameters of 5759 Faint Radio Meteors”. *Journal of Geophysical Research*, **78:35**, 8429–8462.
- Weryk R. J., Brown P. G., Domokos A., Edwards W. N., Krzeminski Z., Nudds S. H., and Welch D. L. (2008). “The Southern Ontario All-sky Meteor Camera Network”. *Earth Moon and Planets*, **102:1-4**, 241–246.

Handling Editor: Javor Kac

This paper has been typeset from a L^AT_EX file prepared by the authors.

Encontreitor: First Radiants

Leonardo S. Amaral^{1,2}, Carlos A.P.B. Bella¹, Lauriston S. Trindade¹, Gabriel G. Silva^{1,3}, Rubens Damigle¹, Marcelo L.P.V. Zurita¹, Marcelo W.S. Domingues¹, Renato C. Poltronieri¹, Cristóvão J.L. Faria^{1,4}, Carlos F. Jung^{1,4}

This article presents the results of a new method implemented in the Encontreitor software (Amaral et al., 2018b). Twenty-three new radiants were found at first with this computational application. The software input is a set of meteor orbits extracted from databases from meteor video-monitoring networks, such as BRAMON (Amaral et al., 2018a), EDMOND (Kornoš et al., 2014a; Kornoš et al., 2014b; EDMOND, 2018) and SonotaCo (SonotaCo, 2009; SonotaCo, 2018), after applying the five steps of the method, the application provides a list of possible new radiants.

Received 2019 December 5

1 Introduction

The Encontreitor software was developed using the Visual Basic programming language and it implements features that allow it to execute the five steps described in the method proposed by Amaral et al. (2018a). The tool implements the calculation of the Drummond determinant D describing the orbital dissimilarity (Drummond, 1981; Galligan, 2001; Jopek et al., 2002). This also implements the Break-point+, Valdeitor and Lapdeitor methods (Amaral et al., 2018b). This software was used to discover the 23 radiants described in this article, in addition to being responsible for the tabulation of the data used to create the plots (see the interface shown in Figure 1).

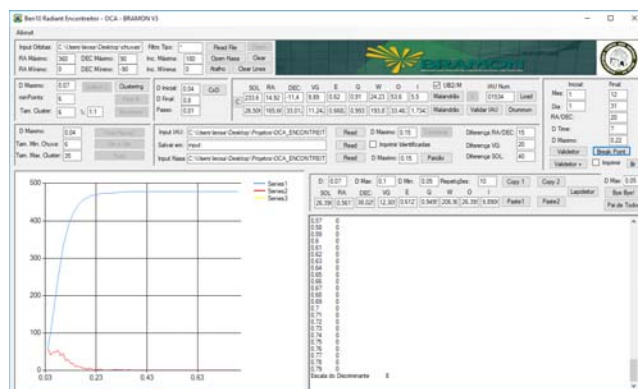


Figure 1 – Graphic Interface of the Encontreitor Software (Amaral et al., 2018b).

2 Reporting Radiants to the IAU

From May 2017 to January 2018, six reports of new radiants were sent to the IAU (International Astronomical Union) totalling 121 new radiants. These new radiants were found using the Encontreitor software and databases from the BRAMON, SonotaCo and EDMOND networks. This article presents the first 23 radiants found, as listed in Table 1. The three-letter codes as well as the designation of the showers are assigned by the IAU MDC.

The mean orbit generated by each radiant (see Table 1) has a low D value (always below 0.07) with respect to the meteors used to find each radiant. As described in Amaral et al. (2018a), the values listed in Table 1 comprise the radiant's nucleus and were used to generate the mean orbit.

Later in the paper we describe each of the 23 new radiants in detail. The results of the analysis are presented as a three-parameter plot (right ascension α – declination δ – geocentric velocity V_g) of the distribution of the orbits for each radiant. These plots were built from a search in the meteor orbit databases BRAMON, EDMOND, and SonotaCo, looking for orbits that are similar ($D \leq 0.22$) to the mean orbits associated to the meteors of the radiants. Breakpoint+ and Valdeitor plots are also be presented. Details on how these methods work and explanations of the graphs can be found in (Amaral et al., 2018b). These plots allow us to understand how meteors defining a radiant are related to meteors of other radiants.

All radiants described have been tested against all radiants in the current IAU database in order to ensure that they have a high orbital distance to other existing radiants.

3 Radiants

3.1 NEC – November Cetids

Before Encontreitor was created, two radiants were found by BRAMON using visual data (described by Trindade et al., 2019). The NEC radiant was also visually identified and later detected by Encontreitor. Initially, in the search for this radiant, only the BRAMON orbit database was used. The NEC radiant marks a change in the methodology used by BRAMON in the search for new radiants.

¹BRAMON – Brazilian Meteor Observation Network, Nhandeara, Brazil

Email: carlos.pbella@gmail.com; lauristontrindade@yahoo.com.br; rubens.marreira@gmail.com; marcelozurita@gmail.com; marcelo@casb.com.br; rcpoltronieri@gmail.com

²OCA – Observatório Campo dos Amarais, Bilac, Brazil (MPC X74). Email: lsamaral-ios@hotmail.com

³Instituto de Química, Universidade de São Paulo, São Paulo, Brazil. Email: gabrielg@iq.usp.br

⁴SONEAR – Southern Observatory for Near Earth Asteroids, Oliveira, Brazil (MPC Y00). Email: cjacqueslf@gmail.com

⁵HELLER & JUNG – Space and Sky Observatory, Taquara, Brazil. Email: carlosfernandojung@gmail.com

Table 1 – New radiants found in this study. Number – number of orbits; parent – possible parent object.

Code	Name	λ_{\odot}	α	δ	$\Delta\alpha$	$\Delta\delta$	V_G	a	q	e	ω	Ω	i	Number	Parent
NEC	November Cetids	233.6	14.92	-11.4	0.3	-0.3	9.89	2.39	0.91	0.62	24.23	53.6	5.5	265	2016 BE ₁ , 2007 TW ₂₄ , 2014 UA ₈ ?
JCT	July Cetids	110.4	19.48	-7.7	0.9	0.5	66.2	3.67	0.99	0.73	20.0	290.0	153.7	28	
JCD	June Cetids	88.7	20.13	-23.23	1.3	0	62.52	10.22	0.92	0.91	330.05	268.71	128.46	7	
ADS	June Aquariids	91.7	333.6	-18.46	1.0	0.4	60.89	2.44	0.44	0.82	115.53	271.68	160.02	11	
LSA	Lambda Sagitariids	74.2	276.85	-24.76	0.6	0.1	35.15	2.00	0.16	0.92	138.8	254.23	6.06	77	
DGR	Delta2 Gruids	91.3	339.09	-43.41	0.0	0.0	53.12	6.50	0.52	0.92	91.66	271.29	102.14	6	
GSC	Gamma Sculptorids	86.6	348.21	-28.42	0.7	0.5	63.54	7.00	0.77	0.89	60.33	266.55	138.45	13	
SGI	June Sagittariids	72.8	277.58	-20.37	0.6	0.0	37.51	2.40	0.12	0.95	324.13	72.84	4.88	32	
FLO	February Leonids	329.6	166.57	4.13	0.6	-0.2	32.44	2.17	0.26	0.88	125.51	149.57	4.06	79	
PCS	Phi Capricornids	226.9	318.09	-19.26	-0.2	0.4	7.06	1.85	0.98	0.47	349.43	46.9	3.12	44	2009 WX ₇ , 2010 VW ₁₉₄ , 2014 WX ₄ , 2015 XM ₁₆₉ ?
USG	Phi Ophiuchids	50.7	251.03	-17.46	0.4	-0.04	35.73	2.43	0.17	0.93	317.06	50.74	6.78	67	
XCD	October Cetids	187.5	37.99	7.67	0.2	0.3	39.75	1.75	0.07	0.96	152.6	7.46	27.4	29	
LCP	Lambda Capricornids	202.1	326.12	-11.74	0.6	0.0	6.37	1.72	0.98	0.43	13.76	22.15	2.63	41	
NAA	November alpha Aurigids	231.38	80.64	47.24	0.1	0.0	45.05	5.50	0.22	0.96	304.45	231.38	65.12	39	
OAC	October alpha Camelopardalids	213.6	56.47	64.46	0.9	0.1	43.37	7.38	0.59	0.92	261.05	213.63	69.8	38	
CVD	January Canum Venaticids	304.4	185.86	40.48	0.0	0.0	47.37	6.50	0.52	0.92	269.19	304.43	79.28	43	
CVT	February Canum Venaticids	331.8	195.72	36.09	0.0	0.0	39.96	6.38	0.51	0.92	269.96	331.8	56.5	45	
PCI	42 Piscids	135.6	7.1	12.44	0.5	0.3	59.72	5.40	0.27	0.95	300.51	135.65	155.74	31	
OAG	October Aurigids	205.0	70.24	35.53	0.4	0.1	56.19	5.33	0.16	0.97	314.16	205.04	130.65	31	
SPS	Sigma Perseids	182.3	51.51	47.38	0.0	-0.1	55.37	3.00	0.51	0.83	274.85	182.29	115.54	32	
TRD	October Taurids	192.4	69.81	12.46	0.6	0.0	60.9	6.20	0.31	0.95	114.59	12.45	153.49	37	
DRP	December rho Puppids	251.2	124.4	-24.2	0.4	-0.1	53.67	8.78	0.79	0.91	54.41	71.23	97.11	26	

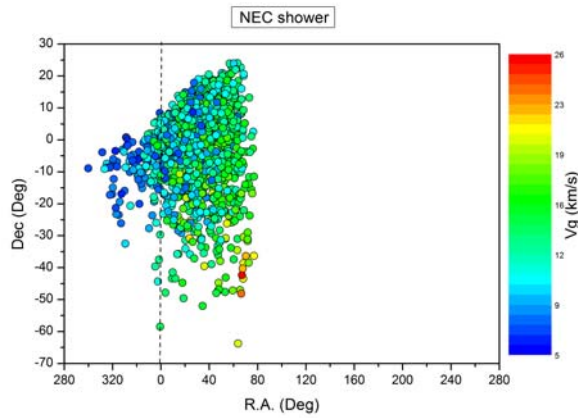


Figure 2 – Radiant of the November Cetids (NEC).

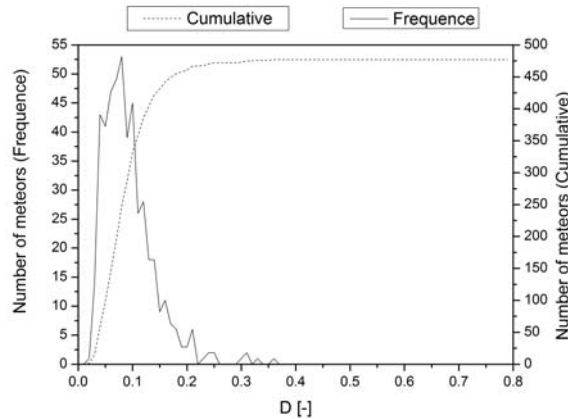


Figure 3 – NEC Break-point+ with a 20 degree radius.

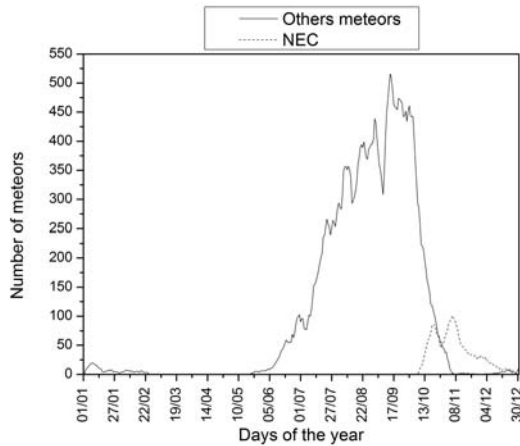


Figure 4 – NEC Valdeitor, 20° radius ($D \leq 0.22$).

Figure 2 presents the NEC radiant orbit distribution. It shows that the radiants cover a large area of the sky (right ascension from $\approx 300^\circ$ to $\approx 70^\circ$ and declination from $\approx -50^\circ$ to $\approx +25^\circ$). Further, we see an apparent velocity increase as the rights ascension increases and the declination decreases.

Figure 3 shows the NEC breakpoint+ plot, in which we can see that the plot's inflection point occurs very early, close to $D = 0.15$. This means that, despite being a radiant with few orbits recorded by now, they are well concentrated relative to the mean orbit found for meteors of this radiant (hereafter we use the shorter “radiant’s mean orbit”).

Figure 4 presents the Valdeitor plot (Amaral et al., 2018b). It shows the distribution of the orbits associated to the radiant as a function of the dates the meteors were captured. Only meteors within a radius of 20° around the radiant’s center are considered. The continuous line represents meteors not belonging to the radiant ($D > 0.22$), and the dotted line represents meteors belonging to the radiant ($D \leq 0.22$).

In this graph we can identify the formation of two maximum-activity peaks in the radiant. We also note the intense activity of meteors which do not belong to the NEC radiant, but which are probably associated to other radiants. At the time of the second peak, there is essentially no activity from other radiants in the area defined by Valdeitor, which allowed the detection of the radiant in visual data. It is important to notice that for several months of the year, this region of the sky was only visible during the day, therefore no meteors were captured during this period.

Despite the high activity of other meteors not belonging to the radiant, these meteors are distant from NEC in terms of their orbits. This becomes clear when we compare the numbers from the breakpoint+ and Valdeitor plots. In the breakpoint plot, the maximum number of meteors reached by NEC is about 475. Even if we increase the D value up to 0.8, the number of meteors does not increase significantly after $D = 0.2$. But when we look at the Valdeitor plot, it becomes evident that in the 20° radius area used to create the plots (breakpoint+ and Valdeitor) there were many other meteors besides these roughly 475 (the total number of meteors was 5783).

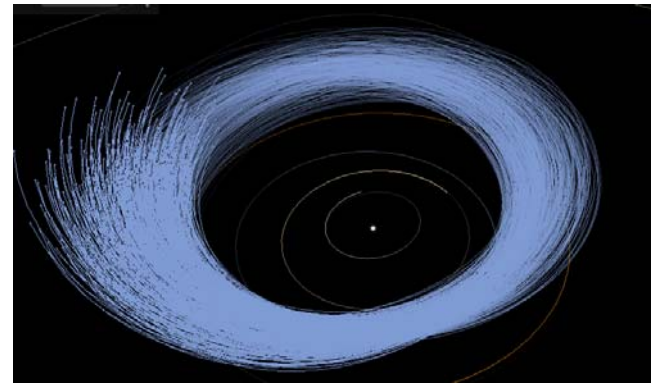


Figure 5 – Stream representation of the NEC ($D \leq 0.1$).

Figure 5 is a simple stream representation of the meteoroids associated to the NEC radiant. The purpose of the figure is just to demonstrate the orbital similarity of the meteoroids which are considered to belong to the radiant. This representation was created by exporting the orbital data of 549 NEC meteors (with $D \leq 0.1$) to the Universe Sandbox (2018) software.

A search for parent bodies of the NEC radiant has returned several possible candidates. The four candidates with the most compatible orbits are 2016BE₁, 2014DS₂₂, 2007TW₂₄, and 2014UA₈. Of these, 2016BE₁ is the object with the highest orbital similarity ($D = 0.019$).

A second concentration of NEC meteors (Table 2) that appears to be related to this radiant was also found. This second stream appears to be slightly larger than the first one found. The two groups vary mainly in terms of the parameters ω and Ω . This second stream was found using the BRAMON, SonotaCo, and EDMOND databases, and may indicate that the radiant can be associated to more than one parent body.

Table 2 – Second NEC flow (established from 262 orbits).

$\Delta\alpha$	$\Delta\delta$	λ_{\odot}	α	δ	V_G
0°48	0°07	219°8	13°83	−2°96	11.92 km/s
a	q	e	ω	Ω	i
2.38 au	0.62 au	0.89	40°45	39°8	4°51

3.2 JCT – July Cetids

Figure 6 shows a plot of the JCT Radiant orbit distribution. The radiant coverage area (right ascension from $\approx 340^\circ$ to $\approx 50^\circ$ and declination from $\approx -30^\circ$ to $\approx +20^\circ$) is noteworthy, in addition to an apparent speed increase as the right ascension decreases and the declination increases.

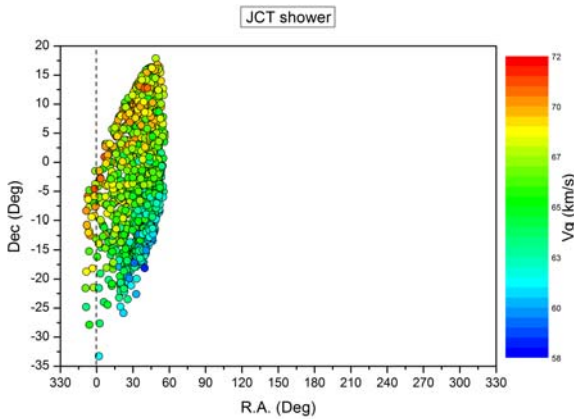


Figure 6 – Radiant of the July Cetids (JCT).

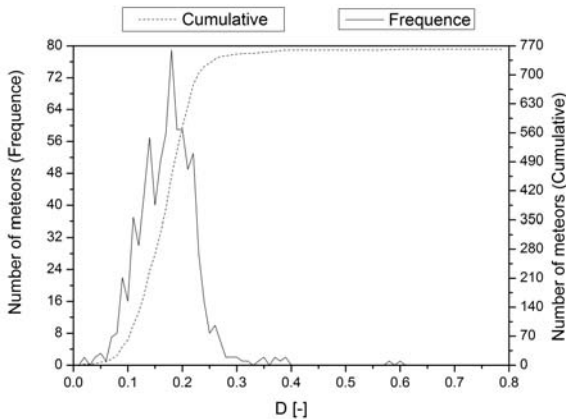


Figure 7 – JCT Break-point+ with a 20 degree radius.

Figure 7 shows the JCT breakpoint+ plot, in which we can see that the plot's inflection point occurs very early, close to $D = 0.22$, i.e., despite being a radiant with few orbits recorded by now, they are well concentrated relative to the radiant's mean orbit.

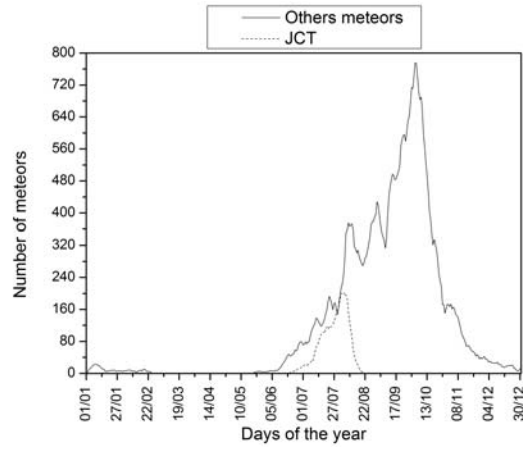


Figure 8 – JCT Valdeitor, 20° radius ($D \leq 0.22$).

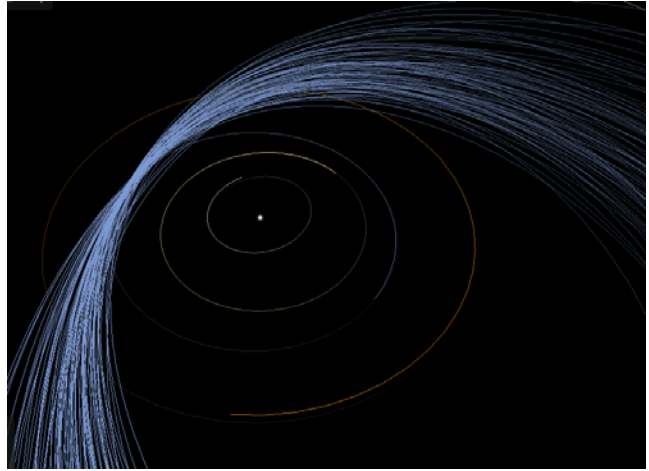


Figure 9 – Stream representation of the JCT ($D \leq 0.1$).

Figure 8 presents the Valdeitor plot (Amaral et al., 2018b), in which we can identify the formation of a maximum-activity peak in the radiant near the end of July and beginning of August. As detailed for the NEC radiant, we can also see the activity of other radiants along with the JCT radiant, however, according to the breakpoint+ plot, these radiants are orbitally distant from the JCT radiant.

Figure 9 is a stream representation of meteors associated to the JCT radiant. This representation was created by exporting the orbital data of 89 meteors belonging to JCT (with $D \leq 0.1$).

3.3 JCD – June Cetids

Figure 10 shows a plot of the JCD radiant orbit distribution, in which we can see the radiant coverage area (right ascension from $\approx 340^\circ$ to $\approx 50^\circ$ and declination from $\approx -35^\circ$ to $\approx -2.5^\circ$). Further, we find an apparent speed increase as the right ascension decreases and the declination increases.

Figure 11 shows the breakpoint+ plot for the JCD. We can see that the plot's inflection point occurs close to $D = 0.22$, i.e., despite being a radiant with rather few orbits recorded, they are well concentrated relative to the radiant's mean orbit.

Figure 12 shows the Valdeitor plot, in which we can identify that activity from the radiant occurs between the end of June and the middle of August. We can

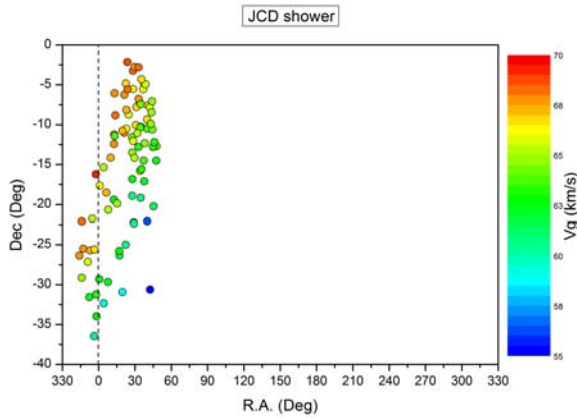


Figure 10 – Radiant of the June Cetids (JCD).

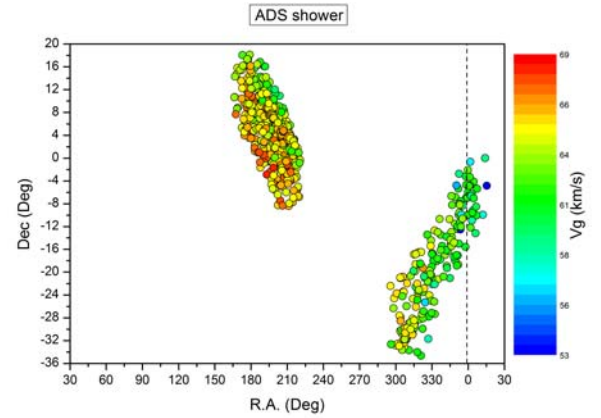


Figure 13 – Radiant of the June Aquariids (ADS).

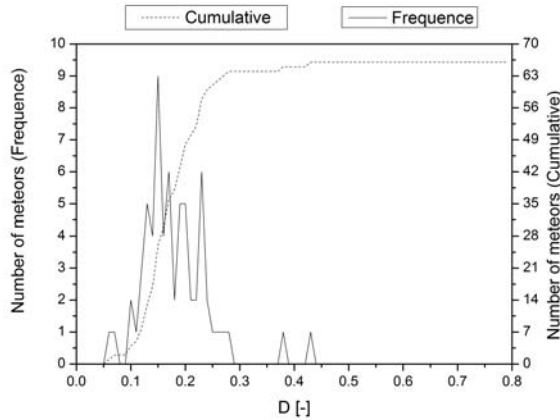


Figure 11 – JCD Break-point+ with a 20 degree radius.

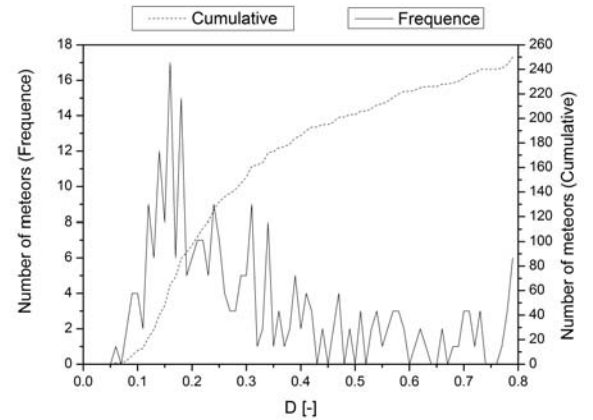
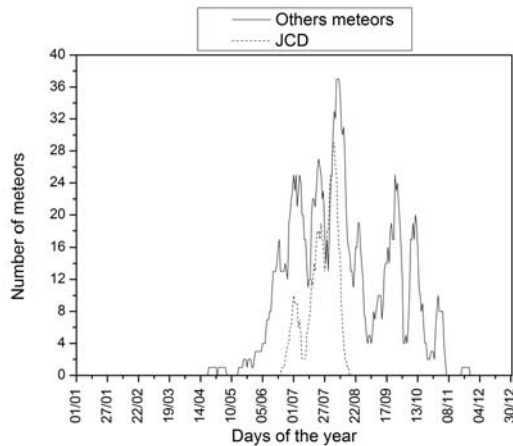
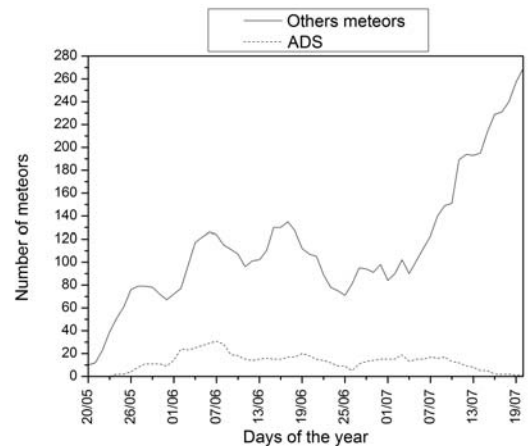


Figure 14 – ADS Break-point+ with a 20 degree radius.

Figure 12 – JCD Valdeitor, 20° radius ($D \leq 0.22$).Figure 15 – ADS Valdeitor, 20° radius ($D \leq 0.22$).

also notice the activity of other radiants along the JCD. As described for the NEC radiant, these other radiants appear to be orbitally distant to the JCD.

3.4 ADS – June Aquariids

Figure 13 shows a plot of the ADS radiant orbit distribution and the radiant coverage area (right ascension from $\approx 290^\circ$ to $\approx 15^\circ$ and declination from $\approx -34^\circ$ to $\approx 0^\circ$). We note that two regions of meteor occurrence are formed. This is because the radiant's orbit crosses the Earth's orbit at two different times, thus generating two radiants. ADS gives rise to the orbit concentration seen to the right, and another radiant (which appears to

be 428 DSV – December sigma Virginids) gives rise to the orbit concentration seen to the left. These two radiants may be related and may share a common parent body. We can also note that the speed of the meteors seems to increase as the right ascension decreases and the declination increases.

Figure 14 shows the ADS breakpoint+ plot, and although it starts to “decelerate” around $D = 0.3$, it is not clear where the inflection point is. This means that the orbits are not as strongly concentrated near the mean orbit associated with the radiant. While the mean orbit represents the point of highest concentration of orbits, the orbits associated to the radiant are not all close to

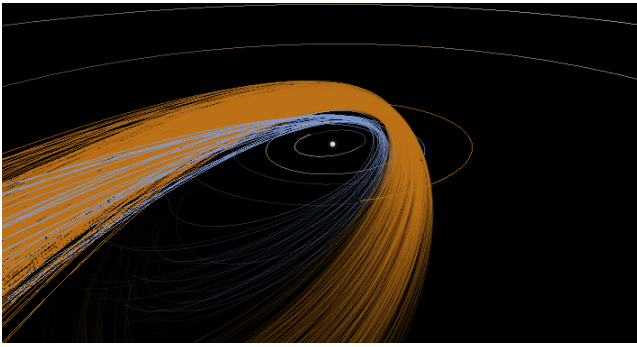


Figure 16 – Stream representation of the ADS and DSV ($D \leq 0.1$).

this center (as we saw in the case of NEC, JCT, and JCD). This could indicate, for example, that this is a radiant with meteoroid orbits which are already “dissipating” (perhaps due to minor orbital changes taking place over time), or even that the ADS could have been formed by several parent bodies with similar orbits.

Figure 15 shows the Valdeitor plot, in which we can identify the radiant’s activity between the end of May and the middle of July. We can also notice a strong activity of other radiants together with the ADS radiant.

Figure 16 is a stream representation of the meteors of the ADS (in blue) and the DSV (in orange). This representation was created by exporting the orbital data of 28 meteors belonging to the ADS (with $D \leq 0.1$) and 546 from the DSV.

3.5 LSA – Lambda Sagitariids

Figure 17 shows a plot of the JCD radiant orbit distribution, in which we can see the radiant coverage area (right ascension from $\approx 235^\circ$ to $\approx 320^\circ$ and declination from $\approx -34^\circ$ to $\approx -14^\circ$), in addition to an apparent speed increase as the right ascension decreases.

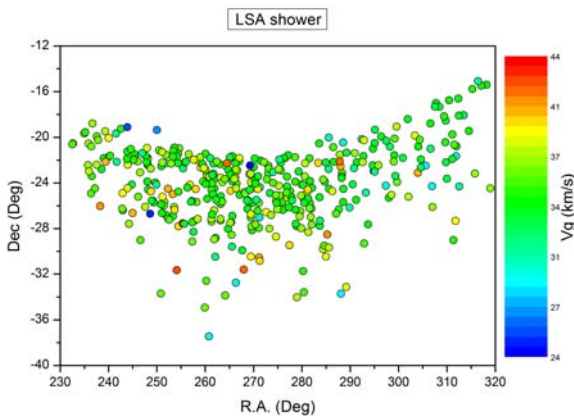


Figure 17 – Radiant of the Lambda Sagitariids (LSA).

Figure 18 shows the LSA breakpoint+ plot, in which the inflection point is late, i.e., the orbits are not strongly concentrated near the radiant’s mean orbit.

Figure 19 shows the Valdeitor plot, in which we can identify the radiant’s peak activity between the middle of May and beginning of June. We can also notice the activity of other radiants along with the LSA radiant. A relationship between the LSA and nearby radiants

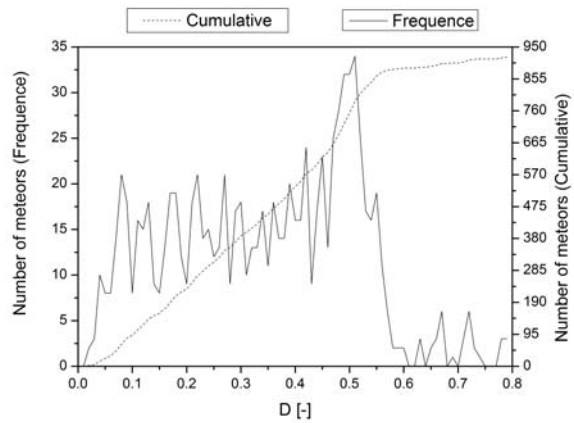


Figure 18 – LSA Break-point+ with a 20 degree radius.

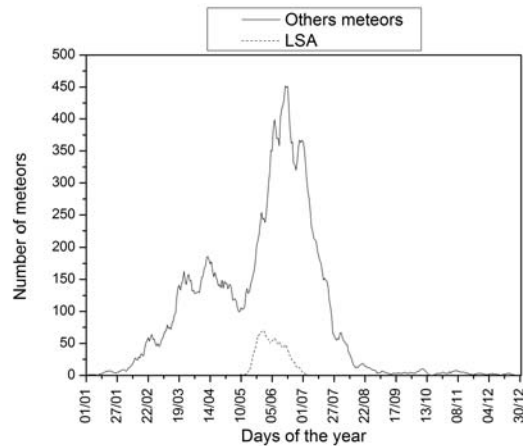


Figure 19 – LSA Valdeitor, 20° radius ($D \leq 0.22$).

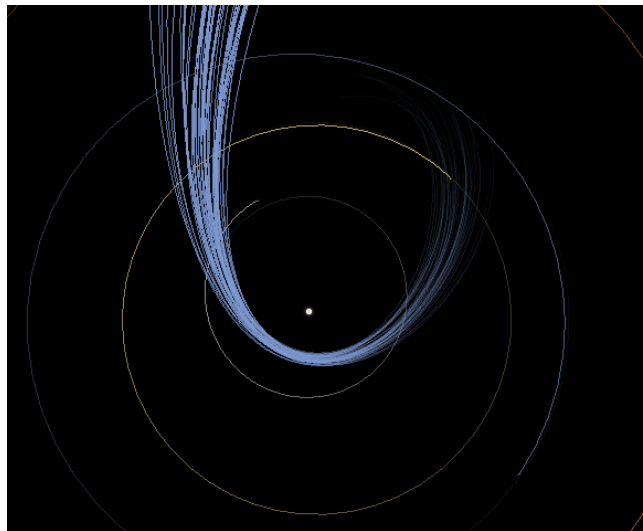


Figure 20 – Stream representation of the LSA ($D \leq 0.07$).

is likely, even though the LSA center is far from other radiants.

Figure 20 is a stream representation of the LSA radiant meteors. This representation was created by exporting the orbital data of 52 meteor belonging to LSA (with $D \leq 0.07$).

3.6 DGR – Delta2 Gruids

Figure 21 shows the orbit distribution of the DGR radiant, and we find the radiant coverage area in right

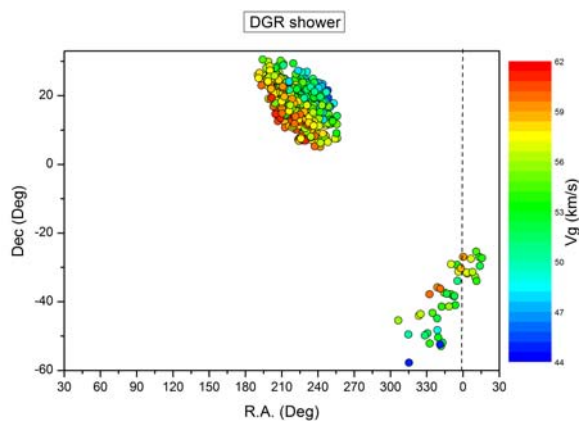


Figure 21 – Radiant of the Delta2 Gruids (DGR).

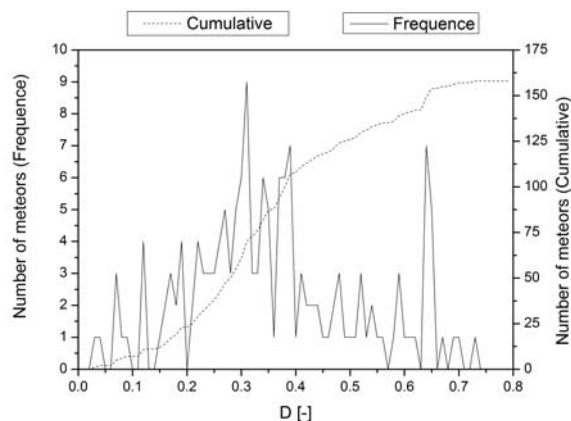


Figure 22 – DGR Break-point+ with a 20 degree radius.

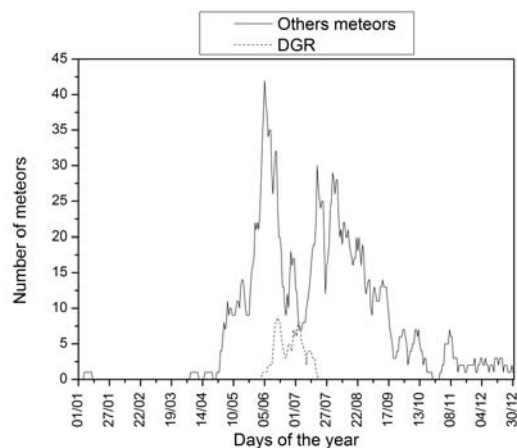


Figure 23 – DGR Valideitor, 20° radius ($D \leq 0.22$).

ascension from $\approx 315^\circ$ to $\approx 15^\circ$ and in declination from $\approx -55^\circ$ to $\approx -22^\circ$. DGR has a twin radiant, while DGR gives rise to the concentration of orbits on the right, another radiant (which appears to be 727 ISR – iota Serpentids) gives rise to the concentration of orbits on the left. These two radiants may be related and share a parent body. We can also notice that the speed of the meteors seems to increase as the right ascension and the declination increases.

Figure 22 shows the DGR breakpoint+ plot, and although it begins to “decelerate” near $D = 0.35$, it is not clear where the inflection point is, i.e., the orbits

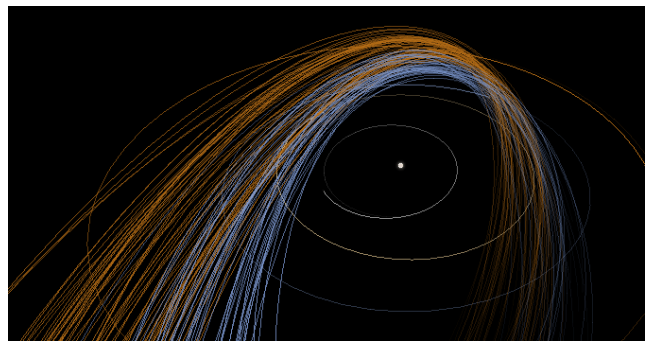


Figure 24 – Stream representation of the DGR and DSV ($D \leq 0.1$).

are not strongly concentrated near the radiant’s mean orbit.

Figure 23 shows the Valideitor plot, in which we can identify the radiant’s activity occurring between the beginning of June and the middle of July. We can also notice the activity of other radiants occurring together with the DGR radiant. A relationship between the DGR and nearby radiants is possible, even though the DGR center is far from other radiants.

Figure 24 is a stream representation of the DGR (in blue) and ISR (in orange) radiant meteors. This representation was created by exporting the orbital data of 51 meteor belonging to DGR (with $D \leq 0.1$) and 66 from ISR.

3.7 GSC – Gamma Sculptorids

Figure 25 shows the orbit distribution of the GSC radiant, and we can notice the radiant coverage area (right ascension from $\approx 315^\circ$ to $\approx 30^\circ$ and declination from $\approx -45^\circ$ to $\approx -2.5^\circ$). GSC gives rise to orbit concentration on the right, and its twin radiant (not yet published) gives rise to the orbit concentration on the left. These two radiants may be related and share a common parent body. We can also notice that the speed of the meteors seems to increase as the right ascension decreases and the declination increases.

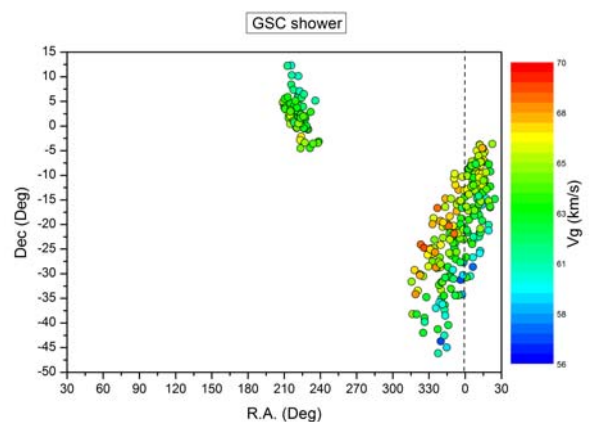


Figure 25 – Radiant of the Gamma Sculptorids (GSC).

Figure 26 presents the GSC breakpoint+ plot, whose inflection point is close to $D = 0.27$.

Figure 27 shows the Valideitor plot, in which we can identify the radiant’s activity near the end of May

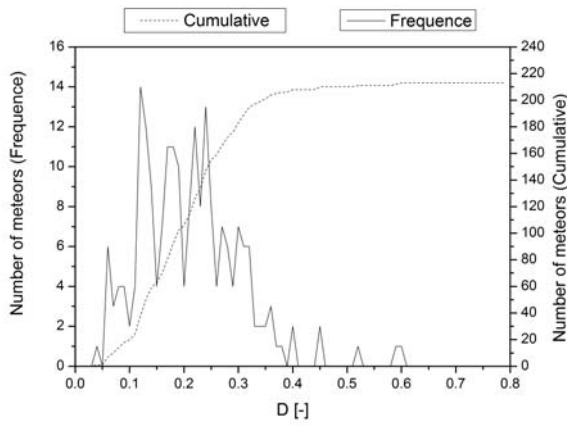


Figure 26 – GSC Breakpoint+ plot with a 20 degree radius.

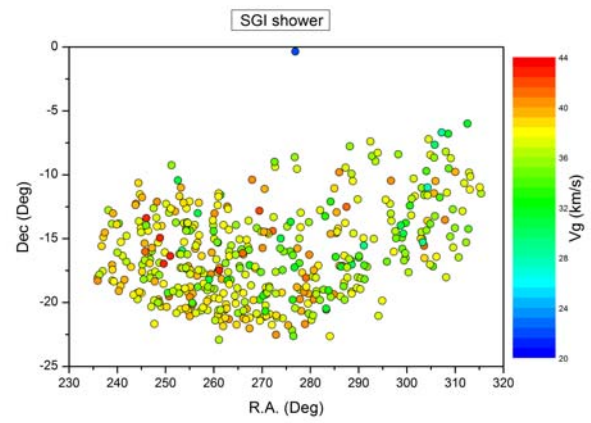


Figure 29 – Radiant of the June Sagittariids (SGI).

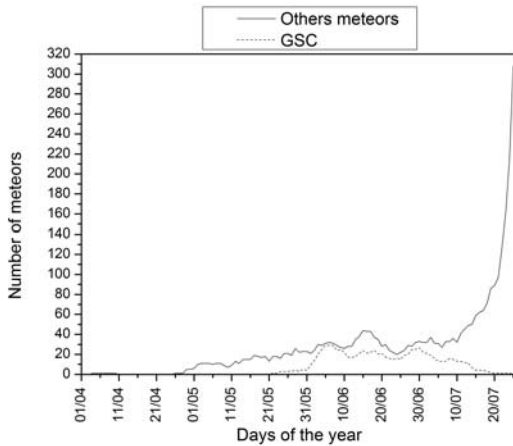
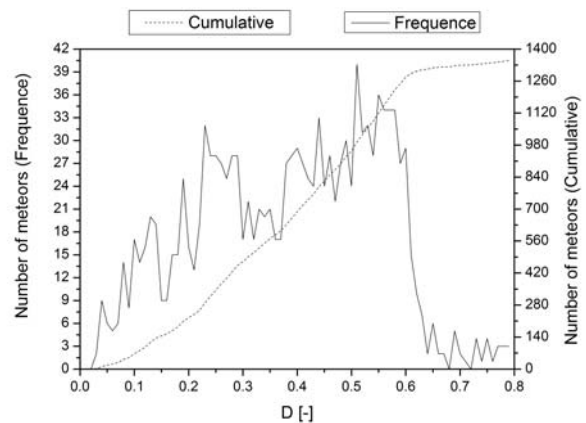
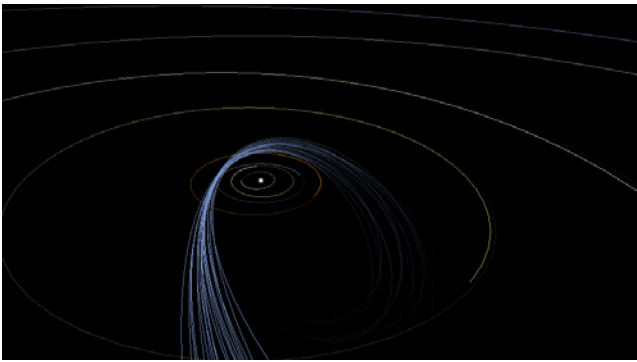
Figure 27 – GSC Valdeitor, 20° radius ($D \leq 0.22$).

Figure 30 – SGI Breakpoint+ plot with a 20 degree radius.

Figure 28 – Stream representation of the GSC ($D \leq 0.1$).

and end of July. We can also notice the activity of other radiants occurring together with the GSC radiant (with a large peak occurring at the end of July).

Figure 28 is a stream representation of the meteors classified as GSC. This representation was created by exporting the orbital data of 20 meteors belonging to the GSC (with $D \leq 0.1$).

3.8 SGI – June Sagittariids

Figure 29 shows the orbit distribution of the DGR radiant, and we can notice the radiant coverage area (right ascension from $\approx 235^\circ$ to $\approx 315^\circ$ and declination from $\approx -22^\circ$ to $\approx -7^\circ$). We can also notice that the speed of the meteors seems to increase as the right ascension decreases and the declination increases.

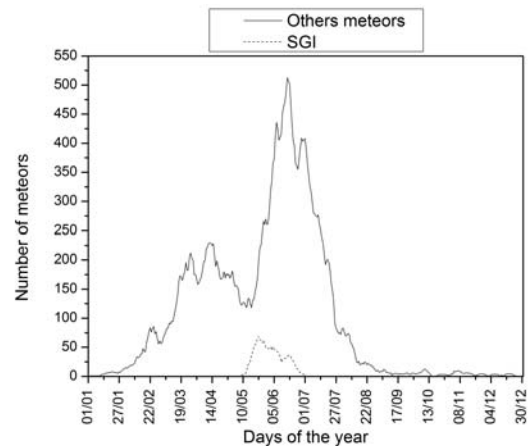
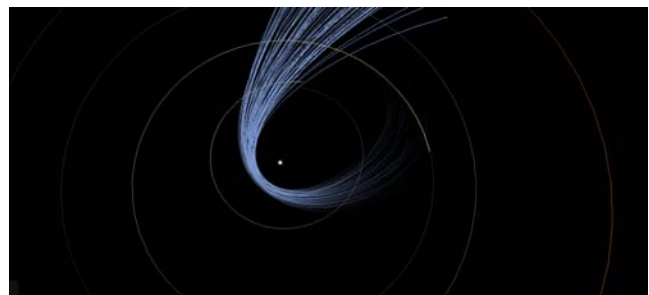
Figure 31 – SGI Valdeitor, 20° radius ($D \leq 0.22$).Figure 32 – Stream representation of the SGI ($D \leq 0.1$).

Figure 30 presents the SGI breakpoint+ plot, whose inflection point occurs late, close to $D = 0.6$, i.e., the

radiant's orbits are not concentrated in relation to the radiant's mean orbit.

Figure 31 shows the Valdeitor plot, in which we can identify the radiant's activity occurring between the middle of May and the beginning of July. We can also notice the activity of other radiants along the SGI radiant. A relationship between the SGI and nearby radiants is likely, even though the SGI center is far from other radiants.

Figure 32 is a stream representation of the SGI radiant meteors. This representation was created by exporting the orbital data of 79 meteor belonging to the SGI (with $D \leq 0.1$).

3.9 FLO – February Leonids

Figure 33 shows the orbit distribution of the FLO radiant, and we can notice the radiant coverage area (right ascension from $\approx 130^\circ$ to $\approx 205^\circ$ and declination from $\approx -17^\circ$ to $\approx +18^\circ$). We can also notice that the speed of the meteors seems to increase as the right ascension decreases and the declination increases.

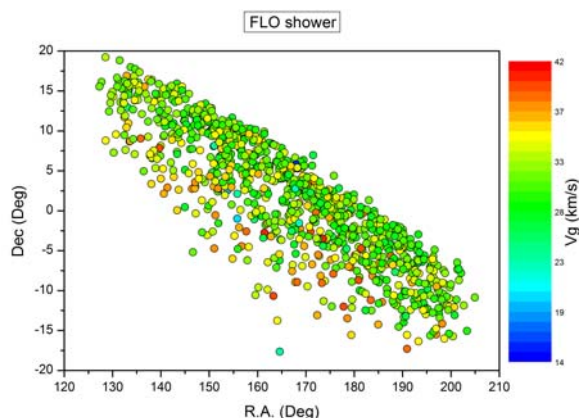


Figure 33 – Radiant of the February Leonids (FLO).

Figure 34 shows the FLO breakpoint+ plot, whose inflection point occurs late, close to $D = 0.4$, i.e., the radiant's orbits are weakly concentrated in relation to the radiant's mean orbit.

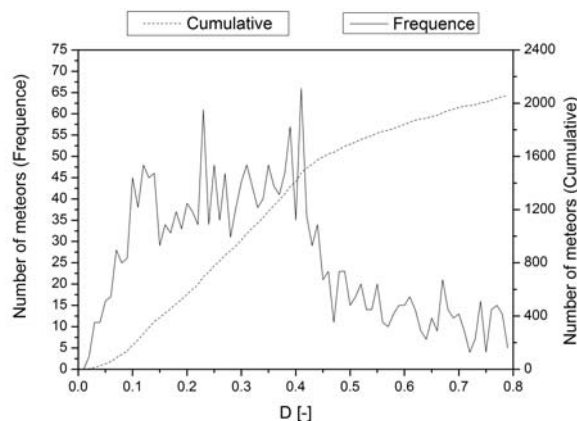


Figure 34 – FLO Breakpoint+ plot with a 20 degree radius.

Figure 35 shows the Valdeitor plot, in which we can identify the formation of three maximum activity peaks

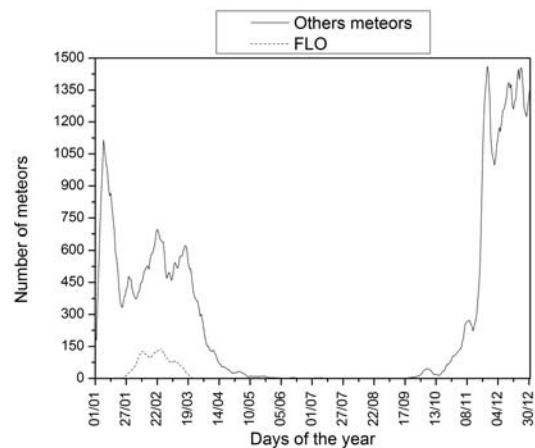


Figure 35 – FLO Valdeitor, 20° radius ($D \leq 0.22$).

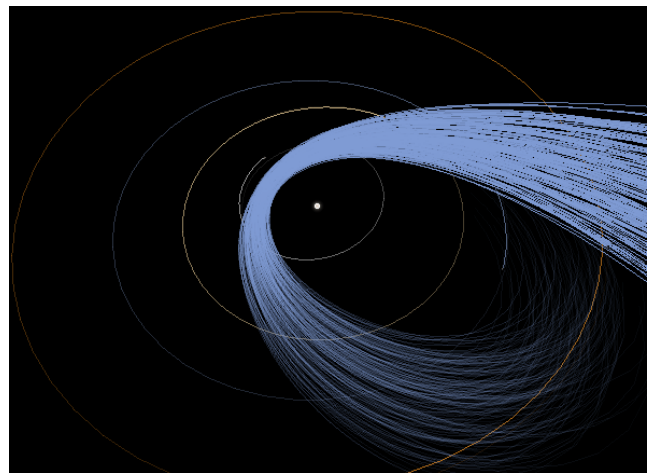


Figure 36 – Stream representation of the FLO ($D \leq 0.1$).

in the radiant between the middle of July and August, and also the activity of other radiants along with the FLO radiant. The FLO is likely related with nearby radiants.

Figure 36 is a streams representation of the FLO radiant meteors. This representation was created by exporting the orbital data of 207 meteors belonging to FLO (with $D \leq 0.1$).

3.10 PCS – Phi Capricornids

Figure 37 shows the orbit distribution of the PCS radiant, and we can notice the radiant coverage area (right ascension from $\approx 270^\circ$ to $\approx 30^\circ$ and declination from $\approx -45^\circ$ to $\approx +5^\circ$). We can also notice that the speed of the meteors seems to increase as the right ascension decreases and the declination increases.

Figure 38 shows the PCS breakpoint+ plot, whose inflection point occurs early, close to $D = 0.2$, i.e., despite being a radiant with few orbits recorded, they are concentrated relative to the mean orbit associated with the radiant.

Figure 39 shows the Valdeitor plot, in which we can identify the radiant's activity between the beginning of November and the middle of December. Some of these peaks show a higher occurrence of meteors among radiants that occur in the same period. We can also notice the activity of other radiants along the PCS radiant,

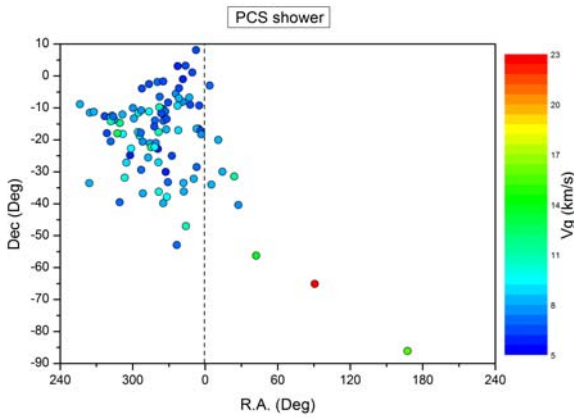


Figure 37 – Radiant of the Phi Capricornids (PCS).

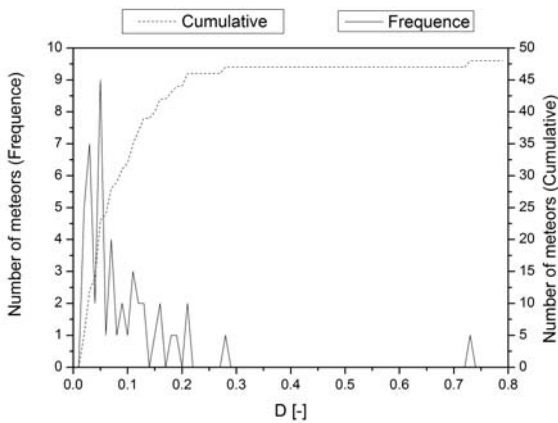


Figure 38 – PCS Breakpoint+ plot with a 20 degree radius.

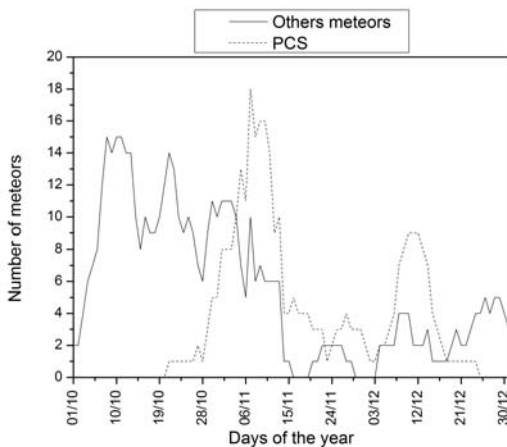


Figure 39 – PCS Valdeitor, 20° radius ($D \leq 0.22$).

and that, as detailed in the NEC radiant, these other radiants seem to be orbitally distant from the PCS.

Figure 40 is a stream representation of the PCS radiant meteors. This representation was created by exporting the orbital data of 71 meteor belonging to PCS (with $D \leq 0.1$).

A search for parent bodies of the PCS radiant has returned several possible candidates. The four candidates with the most similar orbits the asteroids 2009 WX₇, 2010 VW₁₉₄, 2014 WX₄, and 2015 XM₁₆₉, respectively. 2009 WX₇ is the potential parent body with the highest orbital similarity ($D = 0.0135$).

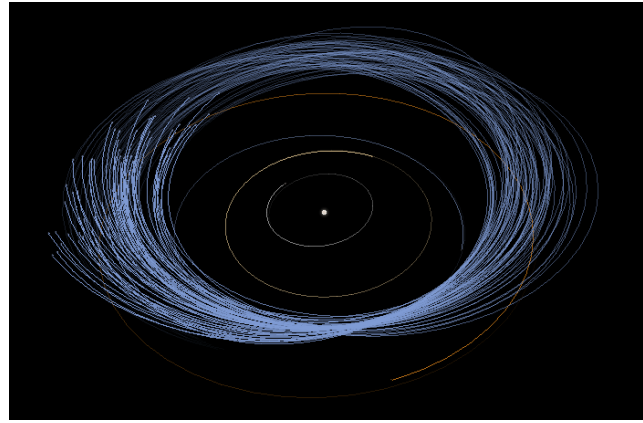


Figure 40 – Stream representation of the PCS ($D \leq 0.1$).

3.11 USG – Phi Ophiuchids

Figure 41 shows the orbit distribution of the USG radiant, and we can notice the radiant coverage area (right ascension from $\approx 210^\circ$ to $\approx 290^\circ$ and declination from $\approx -22^\circ$ to $\approx -2^\circ 5$). We can also notice that the speed of the meteors seems to increase as the right ascension decreases and the declination increases.

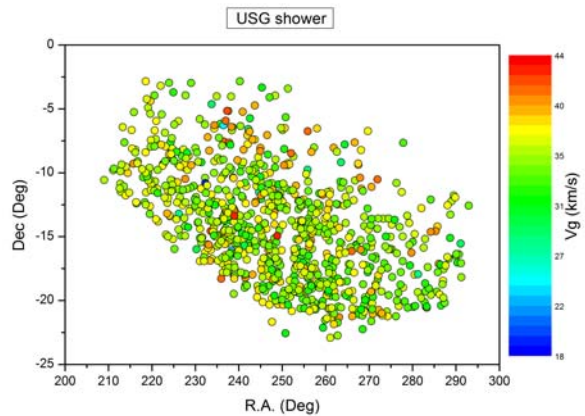


Figure 41 – Radiant of the Phi Ophiuchids (USG).

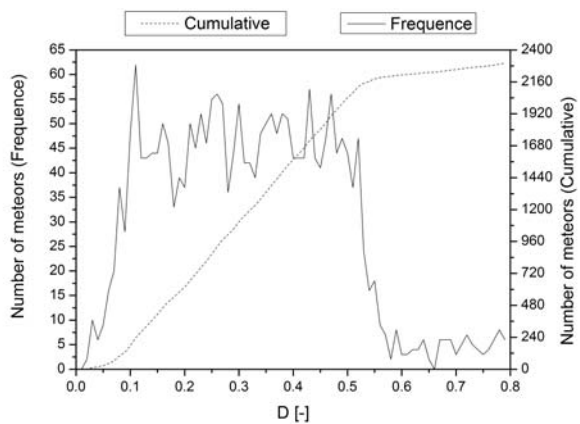


Figure 42 – USG Breakpoint+ plot with a 20 degree radius.

Figure 42 shows the USG breakpoint+ plot, whose inflection point occurs late, near $D = 0.5$, i.e., the orbits associated to the radiant are not concentrated relative to the radiant's mean orbit.

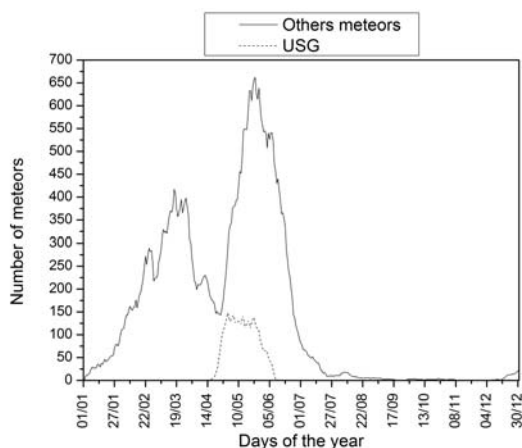


Figure 43 – USG Valdeitor, 20° radius ($D \leq 0.22$).

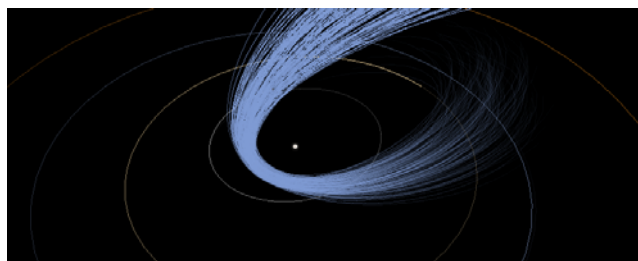


Figure 44 – Stream representation of the USG ($D \leq 0.1$).

Figure 43 presents the Valdeitor plot, which shows radiant activity between April and June. We can also notice the activity of other radiants along with the USG radiant, and it is likely that there is a relationship between USG and other nearby radiants.

Figure 44 is a stream representation of the USG radiant meteors. This representation was created by exporting the orbital data of 195 meteors belonging to USG (with $D \leq 0.1$).

3.12 XCD – October Cetids

Figure 45 shows the orbit distribution of the XCD radiant, and we can notice the radiant coverage area (right ascension from $\approx 30^\circ$ to $\approx 75^\circ$ and declination from $\approx +2.5^\circ$ to $\approx +22^\circ$). We can also notice that the speed of the meteors seems to increase as the right ascension decreases and the declination increases.

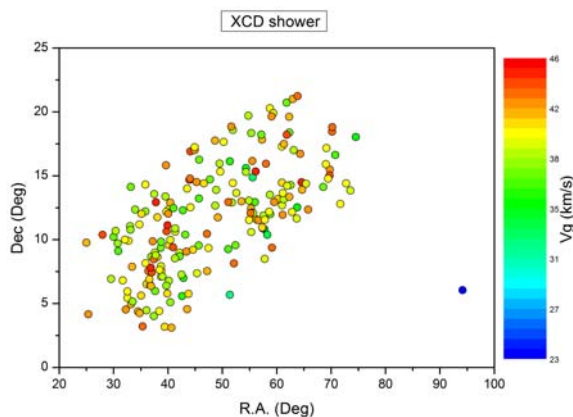


Figure 45 – Radiant of the October Cetids (XCD).

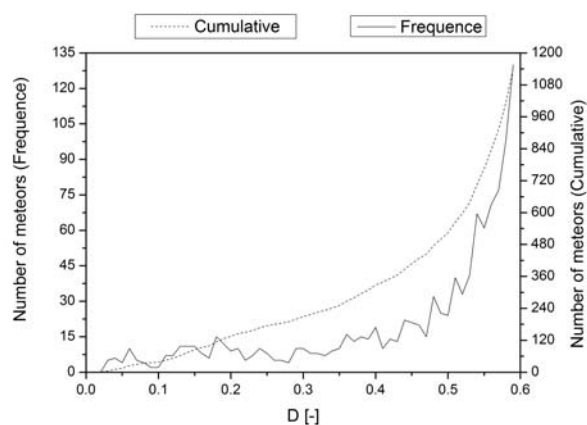


Figure 46 – XCD Breakpoint+ plot with a 20 degree radius.

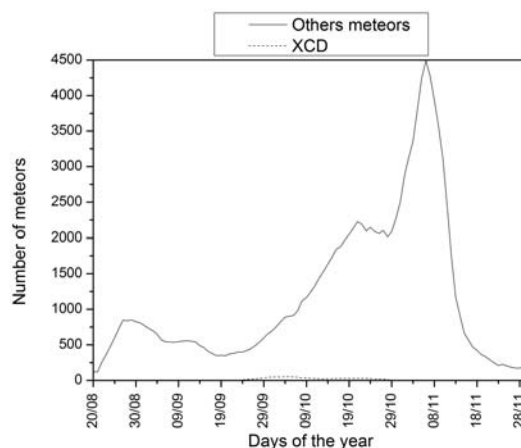


Figure 47 – XCD Valdeitor, 20° radius ($D \leq 0.22$).

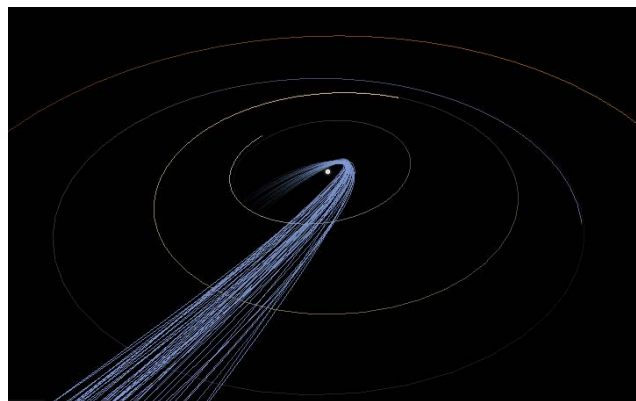


Figure 48 – Stream representation of the XCD ($D \leq 0.1$).

Figure 46 shows the XCD breakpoint+ plot, and we can observe two small inflection points on the plot (close to 0.07 and 0.25). We can also notice that after $D > 0.5$ the plot grows rapidly. This indicates that the XCD radiant became orbitally “close” at this point to a much larger radiant, which is clear when we look at the Valdeitor plot in Figure 47. In this plot, the radiant shows modest activity when compared to other radiants occurring at the same location, i.e., XCD is hard to detect (specially through visual methods) since it is a small radiant occurring at the location of activity of much larger radiants. The Breakpoint+ plot shows a relationship between XCD and other nearby radiants, however, it is important to notice that the orbits asso-

ciated with the XCD are distant from orbits of other known radiant.

Figure 48 is a stream representation of the XCD radiant meteors. This representation was created by exporting the orbital data of 46 meteors belonging to XCD (with $D \leq 0.1$).

3.13 LCP – Lambda Capricornids

Figure 49 shows the distribution of orbits associated with the LCP radiant. We find a radiant coverage area in right ascension from $\approx 300^\circ$ to $\approx 50^\circ$ and in declination from $\approx -50^\circ$ to $\approx +15^\circ$. We can also notice that the speed of the meteors seems to increase as the right ascension decreases and the declination increases.

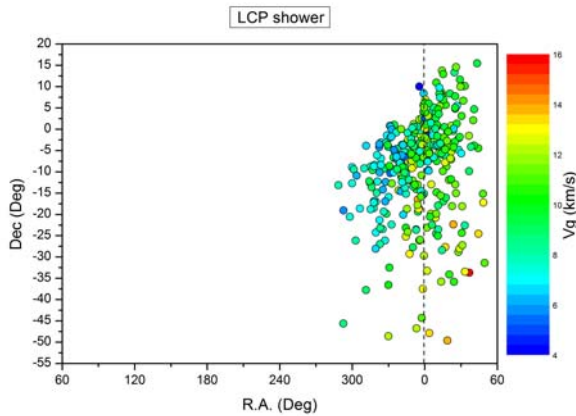


Figure 49 – Radiant of the Lambda Capricornids (LCP).

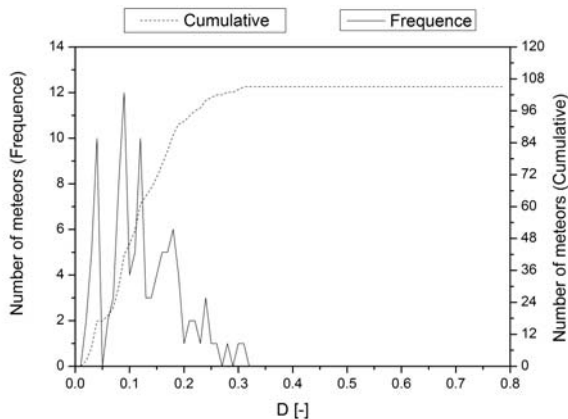


Figure 50 – LCP Breakpoint+ plot with a 20 degree radius.

Figure 50 shows the LCP breakpoint+ plot, whose inflection point occurs early, close to $D = 0.2$, i.e., despite being a radiant with very few orbits recorded, they are well concentrated relative to the mean orbit belonging to the radiant.

Figure 51 shows the Valdeitor plot, in which we can identify the radiant's activity between the end of September and the beginning of November. Some peaks show a higher occurrence of meteors among radiants being active in the same period. Additionally, we can notice the activity from other radiants occurring together with the LCP shower. Such radiants appear to be distant in terms of their orbits, just as explained in detail for the NEC radiant.

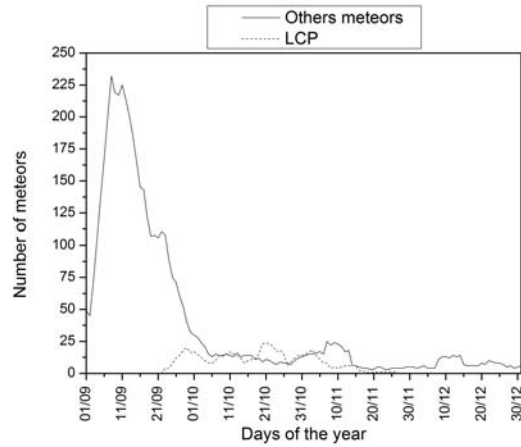


Figure 51 – LCP Valdeitor, 20° radius ($D \leq 0.22$).

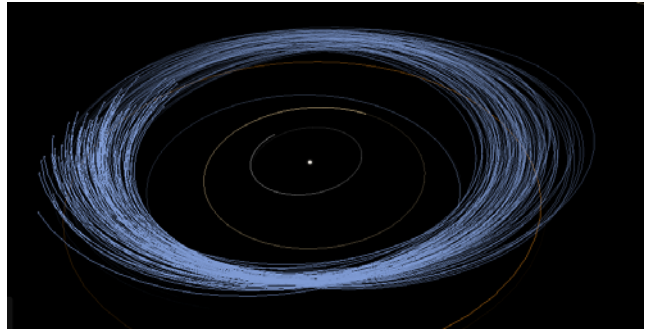


Figure 52 – Stream representation of the LCP ($D \leq 0.1$).

Figure 52 is a stream representation of the meteors related to the LCP radiant. This representation was created by exporting the orbital data of 96 meteors belonging to LCP (with $D \leq 0.1$).

A search for parent bodies of the LCP radiant has returned several possible candidates. The two candidates with the most similar orbits are 2014 RQ₁₇, and 2016 TD₁₁, and 2014 RQ₁₇ is the parent body with the highest orbital similarity ($D = 0.0257$).

3.14 NAA – November alpha Aurigids

Figure 53 shows the orbit distribution of the NAA radiant, and we can notice the radiant coverage area (right ascension from $\approx 40^\circ$ to $\approx 125^\circ$ and declination from $\approx +38^\circ$ to $\approx +54^\circ$). We can also notice that the

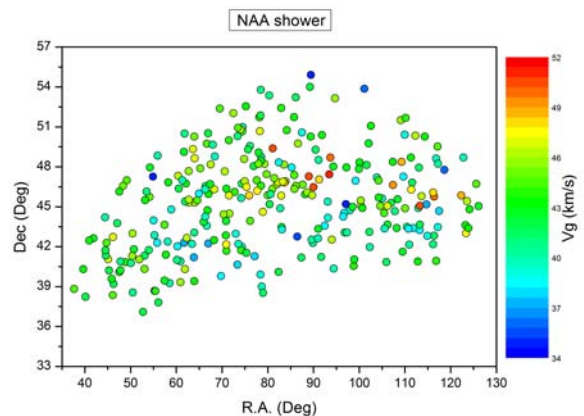


Figure 53 – Radiant of the November alpha Aurigids (NAA).

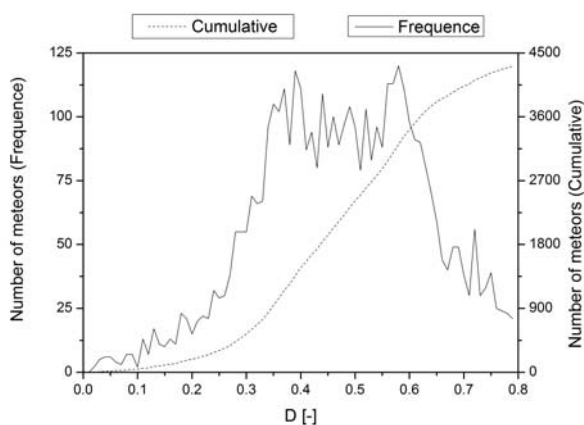


Figure 54 – NAA Breakpoint+ plot with a 20 degree radius.

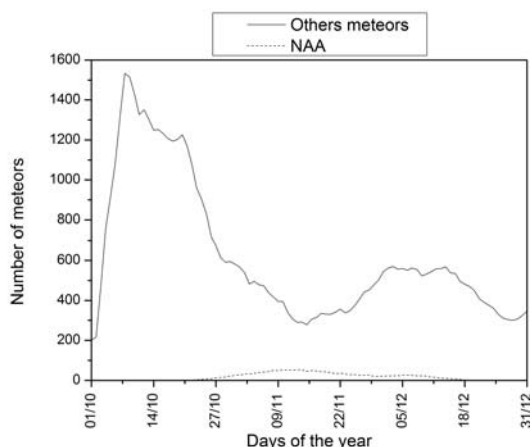


Figure 55 – NAA Valdeitor, 20° radius ($D \leq 0.22$).

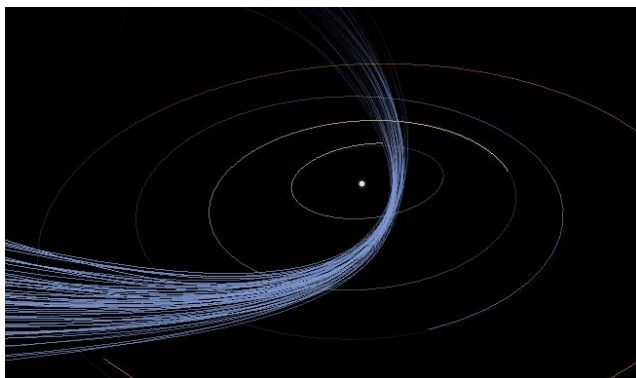


Figure 56 – Stream representation of the NAA ($D \leq 0.1$).

speed of the meteors seems to increase as the declination increases.

Figure 54 shows the NAA breakpoint+ plot, whose inflection point occurs late, close to $D = 0.6$, i.e., the radiant's orbits are not concentrated in relation to the radiant's mean orbit.

Figure 55 presents the Valdeitor plot, which shows the radiant activity occurring between October and December. We can also notice the strong activity of other radiants occurring together with the NAA radiant.

Figure 56 is a stream representation of the NAA radiant meteors. This representation was created by exporting the orbital data of 61 meteors belonging to the NAA (with $D \leq 0.1$).

3.15 OAC – October alpha Camelopardalids

Figure 57 shows the orbit distribution of the OAC radiant, in which we can see the radiant coverage area (right ascension from $\approx 340^\circ$ to $\approx 50^\circ$ and declination from $\approx -30^\circ$ to $\approx +20^\circ$). We can also notice that the speed of the meteors seems to increase as their right ascension decreases and the declination increases.

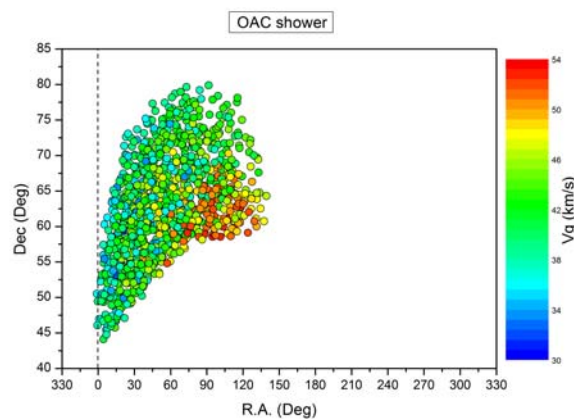


Figure 57 – Radiant of the October alpha Camelopardalids (OAC).

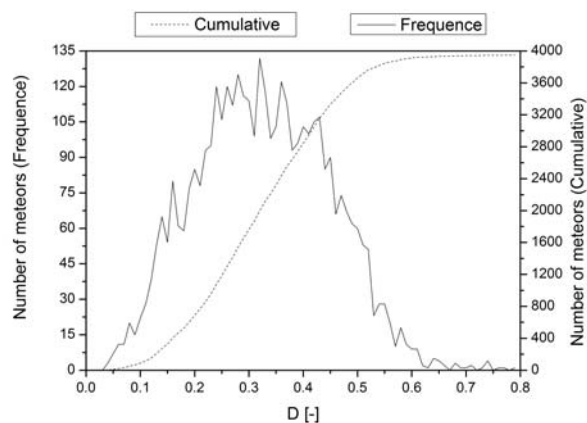


Figure 58 – OAC Breakpoint+ plot with a 20 degree radius.

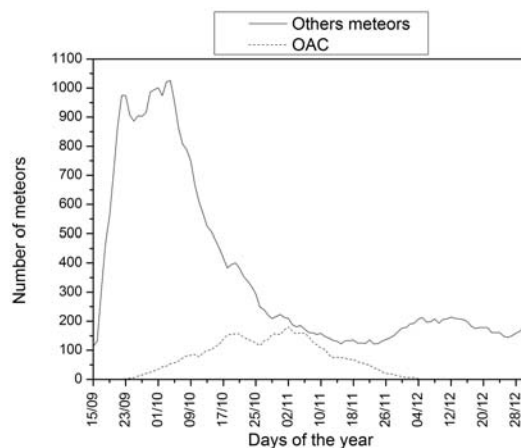


Figure 59 – OAC Valdeitor, 20° radius ($D \leq 0.22$).

Figure 58 shows the OAC breakpoint+ plot, whose inflection point occurs early, near $D = 0.5$, i.e., the

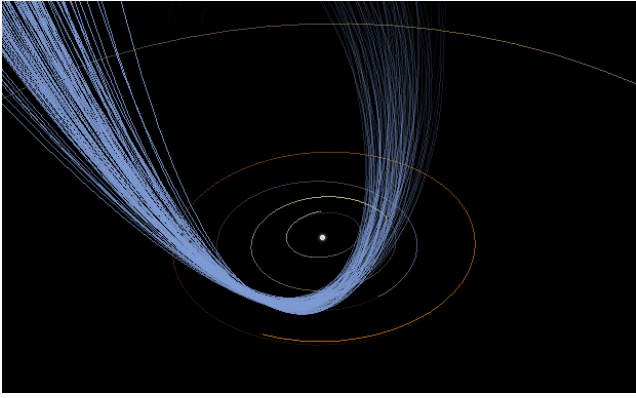


Figure 60 – Stream representation of the OAC ($D \leq 0.1$).

radiant's orbits are not concentrated relative to the radiant's mean orbit.

Figure 59 presents the Valdeitor plot, which shows that the radiant's activity occurs between September and December. We can also notice the activity of other radiants together with the OAC radiant. The OAC is likely related to nearby radiants.

Figure 60 is a stream's representation of the OAC radiant meteors. This representation was created by exporting the orbital data of 103 meteors belonging to OAC (with $D \leq 0.1$).

3.16 CVD – January Canum Venaticids

Figure 61 shows the orbit distribution of the CVD radiant. The radiant coverage extends over an area between $\approx 0^\circ$ and $\approx 140^\circ$ in right ascension and from $\approx +44^\circ$ to $\approx +80^\circ$ in declination. We can also notice that the speed of the meteors seems to increase as the right ascension decreases and the declination increases.

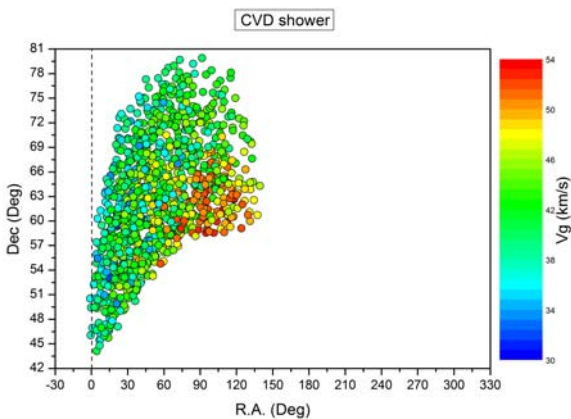


Figure 61 – Radiant of the January Canum Venaticids (CVD).

Figure 62 presents the CVD breakpoint+ plot, whose inflection point occurs late, close to $D = 0.5$. We can also notice that after $D > 0.4$ the plot grows rapidly, indicating that at this point the orbits of meteors associated to the CVD radiant were “close” to those of another radiant. This generated a rapid increase in the number of meteors in the plot at this position. This is evident when we look at the Valdeitor plot in Figure 63, in which the radiant's activity is accompanied by strong activity from other radiants occurring at the

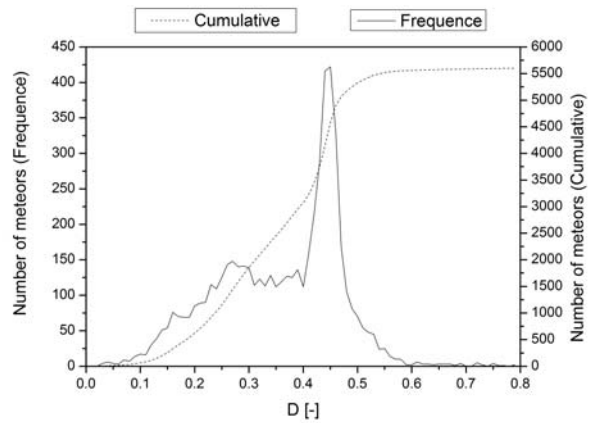


Figure 62 – CVD Breakpoint+ plot with a 20 degree radius.

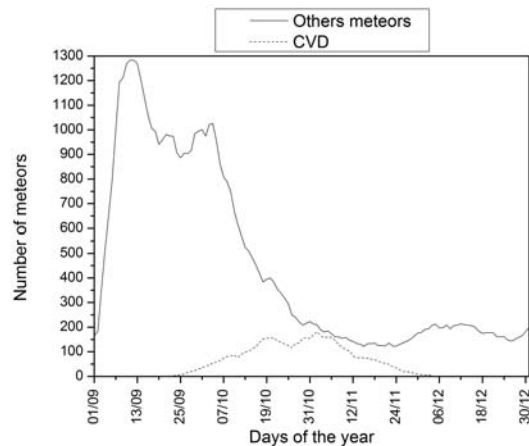


Figure 63 – CVD Valdeitor, 20° radius ($D \leq 0.22$).

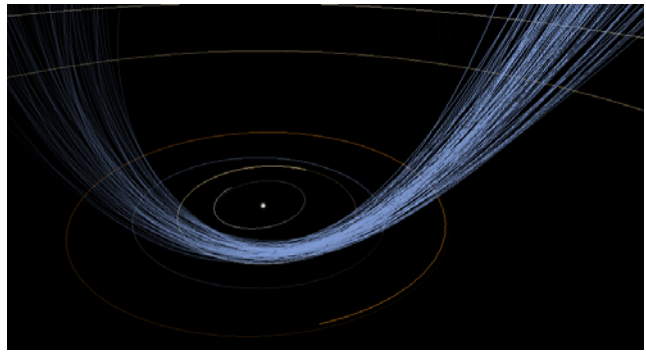


Figure 64 – Stream representation of the CVD ($D \leq 0.1$).

same position. Some of these radiants may be orbitally related with the CVD.

Figure 64 is a stream representation of the CVD radiant meteors. This representation was created by exporting the orbital data of 103 meteors belonging to CVD (with $D \leq 0.1$).

3.17 UMS – August Ursae Majorids

Figure 65 shows the orbit distribution of the UMS radiant, and we can notice the radiant coverage area (right ascension from $\approx 60^\circ$ to $\approx 210^\circ$ and declination from $\approx +45^\circ$ to $\approx +85^\circ$). We can notice that two regions of meteor occurrence are formed. UMS gives rise to the concentration of orbits with positive declination and another radiant (not yet published) gives rise to the concentration of orbits on the left, and these two radi-

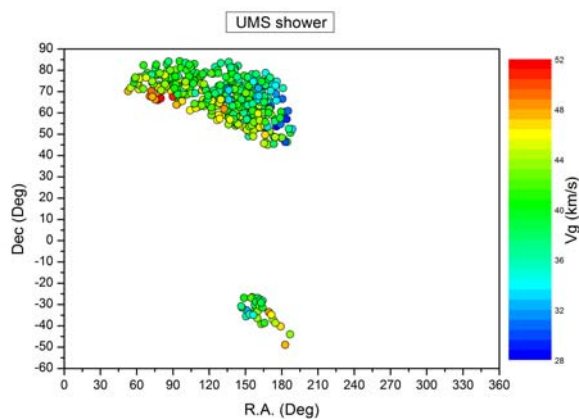


Figure 65 – Radiant of the August Ursae Majorids (UMS).

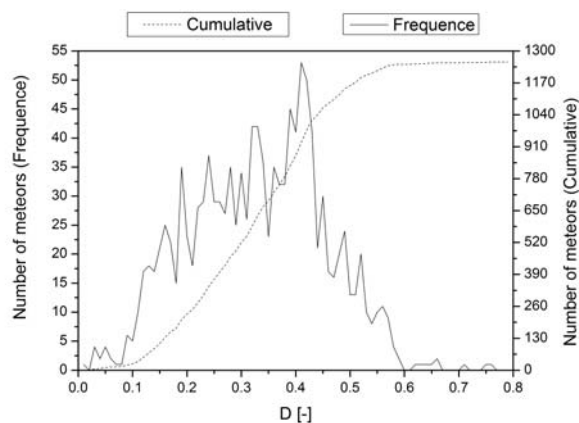
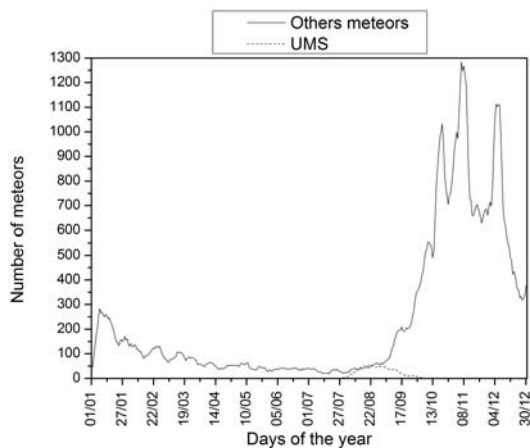


Figure 66 – UMS Breakpoint+ plot with a 20 degree radius.

Figure 67 – UMS Valdeitor, 20° radius ($D \leq 0.22$).

ant may be related and share a common parent body. We can also notice that the speed of the meteors seems to increase as the right ascension decreases and the declination increases.

Figure 66 shows the UMS breakpoint+ plot, whose inflection point occurs late, near $D = 0.55$, i.e., the radiant's orbits are not concentrated in relation to the radiant's mean orbit.

Figure 67 presents the Valdeitor plot, which shows that the radiant's activity occurs between September and December. We see activity from other radiants together with the UMS radiant. The UMS is likely related to nearby radiants.

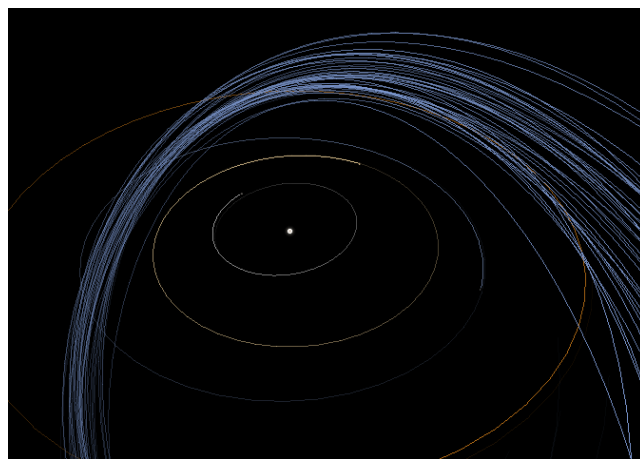
Figure 68 – Stream representation of the UMS ($D \leq 0.1$).

Figure 68 is a stream representation of the UMS radiant meteors. This representation was created by exporting the orbital data of 42 meteors belonging to UMS (with $D \leq 0.1$).

3.18 CVT – February Canum Venaticids

Figure 69 shows the orbit distribution of the CVT radiant, and we can notice the radiant coverage area (right ascension from $\approx 150^\circ$ to $\approx 230^\circ$ and declination from $\approx +22^\circ$ to $\approx +55^\circ$). We can also notice that the speed of the meteors seems to increase as the right ascension increases and the declination decreases.

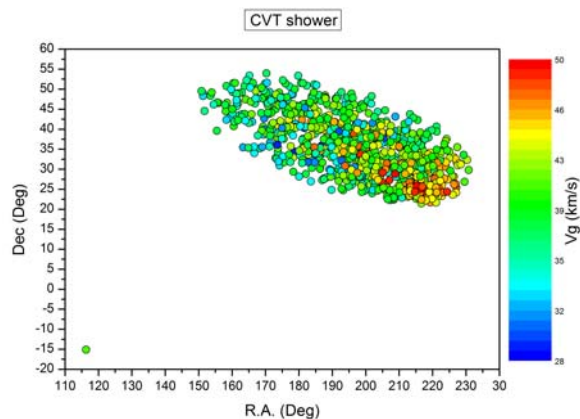


Figure 69 – Radiant of the February Canum Venaticids (CVT).

Figure 70 shows the CVT breakpoint+ plot, whose inflection point occurs late, near $D = 0.6$, i.e., the radiant's orbits are not concentrated in relation to the radiant's mean orbit.

Figure 71 presents the Valdeitor plot, which shows radiant activity between January and March. We can also notice the activity of other radiants occurring together with the CVT radiant. The CVT is likely related to nearby radiants.

Figure 72 is a stream representation of the CVT radiant meteors. This representation was created by exporting the orbital data of 125 meteors belonging to the CVT (with $D \leq 0.1$).

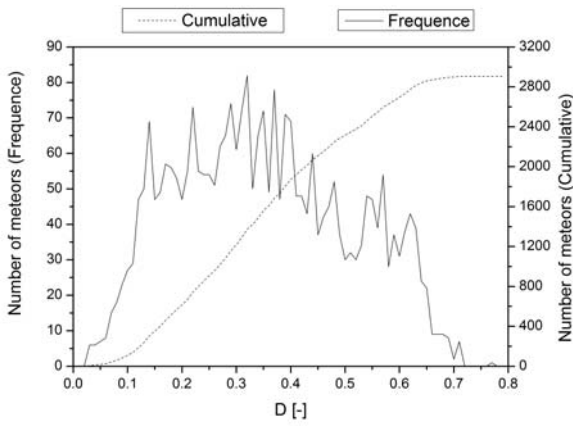


Figure 70 – CVT Breakpoint+ plot with a 20 degree radius.

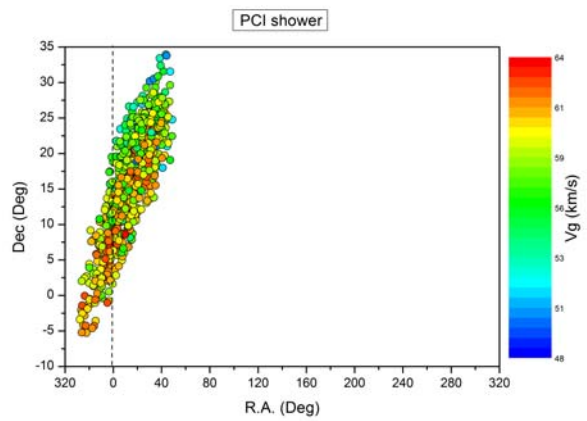


Figure 73 – Radiant of the 42 Piscids (PCI).

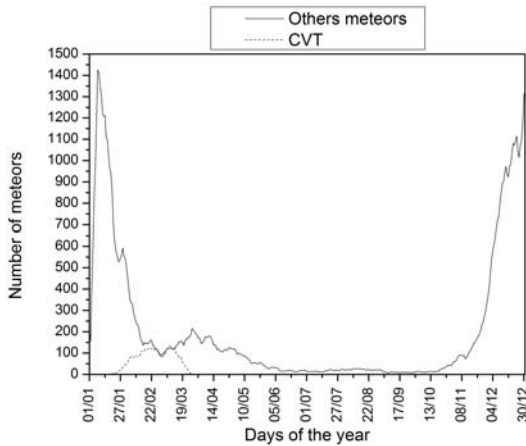
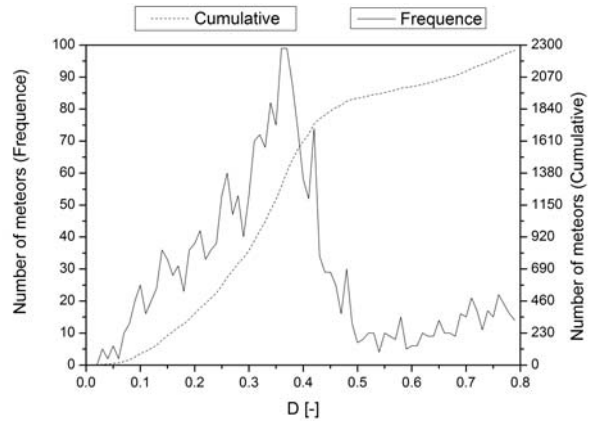
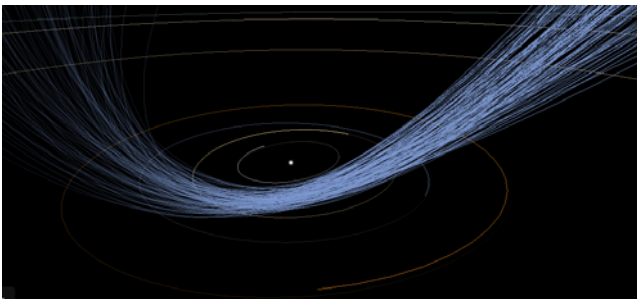
Figure 71 – CVT Valdeitor, 20° radius ($D \leq 0.22$).

Figure 74 – PCI Breakpoint+ plot with a 20 degree radius.

Figure 72 – Stream representation of the CVT ($D \leq 0.1$).

3.19 PCI – 42 Piscids

Figure 73 shows the orbit distribution of the PCI radiant. We can notice the radiant coverage area (right ascension from ≈ 330 to $\approx 60^\circ$ and declination from $\approx -5^\circ$ to $\approx +35^\circ$). We can also notice that the speed of the meteors seems to increase as the right ascension decreases and the declination increases.

Figure 74 shows the PCI breakpoint+ plot, whose inflection point occurs early, near $D = 0.4$, i.e., the radiant's orbits are weakly concentrated in relation to the radiant's mean orbit.

Figure 75 presents the Valdeitor plot. In the plot we can identify the activity of the radiant between July and September. We can also notice the activity of other radiants occurring together with the PCI radiant. PCI is likely to be related to these radiants.

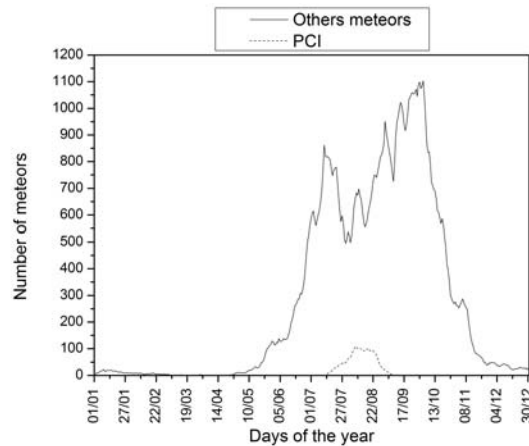
Figure 75 – PCI Valdeitor, 20° radius ($D \leq 0.22$).

Figure 76 is a stream representation of the meteors forming the PCI radiant. This representation was created by exporting the orbital data of 100 meteors belonging to the PCI (with $D \leq 0.1$).

3.20 OAG – October Aurigids

Figure 77 shows the orbit distribution of the OAG radiant. We can notice the radiant coverage area (right ascension from $\approx 30^\circ$ to $\approx 110^\circ$ and declination from $\approx +24^\circ$ to $\approx +43^\circ$). We can also notice that the speed of the meteors seems to increase as the right ascension decreases and the declination increases.

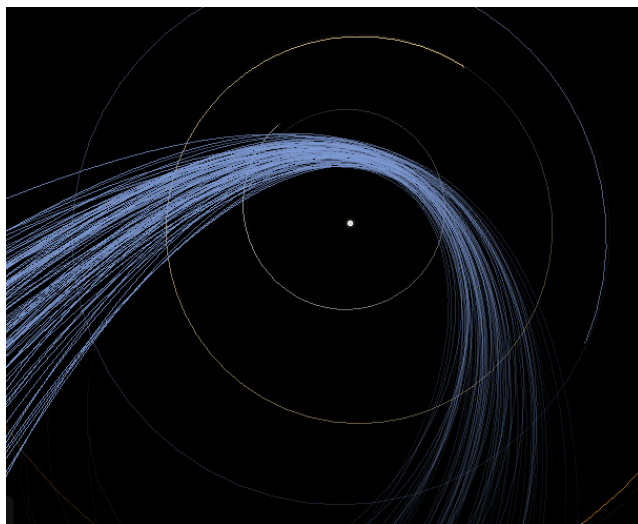
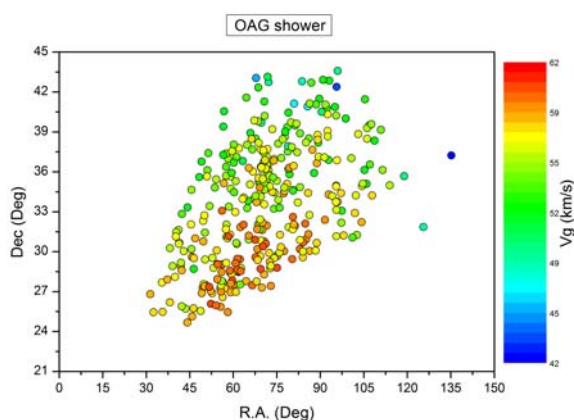
Figure 76 – Stream representation of the PCI ($D \leq 0.1$).

Figure 77 – Radiant of the October Aurigids (OAG).

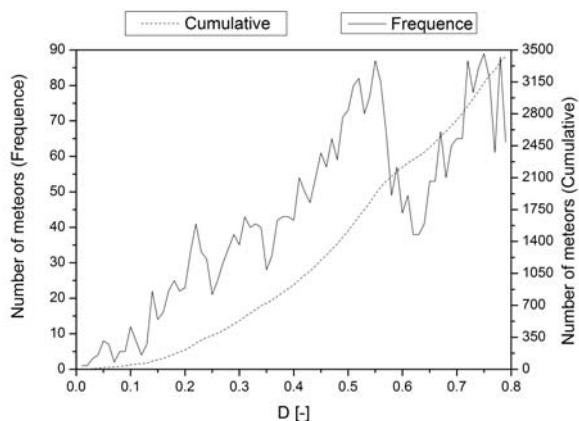
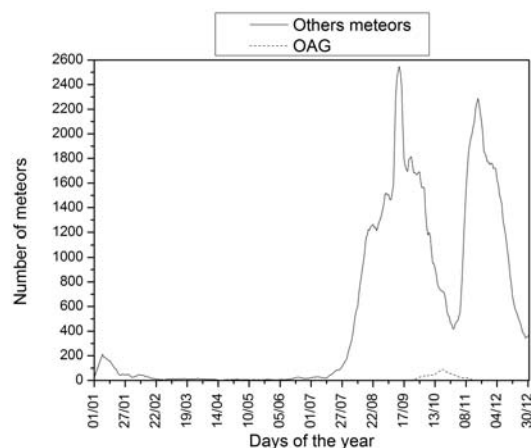
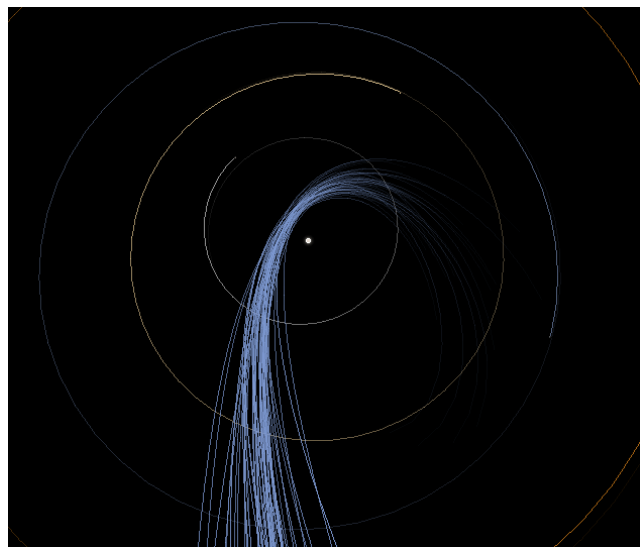


Figure 78 – OAG Breakpoint+ plot with a 20 degree radius.

Figure 78 shows the OAG breakpoint+ plot, whose inflection point occurs early, near $D = 0.55$, i.e., the radiant's orbits are not concentrated towards the radiant's mean orbit.

Figure 79 presents the Valdeitor plot. In the plot we can identify the formation of a maximum activity peak in the radiant near the end of October and beginning of November. We can also notice the activity of other radiants occurring together with the OAG radiant. The OAG is likely related to nearby radiants.

Figure 79 – OAG Valdeitor, 20° radius ($D \leq 0.22$).Figure 80 – Stream representation of the OAG ($D \leq 0.1$).

Between $\lambda_{\odot} = 191^{\circ}$ and 209° there are seven more showers with radiant in or near Auriga in the IAU data base. If we compare the orbital parameters of the radiants, we see that all of them show a dissimilarity $D > 0.1$ implying that they are quite distant.

Figure 80 is a stream representation of the OAG radiant meteors. This representation was created by exporting the orbital data of 56 meteors belonging to the OAG (with $D \leq 0.1$).

3.21 SPS – Sigma Perseids

Figure 81 shows the orbit distribution of the SPS radiant. We can notice the radiant coverage area (right ascension from $\approx 0^{\circ}$ to $\approx 105^{\circ}$ and declination from $\approx +30^{\circ}$ to $\approx +60^{\circ}$). We can also notice that the speed of the meteors seems to increase as the right ascension decreases and the declination increases.

Figure 82 shows the SPS breakpoint+ plot, whose inflection point occurs early, near $D = 0.35$, i.e., the radiant's orbits are weakly concentrated in relation to the radiant's mean orbit.

Figure 83 presents the Valdeitor plot. In the plot we can identify the formation of a maximum activity peak in the radiant near the beginning of September. The peak of September seems to be related to another much larger radiant (possibly SPE). After this peak, another

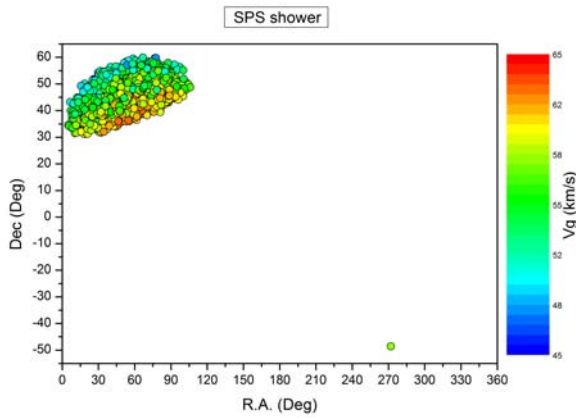


Figure 81 – Radiant of the Sigma Perseids (SPS).

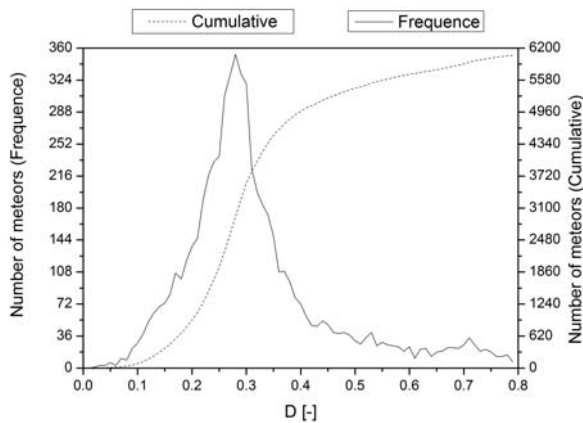


Figure 82 – SPS Breakpoint+ plot with a 20 degree radius.

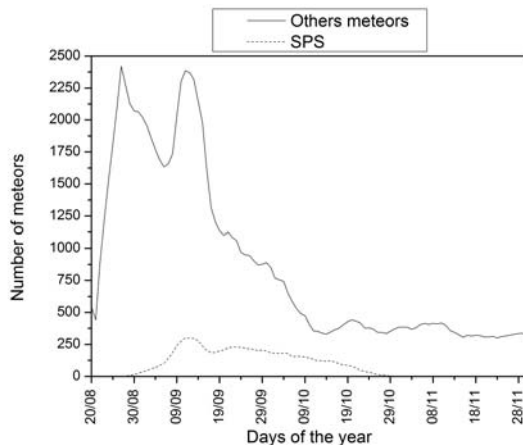


Figure 83 – SPS Valdeitor, 20° radius ($D \leq 0.22$).

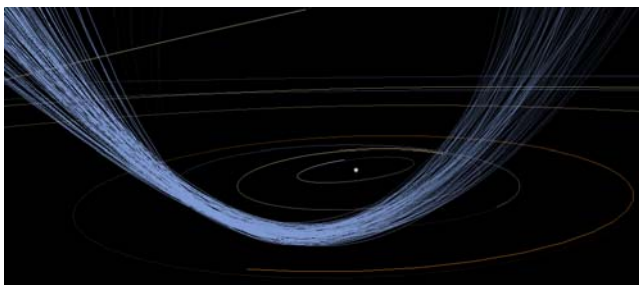


Figure 84 – Stream representation of the SPS ($D \leq 0.1$).

small peak occurs and then the radiant activity tends to decrease smoothly (while the activity of the other radiant decreases rapidly) extending until the end of October. SPS may be related to the SPE, and perhaps may be a stream that is drifting away.

Figure 84 is a stream representation of the SPS radiant meteors. This representation was created by exporting the orbital data of 110 meteors belonging to SPS (with $D \leq 0.1$).

3.22 TRD – October Taurids

Figure 85 shows the orbit distribution of the TRD radiant. We can notice the radiant coverage area (right ascension from $\approx 45^\circ$ to $\approx 120^\circ$ and declination from $\approx +0^\circ$ to $\approx 25^\circ$). We can also notice that the speed of the meteors seems to increase as the right ascension decreases and the declination increases.

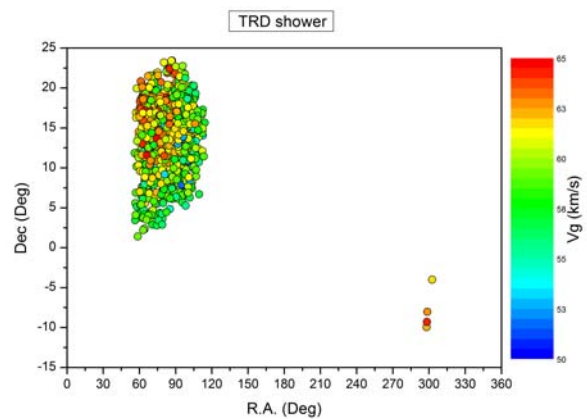


Figure 85 – Radiant of the October Taurids (TRD).

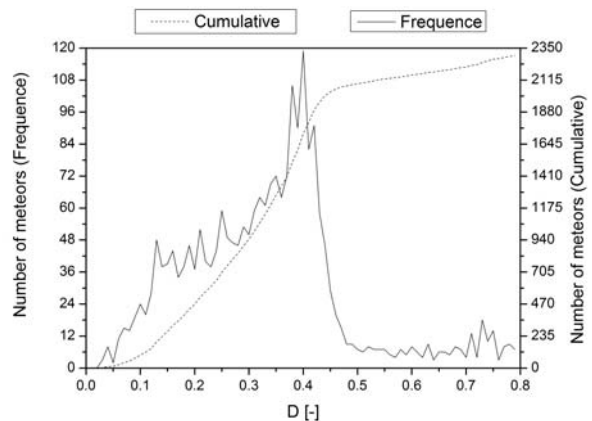
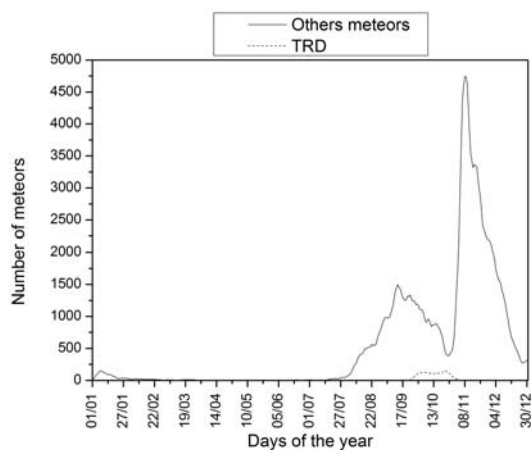
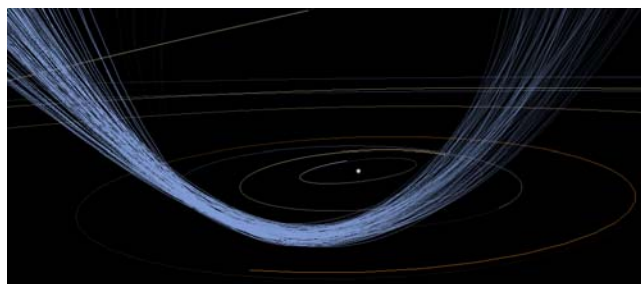


Figure 86 – TRD Breakpoint+ plot with a 20 degree radius.

Figure 86 shows the TRD breakpoint+ plot, whose inflection point occurs early, near $D = 0.4$, i.e., the radiant's orbits are weakly concentrated in relation to the radiant's mean orbit.

Figure 87 presents the Valdeitor plot. In the plot we can identify the activity of the radiant between September and November. We can also notice the activity of other radiants occurring together with the TRD radiant.

Figure 88 is a stream representation of the TRD radiant meteors. This representation was created by

Figure 87 – TRD Valdeitor, 20° radius ($D \leq 0.22$).Figure 88 – Stream representation of the TRD ($D \leq 0.1$).

exporting the orbital data of 107 meteors belonging to TRD (with $D \leq 0.1$). We found $D > 0.108$ when comparing the TRD orbit with meteors of other Taurid radiants in the IAU list which are also active during the September – November period. The value of D indicates the TRD is different from the two branches of the known Taurids (017 NTA, 002 STA) and the other showers in the respective period.

3.23 DRP – December rho Puppids

Figure 89 shows the orbit distribution of the DRP radiant. We can notice the radiant coverage area (right ascension from $\approx 90^\circ$ to $\approx 160^\circ$ and declination from $\approx -40^\circ$ to $\approx -10^\circ$). We can also notice that the speed of the meteors seems to increase as the right ascension decreases and the declination increases.

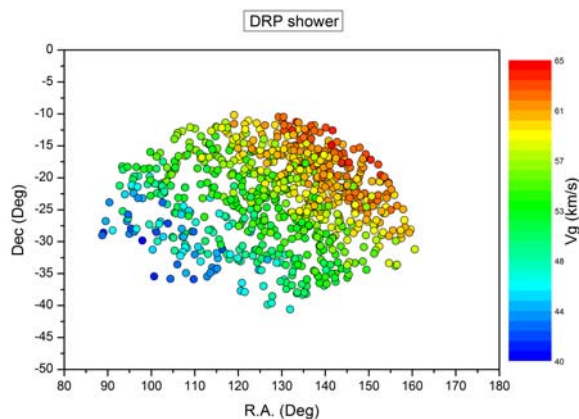


Figure 89 – Radiant of the December rho Puppids (DRP).

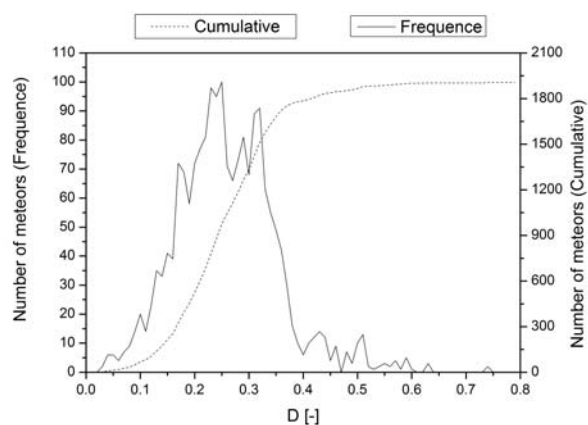


Figure 90 – DRP Breakpoint+ plot with a 20 degree radius.

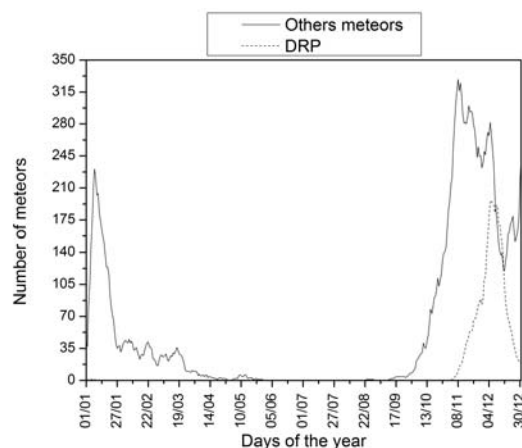
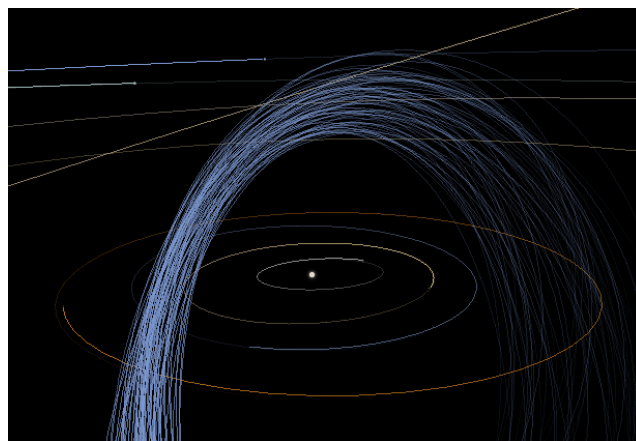
Figure 91 – DRP Valdeitor, 20° radius ($D \leq 0.22$).Figure 92 – Stream representation of the DRP ($D \leq 0.1$).

Figure 90 shows the DRP breakpoint+ plot. We can see that the inflection point occurs early, near $D = 0.3$, i.e., the radiant's orbits are weakly concentrated in relation to the radiant's mean orbit.

Figure 91 presents the Valdeitor plot. In the plot we can identify the formation of a maximum activity peak in the radiant near the beginning of December. We can also notice the activity of other radiants occurring together with the DRP radiant.

Figure 92 is a stream representation of the DRP radiant meteors. This representation was created by exporting the orbital data of 110 meteors belonging to DRP (with $D \leq 0.1$).

3.24 Conclusion

Based on the method of Amaral et al. (2018a), in a short time the Encontreitor software, proved to be an efficient computational application for finding new radiants. The current meteor databases have already been thoroughly searched for new radiants. However, many small radiants are still camouflaged by the occurrence of other larger radiants. Such radiants are difficult to discover (especially if depending on visual analysis).

The capability of the method proposed by Amaral et al. (2018a) to search for radiants based on orbital similarities allowed BRAMON to find radiants which were “invisible” until now by other methods.

The method was also able to identify a number of twin radiants, such as ADS, DGR, GSC, and UMS.

Some radiants (ADS, LSA, FLO, XCD, NAA, CVD, UMS, CVT, and OAG) have been found later by other authors using other methods. This confirms the robustness of the radiants found by Encontreitor.

We were also able to identify parent bodies with orbital similarity very close to the mean orbit of the meteors associated to the radiants of the NEC, PCS, and PCL.

References

- Amaral L., Di Pietro C., Trindade L., Zurita M., Silva G., Domingues M., Poltronieri R., Jacques C., and Jung C. (2018a). “A search method for meteor radiants”. *WGN, Journal of the International Meteor Organization*, **46:6**, 191–197.
- Amaral L., Trindade L., Di Pietro C., Zurita M., Poltronieri R., Silva G., Jacques C., Jung C., and Koukal J. (2018b). “Brazilian Meteor Observation Network: History of creation and first developments”. In *Proceedings of the International Meteor Conference, Petnica, Serbia, September 21–24 2017*. IMO, pages 171–175.
- Drummond J. D. (1981). “A test of comet and meteor shower associations”. *Icarus*, **45:3**, 545–553.
- EDMOND (2018). “EDMOND Database”. <https://fmph.uniba.sk/en/microsites/daa/division-of-astronomy-and-astrophysics/research/meteors/edmond/>.
- Galligan D. P. (2001). “Performance of the D-criteria in recovery of meteoroid stream orbits in a radar data set”. *MNRAS*, **327**, 623–628.
- Joepk T. J., Valsecchi G. B., and Froeschlé C. (2002). “Asteroid meteoroid streams”. In Bottke, Jr. W. F., Cellino A., Paolicchi P., and Binzel R. P., editors, *Asteroids III, first edition*, pages 645–652. University of Arizona Press, Tucson.
- Kornoš L., Koukal J., Piffel R., and Tóth J. (2014a). “EDMOND Meteor Database”. In Gyssens M., Roggemans P., and Zoladek P., editors, *Proceedings of the International Meteor Conference, Poznań, Poland, Aug. 22–25, 2013*. IMO, pages 23–25.
- Kornoš L., Matlovič P., Rudawska R., Tóth J., Hajduková, Jr. M., Koukal J., and Piffel R. (2014b). “Confirmation and characterization of IAU temporary meteor showers in EDMOND database”. In Joepk T. J., Rietmeijer F. J. M., Watanabe J., and Williams I. P., editors, *Proceedings of the Meteoroids 2013 Conference, A.M. University, Poznań, Poland, Aug. 26–30, 2013*. pages 225–233.
- SonotaCo (2009). “A meteor shower catalog based on video observations in 2007–2008”. *WGN, Journal of the IMO*, **37**, 55–62.
- SonotaCo (2018). “SonotaCo Network Simultaneously Observed Meteor Data Sets”. <http://sonotaco.jp/doc/SNM/>.
- Trindade L., Zurita M., Silva G., Daláva A., and Di Pietro C. (2019). “Identification of two new meteor showers: #797 EGR and #798 ACD”. *WGN, Journal of the IMO*, **47:6**, 184–187.
- Universe Sandbox (2020). “Universe Sandbox 2.2”. <http://universesandbox.com/>.

Handling Editor: Jürgen Rendtel

From Cosmic Rays and Meteors

*H. W. Wilschut*¹

A recent article (Prohira et al., 2020) in Physical Review Letters has drawn considerable attention. It proposes to measure high-energy cosmic neutrinos by means of radar. This goes back to the origin of meteor detection by radar, which started as an attempt to measure cosmic rays. In this article the history of cosmic ray and meteor research by radar and the proposal of the article are reviewed. Relevant high-energy particle physics will be explained.

Received 2020 June 4

1 Introduction

Before World War II cosmic rays were the only way to do what is now called particle physics. The nature of cosmic rays was in many respects still puzzling, but the concept of a particle shower was already developed. Such showers occur when high-energy cosmic rays interact with the upper atmosphere and produce a shower of energetic ionizing radiation. Also radar research had started at that time, but it was classified, i.e. a military secret. Radar would play a major role in WWII for example in the Battle of Britain.

When war started the physicist Bernard Lovell was taken from his university research at Manchester and put to work on radar. This was not at all related to what he was studying at the time. Under Patrick Blackett he worked on cosmic rays using triggered Wilson cloud chambers. This method was developed by Blackett, who would receive the Nobel Prize of 1948 for this work. When Lovell worked with radar he saw on occasion strange radar signals. He thought they might be related to cosmic ray events. He mentioned it to Blackett who was intrigued and, in the midst of their duties for the war effort, produced their classic paper (Blackett & Lovell, 1941). Only after the war Lovell found out that the anomalous signals were not related to cosmic rays but to meteoroids, as will be discussed below.

Now almost 80 years later the idea of cosmic-ray radar-detection is back, albeit in a slightly modified form. The cosmic rays that one wants to measure now, are high-energy neutrinos. They are so rare that they need to be looked for in a very large volume detector requiring a cost-effective method. The idea is to put a transmitter and many receivers in the ice of the Antarctic and detect radar reflections of the ionizing shower in the ice. In a first step the authors of (Prohira et al., 2020) have simulated a high energy neutrino using an electron beam and have observed the expected signal.

Because not all readers will be familiar with particle physics, I will first discuss some relevant aspects of cosmic rays and high-energy physics. This is followed by the history of the “non-discovery” of cosmic ray radar detection as told by Lovell. In the final section the new measurement is discussed.

2 Cosmic rays

In Figure 1 the energy spectrum of cosmic rays is shown. On the horizontal scale is the energy of the cosmic particle in GeV (Giga-electronvolt). Because their energies are much larger than their rest mass (one proton has a mass of 1 GeV) they travel with nearly the speed of light. For comparison the kinetic energy of the lighter meteoroids that could still be detected using radar is indicated by the red arrow. (Visible meteoroids have energies larger than 10^{13} GeV. We assume that this is converted into ionization to the same extent as a cosmic ray.) A cosmic ray is mostly a particle like a proton (a hydrogen atom stripped of its electron) but may also be heavier, for example an iron nucleus.

They come from outer space, where they can be produced in violent processes, being charged, they can also gain energy by acceleration. The mechanism for this is not known in detail.

When high-energy particles reach Earth, they may hit an atom in the atmosphere producing more particles. These are also very energetic causing subsequent

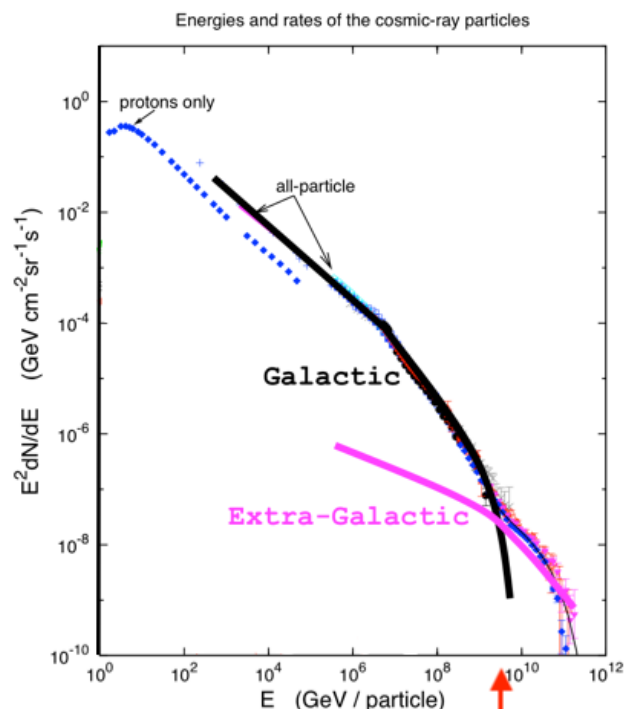


Figure 1 – Energy spectrum of cosmic rays (adapted from the IceCube collaboration). The red arrow indicates the kinetic energy of a 1 μg meteoroid with a characteristic velocity of 40 km/s (0.5×10^{10} eV or 0.8 J).

¹University of Groningen. Email: hwwilschut@gmail.com, Home address: Sankt Augustin, Germany

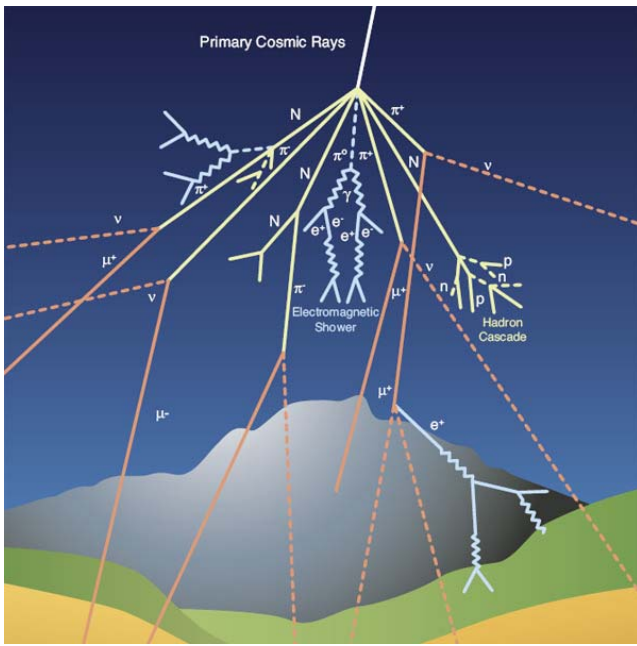


Figure 2 – Schematic depiction of a cosmic shower. This picture was taken from the website of the Auger collaboration. It emphasizes the different types of elementary particles that can be created in the primary and secondary interactions in the atmosphere.

reactions etc., this is called a particle shower. Most of these new particles will be unstable and decay into other more stable particles. Figure 2 shows such a shower, with emphasis on the many different processes and particles. The most copiously produced particle reaching the ground is the muon (μ). These muons have often enough energy to cross layers of concrete. They are a nuisance for most particle-physics experiments, forming an ever present background of about 100 muons/m²/s. However they can still be useful for calibrating the particle detectors. In Figure 1 the vertical axis gives the number of particles/s and per direction (sr⁻¹). This rate is multiplied by E^2 (GeV²) and the data binned per GeV. The multiplication with E^2 is necessary because the flux of cosmic particles decreases so fast with energy that the logarithmic scale is not sufficient to keep the plot manageable in its vertical size.

The first conclusion we can draw from this figure is that observing a cosmic ray by means of radar when it is in the range 10^6 GeV would be very difficult. Pierre Auger was the first to measure such a high energy using a few simple radiation detectors and found the extent of the shower to be about 100 m (Auger et al., 1939). The large size and the height in the atmosphere, where the shower originates, are all factors that can thwart the radar method. At the highest energy events become extremely rare. The Auger collaboration predicts that above 10^{11} GeV only one particle in a year will be seen in a km² area. Their detection system is located in the Pampas of Argentina where detectors are placed over a large area. For more information I recommend their website www.auger.org.

Physicist wonder if there is no limit to the high end of the spectrum. There seems to be a limit but

this is due to a strong restriction for the observation of ultrahigh-energy particles:

The universe is filled with photons that constitute the cosmic microwave background. A proton may hit such a photon that has an energy of only 10^{-14} GeV. But a proton of about 5×10^{10} GeV can still be excited by it to produce a pion particle. (In the laboratory we can easily do this reaction by shooting photons of only 0.3 GeV on a proton at rest, the produced pion has a rest mass of 0.14 GeV. The equivalence of these two system, i.e, photon on proton and proton on photon, is a nice example of a Lorentz transformation.) At 5×10^{10} GeV the spectrum indeed drops off much more rapidly as can be seen in Figure 1. Another limitation of charged particles is that they are deflected due to interstellar magnetic fields of unknown magnitude. In general, we can not know where they are coming from. These are some of the reasons why one would want to use alternative messengers from the deep universe.

Neutrinos may provide such an alternative. Neutrinos are elusive near mass-less particles that interact via the weak force. (The weak force rules radioactive decay and keeps the Sun from burning too rapidly.) Neutrinos have no charge and because of the weakness of the force do almost not react with whatever they find on their way. But that advantage has also a large drawback: Neutrinos can easily travel through Earth without interacting, let alone that they would interact in a detector. Nonetheless a tiny fraction does, requiring a very large volume at high density to make detection practical. Current detector systems are located underwater viewing a volume of water or in the case of the IceCube detector the ice of the Antarctic. They measure the light produced in the wake of charged shower particles that move with speeds larger than the velocity by which light propagates in matter (Cherenkov radiation). The light is detected with costly photomultipliers.

Note that the elusive nature of neutrinos allows looking for them coming from below, going through Earth. This rejects nicely the background muons mentioned above. For more information I refer to the websites of IceCube and KM3NeT.

Neutrinos with an energy up to 10^6 GeV have been observed until now. To observe higher energy neutrinos will need a larger volume of mass, but can that be done cost-effectively? This is were the historic method of radar detection may become useful.

3 History^a

When Bernard Lovell returned to the university after the war, he was about to dust of the Wilson chambers to continue his research. But his boss Blackett reminded him that he had seen these interesting phenomena using radar, would it not be more opportune to do research on that? He was now an expert on radar. In particular, he developed the short wavelength radar for use in airplanes. In particular, he used a wavelength of 9 cm generated with a magnetron operating at 3 GHz,

^aBased on an interview with Lovell, available on YouTube <https://youtu.be/R-SLE6n940c>

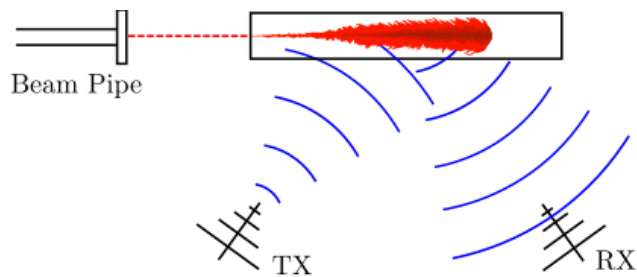


Figure 3 – Schematic setup for testing the concept to observe radar echoes from a high-energy neutrino event. A beam pulse from an electron accelerator enters a 4 m long block of polyethylene from the left, mimicking an electromagnetic shower the neutrino would make. The transmitter operates in the range of 1–2.1 GHz. (Adapted from (Prohira et al., 2020).)

a top secret. When Roosevelt and Churchill decided to collaborate on scientific war research the magnetron was part of the deal that also involved the atomic bomb.

Pierre Auger, had already seen showers with a 100 m baseline in 1938. Therefore, Lovell needed a wavelength longer than 9 cm. A colleague physicist, Stanley Hey had used a 4 m wavelength radar for air defense. Hey helped Lovell to obtain this army surplus. On a cold lonely field in December Lovell saw fantastic signals but soon realized that he observed way too many. It was again Hey who helped him out. He had been involved in tracking the V2 rockets at the end of the war. There he learned that the signals Lovell saw were understood as due to meteors, knowledge that was classified. Of course, December is the month of the Geminids, which explains why he saw so many signals.

Lovell became a successful astronomer, building what was later named the Lovell radio telescope on the grounds of Jodrell Bank, once the cold lonely field where Lovell had put up his radar. The radiotelescope is a 75 m dish that also did its military service during the Cold war. It watched for Russian rockets and satellites. When, in this period, Lovell went to the USSR to setup a scientific collaboration, the Russians tried to get him to defect and brainwash him. Clearly, Lovell would figure well in the recent book by Neil de Grasse Tyson and his assistant Avis Lang with the ominous title “Accessory to War – The unspoken alliance between Astrophysics and the Military”.

4 Radar echoes from high-energy particles

An electromagnetic shower (mostly electrons and positrons) following a typical interaction of a high-energy neutrino in ice will be about 10 m long and about 0.5 m in diameter. The lifetime of free electrons created in the shower is of the order of 1 ns. It is thus best probed with a GHz radar pulse. The frequency Lovell has pioneered.

The authors of (Prohira et al., 2020) mimic the shower by shooting a pulse of 10^9 electrons of 10 GeV into a block of solid polyethylene (Figure 4), approaching the effect of a 10^9 GeV neutrino interaction in ice. The transmitter operated at 50 W and 2.1 GHz. They observed a signal of a few ns duration well above background. The reader familiar with radio detection of meteors may further note that forward scattering is employed and that the reflections are in the overdense regime. As the speed with which the shower develops will be the light speed (3 ns/m) a Doppler shift can be observed, just like in a meteor shower.

The positive result obtained for a radar echo of a particle shower is just a first step for a full-size detector for ultra-high energies. Of course, the detection medium will have to consist of high density material instead and not the atmosphere as Lovell had envisioned. But nonetheless, if it ever comes to development of a high-energy particle detector with radar, they should call it the Lovell detector.

References

- Auger P., Ehrenfest P., Maze R., Daudin J., and Fréon R. A. (1939). “Extensive Cosmic-Ray Showers”. *Reviews of Modern Physics*, **11:3-4**, 288–291.
- Blackett P. M. S. and Lovell A. C. B. (1941). “Radio Echoes and Cosmic Ray Showers”. *Proceedings of the Royal Society of London Series A*, **177:969**, 183–186.
- Prohira S., de Vries K. D., Allison P., Beatty J., Besson D., Connolly A., van Eijndhoven N., Hast C., Kuo C. Y., Latif U. A., Meures T., Nam J., Nozdrina A., Ralston J. P., Riesen Z., Sbrocco C., Torres J., and Wissel S. (2020). “Observation of Radar Echoes from High-Energy Particle Cascades”. *Physical Review Letters*, **124:9**, 091101.

Handling Editor: Jean-Louis Rault

This paper has been typeset from a \LaTeX file prepared by the authors.

Preliminary results

Results of the IMO Video Meteor Network — December 2018, and summary of 2018

Sirko Molau¹, Stefano Crivello, Rui Goncalves, Carlos Saraiva, Enrico Stomeo, Jörg Strunk, and Javor Kac

The IMO Video Meteor Network cameras recorded over 55 000 meteors in almost 10 000 hours of observing time during 2018 December. Flux density and population index profiles are presented for the Geminids, as well as flux density profile for the Ursids. The annual summary of the 2018 IMO Video Meteor Network observations is presented. More than 444 000 meteors were recorded in over 113 000 hours of observing time.

Received 2020 June 12

1 Introduction

During the last month of 2018, 81 video cameras were in operation, which recorded over 55 000 meteors in almost 10 000 hours of effective observing time (Table 4 and Figure 1). The weather was mediocre and the observing statistics look like a Swiss cheese. However, if we compare December with previous years, it is not that bad after all. We had never recorded more than 65 000 meteors in any December, and the average of 5.6 meteors per hour is at the upper end of the usual range. Every second camera managed to observe during twenty or more observing nights – we have experienced months with a much poorer result.

2 Geminids

Highlight of the month – as in every year – were the Geminids, whose maximum was predicted for mid-day (UT) of 2018 December 14. Hence, both the night before and after the peak promised high rates. As shown in Figure 2, activity was highest during the night of

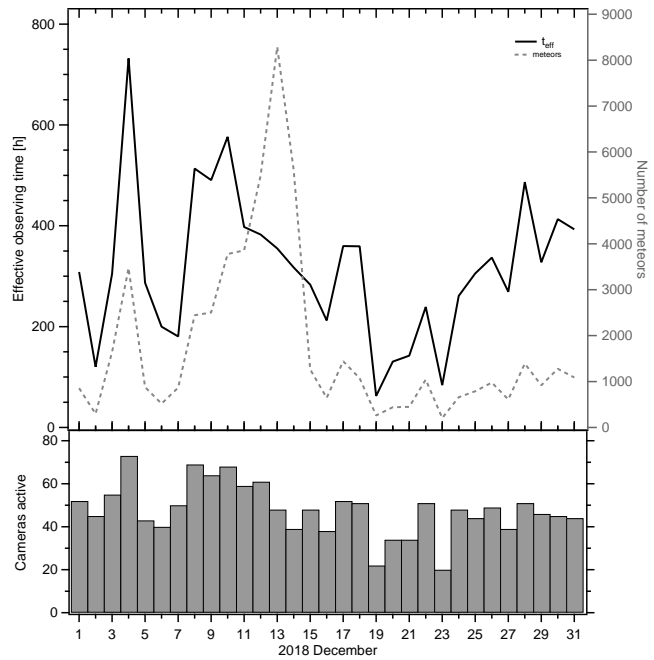


Figure 1 – Monthly summary for the effective observing time (solid black line), number of meteors (dashed gray line) and number of cameras active (bars) in 2018 December.

¹Abenstalstr. 13b, 84072 Seysdorf, Germany.
Email: sirko@molau.de

IMO bibcode WGN-483-molau-viddec
NASA-ADS bibcode 2020JIMO...48...92M

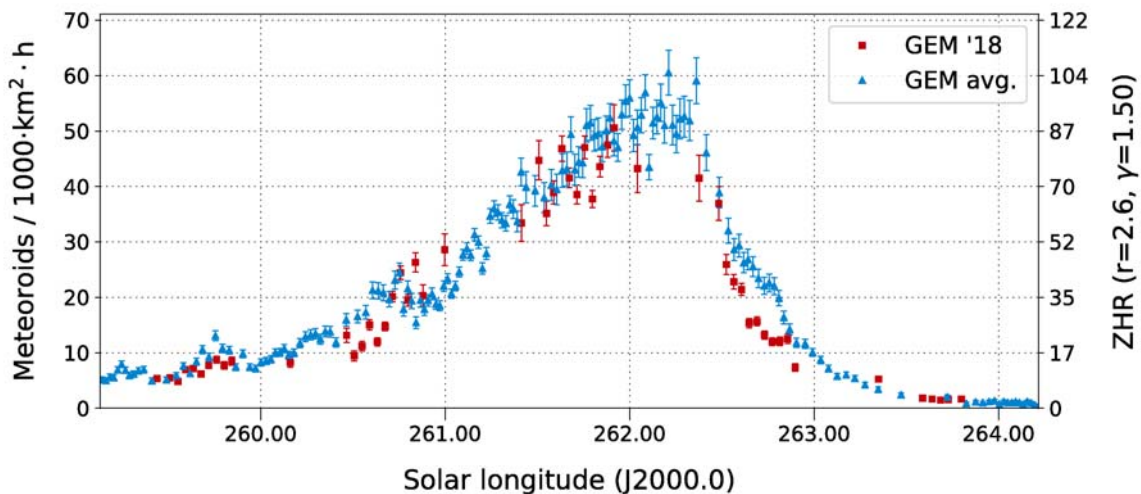


Figure 2 – Flux density profile of the Geminids 2018 (darker/red), compared with the long-term profile of the years 2012–2017 (without 2015, lighter/blue), derived from video data of the IMO Network.

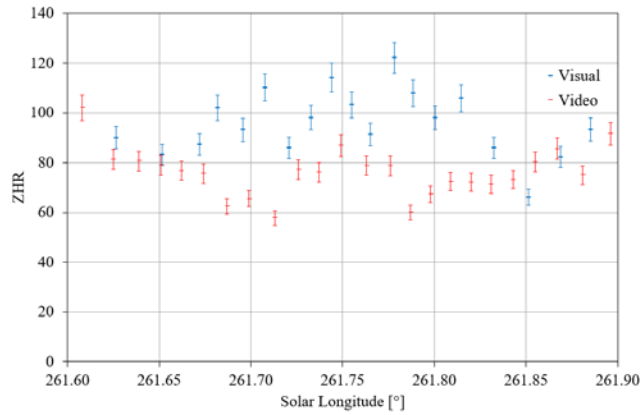


Figure 3 – Comparison of the activity profile of the Geminids on 2018 December 13/14, from visual (lighter/blue) and video observation (darker/red) of IMO.

December 13/14. There were strong fluctuations, but overall, the flux density profile fits well to the long-term average since 2012. During the following night, rates were still at the same high level in the first interval, but declined rapidly thereafter. Despite being as distant from the peak as the previous night, the flux density became much smaller, because the ascent of the activity to the maximum is shallower than the descent thereafter.

We have checked if the fluctuations in the activity profile of the pre-maximum night can be found in visual IMO data (International Meteor Organization, 2018) as well (Figure 3). It turns out that visual observations show even stronger scatter, but there is little overlap with the video data. Neither “minimum”, at $261^{\circ}72$ and $261^{\circ}78$ solar longitude, was not confirmed by visual observations.

The population index of the Geminids varies at the time of peak between 1.8 and 2.4, but the sporadic values are about the same. Only at the end of the activity period, near 263° solar longitude, is the r -value of the Geminids clearly smaller than the sporadic r -value (Figure 4).

To check whether this effect is because of the comparably small data set of a single year, we calculated the average population index profile of the years 2011 to 2017. We can see that the r -value of the 2018 Gemi-

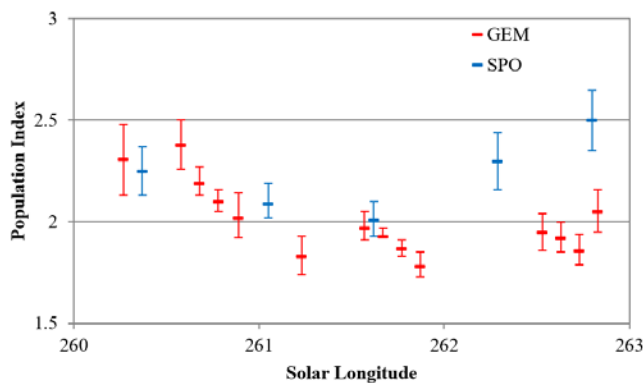


Figure 4 – Population index of the Geminids (darker/red) and sporadic meteors (lighter/blue) during the Geminid maximum 2018.

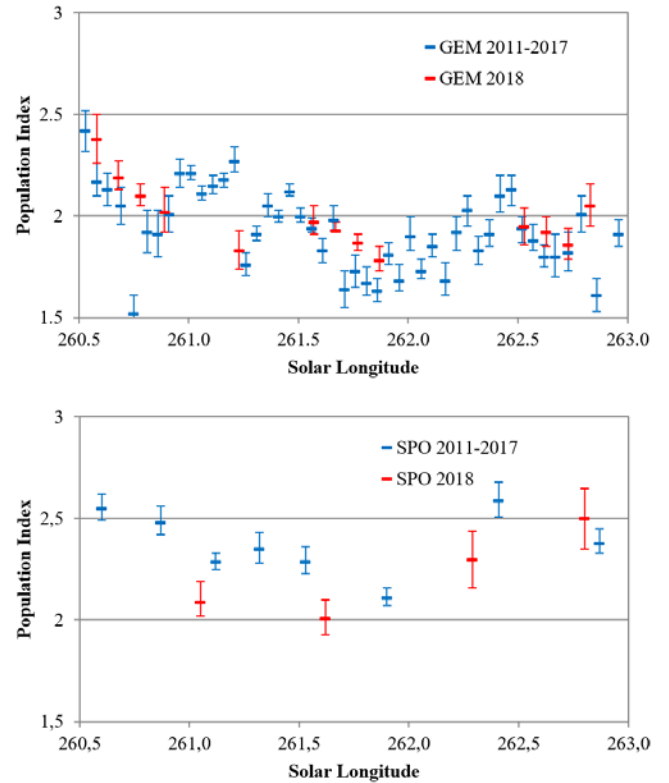


Figure 5 – Comparison of the population index profile of the Geminids (top) and sporadic meteors (bottom). We show the values of the years 2011–2017 (lighter/blue) and 2018 (darker/red).

nids fits nicely to the long-term profile (Figure 5, top), whereas the sporadic population index is slightly smaller (Figure 5, bottom). Interestingly, we also see in the long-term sporadic profile a dip at the time of the Geminid peak, which hints on a pollution by shower meteors.

Finally, we present in Figure 6 the population index profile of the Geminids and sporadic meteors over all years from 2011 to 2018. In the interval between $261^{\circ}8$ and $262^{\circ}2$ solar longitude, i.e. right at the Geminid maximum, the population index reaches a low of about $r = 1.8$. Thereafter it raises to values of 2.1, only to reach a secondary minimum with a similar low population index of about $r = 1.8$ at $262^{\circ}7$ solar longitude. It would be interesting to know if visual data show the same effect.

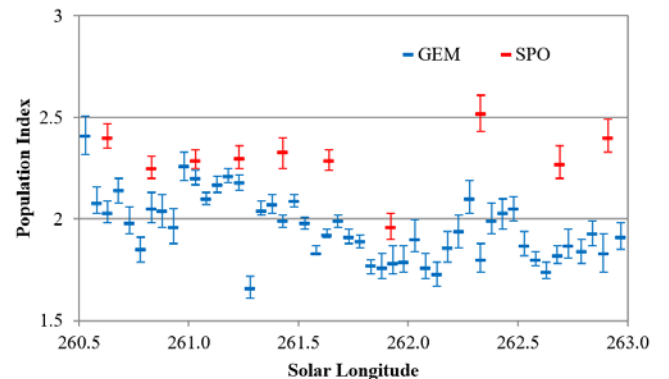


Figure 6 – Population index of the Geminids (darker/red) and sporadic meteors (lighter/blue) in the average of the years 2011 to 2018.

3 Ursids

The maximum of the last shower of 2018, the Ursids, is expected at $270^{\circ}0$ solar longitude according to the IMO Meteor Shower Calendar (Rendtel, 2017). In practice, we observed highest rates in 2011 at $270^{\circ}4$, and a rather short peak at $270^{\circ}8$ solar longitude in 2014. In all the other years since 2011, we could not observe an unambiguous peak.

In 2018, the time of maximum fell perfectly into the European night-time hours, and indeed we could record a strong peak with a flux density of up to 25 meteoroids per 1000 km² per hour on December 22/23 right after midnight (UT). Figure 7 shows the activity profile of the years 2016 and 2018, which complement each other perfectly: Whereas in 2016 we could record the intervals before and after the peak, but the peak itself was missing, the conditions were the opposite in 2018. Just as in 2014, the peak occurred at a solar longitude of $270^{\circ}8$. The full width at half maximum (FWHM) was only $0^{\circ}4$ in solar longitude or less than ten hours, which is comparable to the FWHM of the Quadrantids. This explains why we do not see a lot from the Ursids in years when the peak falls into the daytime hours.

4 2018 summary of the IMO Video Network

At the end of the December report, we want to review as usual the complete year. Whereas up to 2015 we reported a continuous growth in the number of IMO Network observations, the activity level has been stagnating since then at a constantly high level. In the 20th year of the IMO Network, 43 observers (2017: 41) from 11 countries (2017: 11) contributed with 88 meteor cameras overall (2017: 83). Front runner was once again Germany with 21 video cameras, followed by Italy (15). 13 cameras were operated in Portugal, and 12 in Hungary and Slovenia. Less than ten cameras were operated in Poland, Spain, the USA, in the Netherlands, Finland and Russia.

During 365 observing nights (2017: 365) and 113 760 observing hours (2017: 118 269) we recorded a total of

444 033 meteors (2017: 433 047). The average rate was 3.9 meteors per hour, which is identical to the average of the last four years.

Table 1 shows the monthly distributions of video observations. On average, we recorded 9 500 hours per month. With more than 13 000 hours, most observing time in 2018 was collected during the months August to October, making them the 5th, 1st and 4th rank, respectively, in the long-term IMO Network statistics. We have had an unbroken run of recording more than 10 000 meteors each month since June 2010, but this series almost came to an end in March 2018.

Seven observers from Germany, Portugal and Italy managed to accumulate more than 300 observing nights in 2018, two less than in the previous year. The three front runners did not change compared to last year, only their order did. In this year, Sirko Molau was on top with 345 nights, followed by Rui Goncalves (334) and Rui Marques (327). In addition, with regards to the effective observing time, the first three places did not change compared to 2017, whereby Rui Goncalves and Sirko Molau managed to collect over 10 000 hours of effective observing time alone. Looking at the plain meteor counts, Sirko Molau was dominating with almost 63 000 detections, which is the second-best annual outcome in the IMO Network history. Unbeaten in this respect remains Detlef Koschny, who recorded 75 000 meteors back in 2016. Second to fourth ranks are taken by Stefano Crivello, Enrico Stomeo and Rui Goncalves with over 30 000 meteors each. There are nine more observers who managed to contribute more than 10 000 records to the meteor database.

Table 3 presents the details for all active IMO Network observers in 2018. The number of cameras and stations refers to the major part of the year.

Whereas there had been 15 individual cameras that recorded meteors during over 300 nights in 2017, there was just a single camera in 2018. That one would not even have made it into the Top-10 of the previous year! Thanks to the weather conditions, most observing nights were collected by cameras in Italy and Portugal.

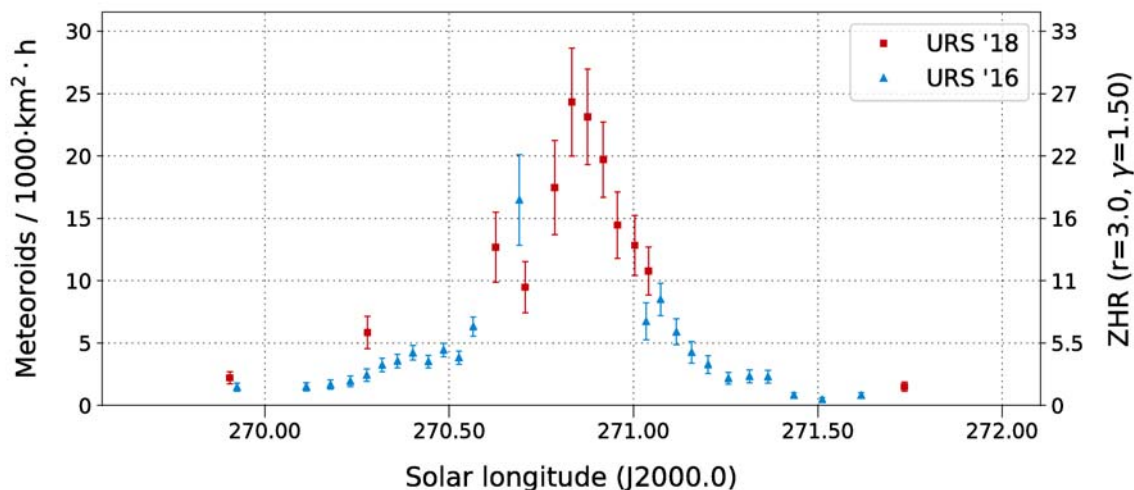


Figure 7 – Flux density profile of the 2018 Ursids (darker/red) and 2016 (lighter/blue), obtained from observations of the IMO Video Meteor Network.

Table 1 – Monthly distribution of video observations in the IMO Network 2018.

Month	Observing Nights	Eff. Observing Time	Meteors	Meteors / Hour
January	31	8 172.2	20 672	2.5
February	28	8 310.9	16 565	2.0
March	31	6 172.2	10 438	1.7
April	30	9 013.7	18 789	2.1
May	31	7 545.6	14 965	2.0
June	30	5 795.3	14 236	2.5
July	31	8 348.7	34 264	4.1
August	31	13 140.5	88 080	6.7
September	30	14 421.8	54 899	3.8
October	31	13 725.6	74 787	5.4
November	30	9 282.5	41 307	4.4
December	31	9 831.4	55 031	5.6
Overall	365	113 760.4	444 033	3.9

The following cameras, despite having recorded more than 10 000 meteors each, are absent from the Top-10: BMH2 (13 067), AVIS2 (12 268), SCO38 (10 764), STG38 (10 448) and ICC9 (10 361).

The complete dataset from 1993 through 2018 is available for download at the IMO Network homepage <http://www.imonet.org>. Our database meanwhile comprises 3 971 618 meteors from 981 838 hours of effective observing time during 6 834 nights. By the 20th anniversary of the IMO Video Meteor Network in March 2019 we may have collected one million hours of observing time and four million meteors. If we really managed to do so, we will let you know in the next report.

We would like to thank as always the avid observers who contribute to the camera network. We are particularly grateful to Stefano Crivello, Enrico Stomeo, Rui Goncalves, Carlos Saraiva and Jörg Strunk, who double-check the observations for every month together with Sirko Molau, thus ensuring the high quality level of the database.

Last but not least we have to state, that the level of workload caused another significant delay in the completion of this report. We assume that this will be the last monthly report in this format. Starting from the next, we will probably switch to quarterly reports.

References

- International Meteor Organization (2018). “Geminids 2018 campaign Live Graph”. http://www.imo.net/members/imo_live_shower/summary?shower=GEM&year=2018.
- Rendtel J. (2017). “2018 Meteor Shower Calendar”. International Meteor Organization. IMO INFO(2-17).

Handling Editor: Javor Kac

Table 2 – The ten most successful video systems in 2018.

Camera	Location	Observer	Observing Nights	Eff. Observing Time [h]	Meteors	Meteors / h
MARIO	Faenza (IT)	Mario Bombardini	305	1 874.5	9 169	4.9
TEMPLAR1	Tomar (PT)	Rui Goncalves	299	2 167.1	8 107	3.7
TEMPLAR2	Tomar (PT)	Rui Goncalves	294	2 158.1	6 578	3.0
JENNI	Faenza (IT)	Francesca Cineglosso	292	1 472.9	7 581	5.1
TEMPLAR5	Tomar (PT)	Rui Goncalves	291	1 851.6	5 653	3.1
TEMPLAR4	Tomar (PT)	Rui Goncalves	289	2 054.2	6 619	3.2
SALSA3	Tucson (US)	Carl Hergenrother	288	2 415.7	5 642	2.3
LUDWIG2	Ludwigsfelde (DE)	Rainer Arlt	288	1 486.1	8 084	5.4
MIN38	Scorze (IT)	Enrico Stomeo	287	1 534.2	11 153	7.3
REMO4	Ketzür (DE)	Sirko Molau	285	1 708.0	11 633	6.8

Table 3 – Distribution of video observations over the observers in 2018.

Observer	Country	Observing Nights	Eff. Observing Time [h]	Meteors	Meteors / h	Cameras (Stations)
Sirko Molau	Germany	345	10 616.2	62 822	5.9	7 (2)
Rui Goncalves	Portugal	334	10 930.5	30 362	2.8	6 (1)
Rui Marques	Portugal	327	3 429.6	10 790	3.1	2 (2)
Carlos Saraiva	Portugal	320	8 526.8	16 938	2.0	5 (1)
Enrico Stomeo	Italy	307	4 398.9	30 805	7.0	4 (1)
Stefano Crivello	Italy	306	6 522.4	33 935	5.2	4 (1)
Mario Bombardini	Italy	305	1 874.5	9 169	4.9	1 (1)
Jörg Strunk	Germany	298	7 433.8	26 046	3.5	5 (1)
Bernd Klemt	Germany	292	2 798.0	10 144	3.6	2 (2)
Francesca Cineglosso	Italy	292	1 472.9	7 581	5.1	1 (1)
Rainer Arlt	Germany	288	1 486.1	8 084	5.4	1 (1)
Carl Hergenrother	USA	288	2 415.7	5 642	2.3	1 (1)
Henrietta Nagy	Hungary	285	2 668.2	11 293	4.2	3 (3)
Hans Schremmer	Germany	284	1 521.3	4 646	3.1	1 (1)
Mitja Govedič	Slovenia	273	3 352.9	7 727	2.3	3 (1)
Maurizio Carli	Italy	272	1 849.2	13 067	7.1	1 (1)
István Tepliczky	Hungary	267	2 729.9	8 420	3.1	2 (1)
Maciej Maciejewski	Poland	263	4 800.3	18 589	3.9	4 (1)
Wolfgang Hinz	Germany	263	1 543.2	5 789	3.8	1 (1)
Fabio Moschini	Italy	255	1 518.9	4 056	2.7	1 (1)
Flavio Castellani	Italy	252	1 856.1	5 907	3.2	1 (1)
Thomas Bianchi	Italy	248	1 030.3	4 183	4.1	1 (1)
József Morvai	Hungary	244	1 434.3	2 437	1.7	1 (1)
Leo Scarpa	Italy	244	1 301.3	2 400	1.8	1 (1)
Károly Jónás	Hungary	242	2 565.0	5 022	2.0	1 (1)
Jure Zakrajšek	Slovenia	241	2 100.1	7 408	3.5	2 (1)
Wala Węgrzyk	Poland	238	1 153.3	3 195	2.8	1 (1)
Javor Kac	Slovenia	233	4 155.5	19 207	4.6	4 (3)
Maurizio Eltri	Italy	224	1 317.6	5 908	4.5	1 (1)
Eckehard Rothenberg	Germany	221	1 320.6	2 672	2.0	1 (1)
Martin Breukers	Netherlands	215	1 228.4	2 849	2.3	1 (1)
Zsolt Perkó	Hungary	214	1 258.5	3 718	3.0	1 (1)
Mike Otte	USA	211	1 068.8	2 162	2.0	1 (1)
Stane Slavec	Slovenia	209	2 001.4	4 079	2.0	2 (1)
Kevin Förster	Germany	199	1 166.4	5 437	4.7	1 (1)
Antal Igaz	Hungary	188	1 075.5	1 460	1.4	1 (1)
Detlef Koschny	Netherlands	178	2 210.4	22 237	10.1	2 (2)
Ilkka Yrjölä	Finland	155	854.0	2 502	2.9	1 (1)
Paolo Ochner	Italy	144	747.4	1 566	2.1	1 (1)
Erno Berkó	Hungary	105	819.2	5 229	6.4	1 (1)
Tomasz Łojek	Poland	83	555.0	2 408	4.3	1 (1)
Stefano Missiaggia	Italy	66	490.8	4 218	8.6	1 (1)
Mikhail Maslov	Russia	28	154.5	1 197	7.7	1 (1)
other	Germany	2	6.7	727	108.5	1 (1)

Table 4 – Observers contributing to 2018 December data of the IMO Video Meteor Network. Eff.CA designates the effective collection area; the overall number of nights is the number of nights with at least one camera operating, the overall observing time and number of meteors are sums over all cameras.

Code	Name	Location	Camera	FOV [°]	Stellar LM [mag]	Eff.CA [km ²]	Nights	Time [h]	Meteors
ARLRA	Arlt	Ludwigsfelde/DE	LUDWIG2 (0.8/8)	1483	6.2	3812	16	64.3	365
BERER	Berkó	Ludányhalászi/HU	HULUD1 (0.8/3.8)	5524	4.8	3829	12	105.5	603
BIATO	Bianchi	Mt. San Lorenzo/IT	OMSL1 (1.2/4)	6422	4.0	1699	20	35.7	262
BOMMA	Bombardini	Faenza/IT	MARIO (1.2/4.0)	5779	3.3	644	22	181.8	1327
BREMA	Breukers	Hengelo/NL	MBB3 (0.75/6)	2399	4.2	641	9	46.9	182
BRIBE	Klemt	Herne/DE	HERMINE (0.8/6)	2369	4.2	674	17	89.7	407
CARMA	Carli	Bergisch Gladbach/DE	KLEMOI (0.8/6)	2374	4.6	1123	17	61.6	312
CASFL	Castellani	Monte Baldo/IT	BMH2 (1.5/4.5)*	4243	3.0	371	27	334.1	3271
CINFR	Cinegrosso	Monte Baldo/IT	BMH1 (0.8/6)	2402	5.0	1633	27	321.4	1429
CRIST	Crivello	Faenza/IT	JENNI (1.2/4)	5995	3.9	1240	19	158.1	1065
		Valbrenna/IT	ARCI (0.8/3.8)	5566	4.6	2571	18	139.1	1375
			BILBO (0.8/3.8)	5441	4.2	1764	18	138.3	1630
			C3P8 (0.8/3.8)	5489	4.2	1603	18	157.8	1140
			STG38 (0.8/3.8)	5574	4.4	1905	20	131.3	1870
ELTMA	Eltri	Venezia/IT	MET38 (0.8/3.8)	5607	4.3	2381	13	114.5	1089
FORKE	Förster	Carlsfeld/DE	AKM3 (0.75/6)	2387	5.1	2145	4	19.3	61
GONRU	Goncalves	Foz do Arelho/PT	FARELHO1 (0.75/4.5)	2260	3.0	206	3	2.4	11
		Tomar/PT	TEMPLAR1 (0.8/6)	2212	5.3	1873	25	211.0	851
			TEMPLAR2 (0.8/6)	2341	5.0	1718	26	214.8	790
			TEMPLAR3 (0.8/8)	1438	4.3	542	20	165.0	342
			TEMPLAR4 (0.8/3.8)	5180	3.0	497	25	199.5	837
			TEMPLAR5 (0.75/6)	2309	5.0	2248	25	180.0	772
GOVMI	Govedič	Središče ob Dravi/SI	ORION2 (0.8/8)	1471	5.5	2170	26	163.2	462
			ORION3 (0.95/5)	3152	4.9	2130	22	149.6	214
			ORION4 (0.95/5)	3818	4.3	1634	24	109.9	186
HERCA	Hergenrother	Tucson/US	SALSA3 (0.8/3.8)	2336	4.1	538	29	221.1	887
HINWO	Hinz	Schwarzenberg/DE	HINWO1 (0.75/6)	2375	5.1	1889	11	42.6	188
IGAAN	Igaz	Hódmezővásárhely/HU	HUHOD (0.8/3.8)	5502	3.4	764	15	80.3	306
		Budapest/HU	HUPOL (1.2/4)	2414	3.6	409	1	1.5	10
JONKA	Jonas	Budapest/HU	HUSOR2 (0.95/3.5)	2468	3.9	716	19	128.4	270
KACJA	Kac	Kamnik/SI	CVETKA (0.8/3.8)*	5334	4.3	2028	21	110.5	479
			REZIKA (0.8/6)	2269	4.4	863	20	151.3	901
			STEFKA (0.8/3.8)	5458	3.6	911	18	122.7	390
KOSDE	Koschny	Ljubljana/SI	SRAKA (0.8/6)	2348	4.8	1595	16	117.8	446
		La Palma/ES	ICC9 (0.85/25)*	660	6.7	2835	29	242.4	1378
			LIC2 (3.2/50)*	1933	6.5	6554	25	166.9	3115
MACMA	Maciejewski	Chełm/PL	PAV35 (0.8/3.8)	5329	4.0	1530	6	13.5	34
			PAV36 (0.8/3.8)*	5484	4.0	1501	7	18.0	49
			PAV43 (0.75/4.5)*	2251	4.7	1484	5	13.7	59
			PAV60 (0.75/4.5)	2302	5.1	1803	7	21.4	75

Table 4 – Observers contributing to 2018 December data of the IMO Video Meteor Network – continued from previous page.

Code	Name	Location	Camera	FOV [°]	Stellar LM [mag]	Eff. CA [km ²]	Nights	Time [h]	Meteors
MARRU	Marques	Lisbon/PT	CAB1 (0.75/6) RAN1 (1.4/4.5) TOALDO (1.2/4.5)	2362 4395 4329	4.8 4.0 4.6	1517 1330 2049	28 25 20	261.7 218.7 192.5	840 938 2239
MISST	Missiaggia	Nove/IT	AVIS2 (1.4/50)*	1204	6.9	5982	24	82.4	420
MOLSI	Molau	Seysdorf/DE	DIMCAM1 (0.8/8) ESCIMO2 (0.85/25) REMO1 (0.8/8) REMO2 (0.8/8) REMO3 (0.8/8) REMO4 (0.8/8)	1553 154 1467 1479 1422 1478	6.8 8.1 6.5 6.4 6.4 6.5	10447 3828 5459 5037 4207 5355	23 20 21 19 20 18	49.6 76.0 77.1 86.2 98.7 94.9	412 117 398 582 424 567
MORJO	Morvai	Fülöpszállás/HU	HUFUL (1.4/5)	3666	3.8	805	20	137.5	320
MOSFA	Moschini	Rovereto/IT	ROVER (1.4/4.5)	3868	4.2	1240	26	230.1	1317
NAGHE	Nagy	Budapest/HU	HUKON (0.8/3.8) HUPIS (0.8/3.8) HUZAM (0.8/6) ORIE1 (1.4/5.7) HUBEC (0.8/3.8)* ARMEFA (0.8/6) Ro1 (0.75/6) Ro2 (0.75/6) Ro3 (0.8/12) Ro4 (1.0/8) SOFIA (0.8/12) LEO (1.2/4.5)* DORAEMON (0.8/3.8) KAYAK1 (1.8/28) KAYAK2 (0.8/12) MIN38 (0.8/3.8) NOA38 (0.8/3.8) SCO38 (0.8/3.8) MINCAM2 (0.8/6) MINCAM3 (0.8/6) MINCAM4 (0.8/6) MINCAM5 (0.8/6) MINCAM6 (0.8/6) HUAGO (0.75/4.5) HUMOB (0.8/6) PAV78 (0.8/6) FINEXCAM (0.8/6) PETKA (0.8/8) TACKA (0.8/12)	5475 5622 2359 2317 5557 2359 2354 2365 720 1568 726 4170 5522 1074 742 5587 5612 5583 2355 2302 2274 1481 2396 2428 2388 2376 2315 1431 715	4.0 4.0 4.7 3.8 2.9 4.5 4.0 4.1 5.7 4.2 4.8 4.5 4.7 5.7 5.7 4.5 4.2 4.8 5.6 4.5 4.7 6.0 5.3 4.6 4.6 4.4 5.5 5.6 5.3	1539 1340 373 470 907 536 635 1126 546 516 2044 3184 2642 1052 2362 1889 3304 3423 1150 1001 3200 2748 1247 1225 1264 2769 1956 784	18 20 6 23 9 29 23 23 19 27 15 20 133.1 23 22 21 14 15 13 14 15 20 10 12 6 23 20	86.3 131.0 7.5 159.7 46.8 154.0 162.9 149.1 152.5 200.3 117.8 90.9 15 156 186.7 199.7 195.6 60.1 64.8 45.1 62.0 58.5 97.1 64.1 47.4 10.3 186.7 176.5	670 257 24 695 61 529 556 513 265 463 339 105.9 2239 2268 2295 699 344 121 310 421 351 191 155 26 1362 408
OTTM	Otte	Pearl City/US		2317	3.8	373	6	7.5	24
PERZS	Perkó	Becsely/HU		5557	2.9	470	23	159.7	695
ROTEC	Rothenberg	Berlin/DE		2359	4.5	907	9	46.8	61
SARAN	Saraiva	Carnaxide/PT		2354	4.0	536	29	154.0	529
SCALE	Scarpa	Alberoni/IT		2365	4.1	635	23	162.9	556
SCHHA	Schremmer	Niederkrüchten/DE		720	5.7	1126	23	149.1	513
SLAST	Slavec	Ljubljana/SI		1568	4.2	546	19	152.5	265
STOEN	Stomeo	Scorze/IT		726	4.8	516	27	200.3	565
STRJO	Strunk	Herford/DE		4170	4.5	2044	15	117.8	463
TEPIS	Tepliczky	Agostyán/HU		5522	4.7	3184	20	90.9	339
WEGWA	Wegrzyk	Niezaszyn/PL		1074	5.7	2642	15	105.9	166
YRJIL	Yrjölä	Kuusankoski/FI		742	5.7	1052	133.1	156	166
ZAKJU	Zakrajšek	Petkovec/SI		5587	4.5	2362	23	186.7	2239
				5612	4.2	1889	22	199.7	2268
				5583	4.8	3304	21	195.6	2295
				2355	5.6	3423	14	60.1	699
				2302	4.5	1150	15	64.8	344
				2274	4.7	1001	13	45.1	121
				1481	6.0	3200	14	62.0	310
				2396	5.3	2748	15	58.5	421
				2428	4.6	1247	20	97.1	351
				2388	4.6	1225	10	64.1	191
				2376	4.4	1264	12	47.4	155
				2315	5.5	2769	6	10.3	26
				1431	5.6	1956	23	186.7	1362
				715	5.3	784	20	176.5	408
Overall								9831.4	55 031

* active field of view smaller than video frame

The International Meteor Organization

www.imo.net

Follow us on Facebook



InternationalMeteorOrganization

Follow us on Twitter



@IMOMeteors

Council

President: Cis Verbeeck,
Bogaertsheide 5, 2560 Kessel, Belgium.
e-mail: cis.verbeeck@scarlet.be

Vice-President: Juraj Tóth,
Fac. Math., Phys. & Inf., Comenius Univ.,
Mlynska dolina, 84248 Bratislava, Slovakia.
e-mail: toth@fmph.uniba.sk

Secretary-General: Robert Lunsford,
14884 Quail Valley Way, El Cajon,
CA 92021-2227, USA. tel. +1 619 755 7791
e-mail: lunro.imo.usa@cox.net

Treasurer: Marc Gyssens, Heerbaan 74,
B-2530 Boechout, Belgium.
e-mail: marc.gyssens@uhasselt.be
BIC: GEBABEBB
IBAN: BE30 0014 7327 5911
Bank transfer costs are always at your expense.

Other Council members:

Javor Kac (see details under WGN)

Detlef Koschny, Zeestraat 46,
NL-2211 XH Noordwijkerhout, Netherlands.
e-mail: detlef.koschny@esa.int

Sirko Molau, Abenstalstraße 13b, D-84072
Seysdorf, Germany. e-mail: sirko@molau.de

Francisco Ocaña Gonzalez, C/ Arquitectura, 7.
28005 Madrid, Spain.
e-mail: francisco.ocana.gonzalez@gmail.com

Vincent Perlerin, 16, rue Georges Bernanos,
51100 Reims, France.

e-mail: vperlerin@gmail.com

Jean-Louis Rault, Société Astronomique de
France, 16, rue de la Vallée, 91360 Epinay sur
Orge, France. e-mail: f6agr@orange.fr

Jürgen Rendtel, Eschenweg 16, D-14476
Marquardt, Germany. e-mail: jrendtel@aip.de

Commission Directors

Visual Commission: Rainer Arlt (rarlt@aip.de)

Generic e-mail address: visual@imo.net

Electronic visual report form:

<http://www.imo.net/visual/report/electronic>

Video Commission: Sirko Molau (video@imo.net)

Photographic Commission: Bill Ward

(William.Ward@glasgow.ac.uk)

Generic e-mail address: photo@imo.net

Radio Commission: Jean-Louis Rault

(radio@imo.net)

Fireballs: Online fireball reports:

<http://fireballs.imo.net>

Webmaster

Karl Antier, e-mail: webmaster@imo.net

WGN

Editor-in-chief: Javor Kac
Na Ajdov hrib 24, SI-2310 Slovenska Bistrica,
Slovenia. e-mail: wgn@imo.net;
include METEOR in the e-mail subject line

Editorial board: Ž. Andreić, M. Argo, D.J. Asher,
F. Bettonvil, J. Correira, M. Gyssens,
C. Hergenrother, T. Heywood, J.-L. Rault,
J. Rendtel, C. Verbeeck, S. de Vet, D. Vida.

IMO Sales

Available from the Treasurer or the Electronic Shop on the IMO Website € \$

IMO membership, including subscription to WGN Vol. 48 (2020)

Surface mail	26	32
Air Mail (outside Europe only)	49	60
Electronic subscription only	21	25

Proceedings of the International Meteor Conference on paper

1990, 1991, 1993, 1995, 1996, 1999, 2000, 2002, 2003, per year	9	12
2007, 2010, 2011, per year	15	20
2012, 2013, 2014, 2015 per year	25	34

Proceedings of the Meteor Orbit Determination Workshop 2006 15 20

Radio Meteor School Proceedings 2005 15 20

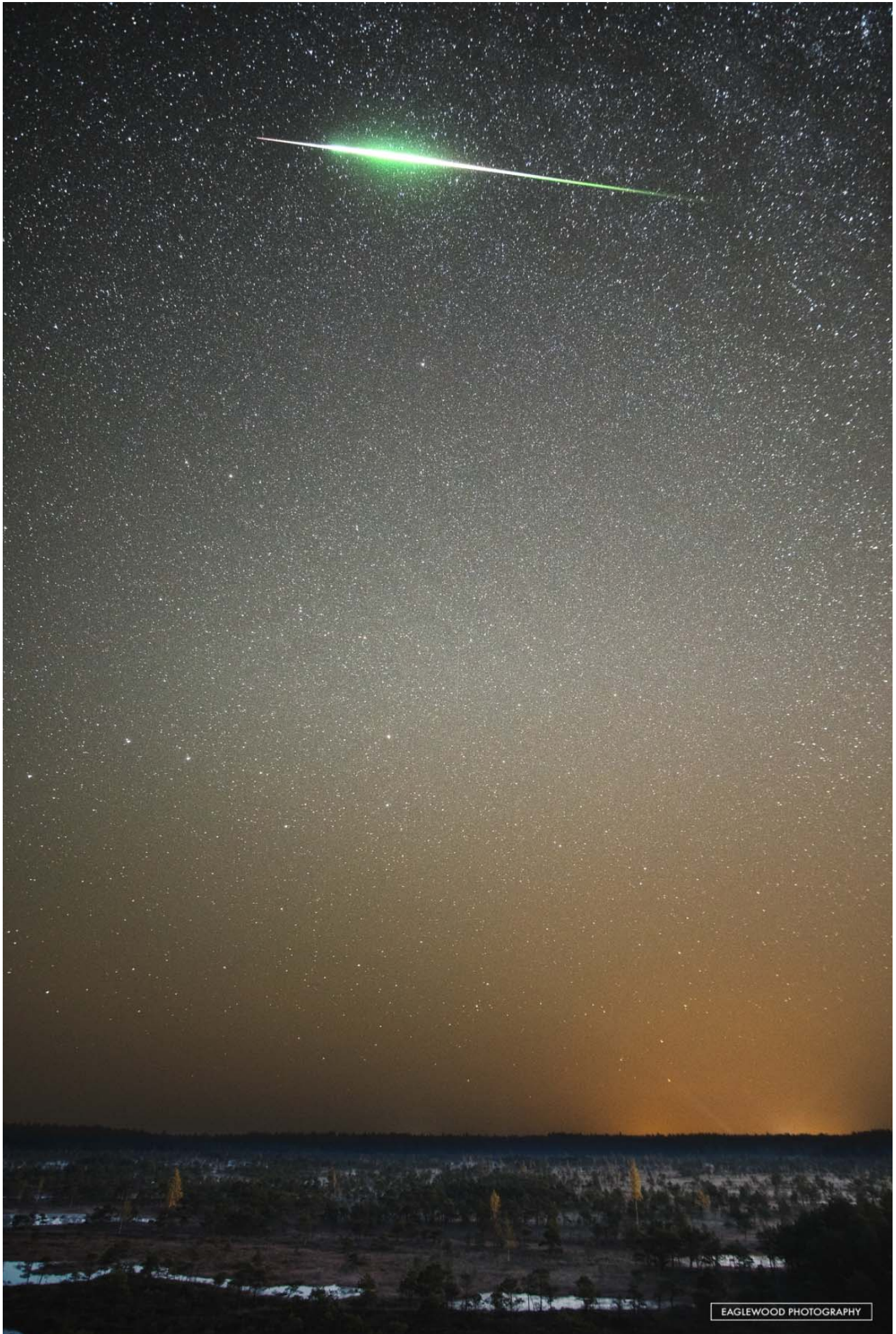
Handbook for Meteor Observers 15 20

Meteor Shower Workbook 12 16

Electronic media

Meteor Beliefs Project ZIP archive	6	8
------------------------------------	---	---

Latvian fireball of 2017 September 25



This incredible fireball was captured by Arvids Baranovs on 2017 September 25 at 21^h09^m UT from the raised bog of Kemeris in Latvia. Photo courtesy: Arvids Baranovs and Eaglewood Photography
eaglewoodfilms.com